

**Quantum Chemical Studies on the Catalytic Potential of Anionic Transition Metal
Compounds in Methane to Methanol and Carbon Dioxide Carboxylation Reactions**

by

Safaa Sader

A dissertation submitted to the Graduate Faculty of
Auburn University
in partial fulfillment of the
requirements for the Degree of
Doctor of Philosophy

Auburn, Alabama
May 6, 2023

Keywords: Computational chemistry, C-H activation,
CO₂ activation, electronic structures

Approved by

Evangelos Miliordos, Chair, J. E. Land Associate Professor of Chemistry and
Biochemistry

J. Vincent Ortiz, Ruth W. Molette Professor of Chemistry and Biochemistry
Konrad Patkowski, S. D. and Karen H. Worley Professor of Chemistry and Biochemistry
David Stanbury, Dr. J Milton Harris Emeritus Professor of Chemistry and Biochemistry

Abstract

Using transition-metal (TM) catalysts in organic chemistry conversion reactions is a well-established practice due to their superior efficiency. They have been particularly useful in both methane to methanol conversion (MTM) and carbon dioxide carboxylation reactions (CDC). But using the anionic forms of these transition metals is relatively recent and has sparked interest in using them as prospective catalysts, especially in light of experimental evidence supporting their stability and producibility. This dissertation describes the catalytic potential of the following transition-metal anions: platinum (Pt^-), palladium (Pd^-), and nickel (Ni^-) for both above-mentioned conversion reactions in addition to iron (Fe^-) in the MTM pathway. The dissertation will emphasize the energy profiles, geometries, turnover frequencies, and electronic structure of catalysts using DFT and post-Hartree-Fock electronic correlation methods. It will also elucidate the mechanism of reactions of the most promising routes through orbital analysis. The introduction briefly describes the computational methods used in this dissertation.

The second chapter covers the MTM pathway starting with an introduction to the research history performed. It describes our computational findings for the atomic and ligated TMs catalyzed MTM pathway with emphasis on differentiating between radical and [2+2] routes. The findings from bare TMs are followed by a discussion of the effect on the catalytic efficiency of these TMs using the energetic span model and chemical kinetics analysis.

Chapter 3 will outline the catalytic potential of atomic and ligated TMs in CO_2 carboxylation reactions with different unsaturated alkanes of various lengths which include ethene, butadiene, and both conjugated and unconjugated octadiene. Conclusions and discussions follow both chapters 2 and 3 with a description of the outlook for future work.

Acknowledgments

I am particularly grateful to my advisor, Dr. Evangelos Miliordos, for his teaching, support, and guidance and for being always available to us throughout the Ph.D. degree process. I also would like to thank my committee members for their useful insights and comments during the proposal and annual evaluation meetings. Thanks to Miliordos group members for their advice, technical assistance, and great scientific conversations. Finally, my deep thanks to Auburn University's department of chemistry and biochemistry, as well as Easley (formerly Hopper) clusters, and Alabama Supercomputer facilities for making these calculations possible and for their consistent support.

List of Publications and Copyrights

The following papers are incorporated in this dissertation, and they are attached at the end:

- 1) **Sader, S.** and Miliordos, E. (2021) "Methane to methanol conversion facilitated by anionic transition metal centers: The case of Fe, Ni, Pd, and Pt," *The Journal of Physical Chemistry A*, 125(11), pp. 2364–2373.
- 2) **Sader, S.** and Miliordos, E. (2022) "Being negative can be positive: Metal oxide anions promise more selective methane to methanol conversion," *Physical Chemistry Chemical Physics*, 24(36), pp. 21583–21587.
- 3) E. Claveau, **S. Sader.**, B. A. Jackson, S. N. Khan, E. Miliordos (2023) "Transition metal oxide complexes as molecular catalysts for selective methane to methanol transformation: Any prospects or time to retire?," *Physical Chemistry Chemical Physics*, 24, pp. 5313-5326.

This dissertation contains tables and figures adapted from the above list of publications. The copyrights for re-using these materials are obtained from the ACS and PCCP publications under the following statements:

- 1) "Reprinted (adapted) with permission from [Sader, S. and Miliordos, E. (2021) "Methane to methanol conversion facilitated by anionic transition metal centers: The case of Fe, Ni, Pd, and Pt," *The Journal of Physical Chemistry A*, 125(11), pp. 2364–2373.] Copyright [2021] American Chemical Society."
- 2) "Reprinted (adapted) with permission from [S. Sader and E. Miliordos, *Phys. Chem. Chem. Phys.*, 2022, **24**, 21583]. Copyright [2022] Physical Chemistry Chemical Physics"
- 3) "Reprinted (adapted) with permission from [E. Claveau, S. Sader, B. A. Jackson, S. N. Khan and E. Miliordos, *Phys. Chem. Chem. Phys.*, 2023, **25**, 5313]. Copyright [2023] Physical Chemistry Chemical Physics"

Table of Contents

Abstract.....	2
Acknowledgments.....	3
List of Publications and Copyrights.....	4
List of Tables	8
List of Figures	9
CHAPTER 1: Overview of Computational Catalysis Methods.....	12
1.1 Introduction and background	12
1.2 Objectives and outline of the dissertation.....	13
1.3 Wave function-based ab initio methods.....	14
1.3.1. Hartree equation and self-consistent field (SCF) method.....	15
1.3.2. The Hartree-Fock method.....	16
1.3.3. Linear Combination of Atomic Orbitals (LCAO)	18
1.3.4. Post-Hartree-Fock methods	19
1.4. Density functional theory (DFT)	20
1.5. Choice of basis sets for anionic systems.....	21
1.6. Pseudo Potential Basis Sets	22
1.7. Calculation of gas-phase chemical reaction rate constant from DFT data	22
CHAPTER 2: Methane to Methanol Conversion	25
2.1. Significance and Background	25
2.2. Current MTM status and previous work	26
2.3. Computational details	28

2.3.1. Multi-reference calculation details for assessing the reference state of metal oxides.....	30
2.4. Metal oxide electronic structure and relevance to methane activation	31
2.5. MTM mediation with cationic vs. anionic TMs	33
2.6. Proposed reaction mechanism of MTM catalyzed by atomic M^-	35
2.7. Results.....	36
2.7.1. DFT calculated reaction geometries and pathway for Pt^- oxidation	36
2.7.2. DFT and CCSD(T) Calculated reaction energy landscape for Pt^- -mediated CH_4 oxidation	39
2.7.3 DFT and CCSD(T) Calculated energy landscape for PCET mechanism in $Pt^- + CH_4$ reaction	40
2.7.4. Pt^- -mediated Methane activation via PCET orbital analysis	41
2.7.5. DFT Calculated reaction energy landscape for Pd^- and Ni^- oxidation reactions.....	43
2.7.6. Alternative MTM reaction pathway for Pt^-	48
2.7.7. CCSD(T)//MN15 Calculated reaction energy landscape for $Fe-(S = 3/2$ and $5/2)$ oxidation reactions	54
2.8. Conclusion and Outlook.....	55
2.9. Impact of ligand addition on catalytic MTM reaction pathway	57
2.9.1 Background on ligands in organometallic chemistry	57
2.9.2. Computational details.....	59
2.9.3. Results and discussions	60
2.10. Conclusion and final remarks	68

CHAPTER 3: TM-Catalyzed Carbon Dioxide Reactions with Unsaturated Alkanes	69
3.1. Significance and Background	69
3.2. Computational details	70
3.3. Proposed catalytic cycle of δ -lactone formation.....	71
3.4. Results.....	72
3.4.1. Atomic Pt-catalyzed carboxylation with ethylene	72
3.5. Discussion	76
3.5.1. Platinum-mediated five-membered metalolactone formation (TS1/TS2) ..	
.....	76
3.5.2. Seven-membered metalolactone formation via (TS3/TS4) or (TS5/TS6) .	
.....	77
3.5.3. Seven-membered metalolactone ring opening and metal release via	
(TS7/TS8/TS9)	78
3.6. Ligand impact on Pt ⁻ -catalyzed carboxylation with ethylene	80
3.6.1. Results and Discussion.....	82
3.7. Conclusions.....	86
References	87
Appendix 1 Supporting Material for Chapter 2	93
Appendix 2 Supporting Material for Chapter 3	122

List of Tables

Table 2.1. MN15/aug-cc-pVTZ relative energy (kcal/mol) and experimental yields	34
Table 2.2. Activation energy barriers for the Ni, Pd, and Pt species with methyl or biphenyl (Bp) ligands	62
Table 2.3. Rate constants k for the reaction steps of Figure 2.14, and $t_{1/2}$, TOF, ΔE for the overall catalytic cycle employing $[M]O^-$ as catalysts	67

List of Figures

Figure 1.1. Schematic representation of the self-consistent field (SCF) method	16
Figure 2.1. Reaction enthalpies for the direct and indirect CH ₄ to CH ₃ OH conversion	26
Figure 2.2. Possible CH ₄ activation mechanisms by metal oxide.....	32
Figure 2.3 Catalytic cycle for the oxidation of CH ₄ to CH ₃ OH by the anionic metal center (M ⁻) using N ₂ O as an oxidant.....	36
Figure 2.4. MN15 intermediate structures (IS) and transition states (TS) for the reaction's steps 1–3 with M = Pt	38
Figure 2.5. Energy diagram for the oxidation step of the metal center (eq 1) for different methodologies.....	39
Figure 2.6. Energy diagram for the methane functionalization steps for different methodologies	41
Figure 2.7. Molecular orbital contours of PtO ⁻ (top), PtOH ⁻ (middle), and CH ₃ ...PtOH ⁻ (bottom) involved in the C-H activation process	43
Figure 2.8. MN15 energy diagram for the oxidation of Ni ⁻ , Pd ⁻ , and Pt ⁻ to NiO ⁻ , PdO ⁻ , and PtO ⁻ by N ₂ O	44
Figure 2.9. RCCSD(T)//MN15 energy diagram for the MO ⁻ + CH ₄ → M ⁻ + CH ₃ OH reaction (M = Ni, Pd, Pt)	47
Figure 2.10. RCCSD(T)//MN15 energy diagrams for several pathways of the Pt ⁻ + CH ₄ + N ₂ O → Pt ⁻ + CH ₃ OH + N ₂ reaction	49
Figure 2.11. Alternative reaction pathways for CH ₄ activation.....	50
Figure 2.12. RCCSD(T)//MN15 (S=5/2) and qCCSD(T)//MN15 (S=3/2) energy diagrams for the radical and 2+2 mechanisms of the Fe ⁻ + CH ₄ + N ₂ O → Fe ⁻ + CH ₃ OH + N ₂ reaction.....	55

Figure 2.13. Ethylene-platinum orbitals overlap showing competing π and σ bonds	58
Figure 2.14. Optimized geometries of structures of $[\text{Pd}(\text{CH}_3)_4]^-$ (top) and $[\text{Pd}(\text{Bp})_2]^-$ (bottom) catalysts used in the MTM pathway	59
Figure 2.15. Structures of all intermediates and transition states for the $\text{CH}_4 + \text{N}_2\text{O} \rightarrow \text{CH}_3\text{OH} + \text{N}_2$ reaction facilitated by $\text{PdO}^-(\text{CH}_3)_4$	60
Figure 2.16. MN15/TZ potential energy diagram for the $\text{CH}_4 + \text{N}_2\text{O} \rightarrow \text{CH}_3\text{OH} + \text{N}_2$ reaction facilitated by $[\text{PdO}(\text{CH}_3)_4]^-$	61
Figure 2.17. Natural orbital (NO) analysis of doublet $[\text{Pd}(\text{CH}_3)_4]^-$ showing the spin density of the singly occupied orbital localized mainly on metal and the two bent methyl groups	65
Figure 3.1. Different routes leading to lactone formation from CO_2 and two ethylene molecules. $\text{M} = \text{Pt}^-, \text{Pd}^-, \text{Ni}^-$ in free and ligand-complexed forms	72
Figure 3.2. Free energy profile for Pt^- -mediated C-C coupling (TS1 & TS5) and lactone formation (TS9)	73
Figure 3.3. Free energy profile for the Pt^- -mediated C-C coupling (TS1), C-O coupling (TS6), and lactone formation (TS9). Energies are relevant to the reactants	74
Figure 3.4. Free energy profile for the Pt^- -mediated C-C coupling (TS3) and C-O coupling (TS2) and lactone formation (TS7). Energies are relative to the reactants	75
Figure 3.5. Free energy profile for the Pt^- -mediated C-O coupling (TS2), C-C coupling (TS4), and lactone formation (TS8). Energies are relevant to the reactants	75
Figure 3.6. Optimized geometries of intermediates and transition states for metalolactone formation	76
Figure 3.7. Natural orbital (NO) representation showing the spin density of the single electron in Pt^-	77

Figure 3.8. Optimized geometries of intermediates and transition states for 7-membered metalolactone formation	78
Figure 3.9. Optimized Pt ⁻ -based catalyst	80
Figure 3.10. Energy landscape for atomic (right) and complexed Pt ⁻ (left) for Pathways A & B	81
Figure 3.11. Energy landscape for atomic (right) and complexed Pt ⁻ (left) for pathways C & D	81
Figure 3.12. Natural orbital (NO) diagram showing the spin density of the single electron on atomic and complexed Pt ⁻	82
Figure 3.13. Ligand effect on the geometrical shape of reactants for TS1 (C-C) coupling and TS2 (C-O) coupling	83
Figure 3.14. Ni ⁻ (Bp) catalyzed CO ₂ reaction with ethylene.....	84
Figure 3.15. Pd ⁻ (Bp) catalyzed CO ₂ reaction with ethylene	84

1. CHAPTER 1: Overview of Computational Catalysis Methods

1.1. Introduction and background

The growing demand for clean and sustainable energy resources is driving the transformation of the world's heavy reliance on petroleum into more developed energy systems. Solar cells, electric cars technology, and biofuels are a few examples of current technologies that have proven to be efficient in mitigating both world energy requirements and climate change phenomena. More recently, natural gas and carbon capture and utilization have emerged as ubiquitous and free chemical feedstocks to synthesize useful chemicals such as methanol and other fine chemicals. However, for those new technologies to be practically efficient, several obstacles need to be overcome pertaining to the cost of infrastructures required by these new technologies as well as transportation and energy conversion cost. Chemical catalysis plays a pivotal role in developing viable routes in energy conversion, particularly, transition metals owing to their efficiency and reliability. The process of designing and developing new and cost-effective catalysts is a challenging process that needs to be addressed before it can be practically useful. It requires knowledge of the mechanisms and advanced methods that aid in understanding catalyst behavior and improvement possibilities. Computational chemistry is a routinely utilized tool in studying various chemical concepts and transformations due to its rising accuracy and efficiency. Perhaps, organometallic catalysis is one area where quantum chemical calculations have proven to play a central role as a missing piece in understanding catalytic mechanisms. Density Functional Theory (DFT) is a commonly utilized method in computational catalysis due to its exceptionally low computational cost. Still, it has its shortcomings in cases of open shell multireference systems such as TMs, plus DFT data accuracy is strongly correlated with the right choice of functional.¹ Therefore, applying advanced electronic correlation methods such as Multi-Reference

Configuration Interaction (MRCI) is fundamentally important in understanding the status of the electronic configuration of transition metals (TMs) and provides an accurate prediction of the electronic structure of TM-containing molecules. Similarly, CI methods are significant in situations involving bond-forming or breaking stages, a feature typically missing in singly referenced methods such as Hartree Fock and DFT. Equally important, methods such as coupled clusters are critical for both accuracy and size extensivity needed to accurately describe catalytic pathway energetics.² Among intensely researched areas are methane to methanol conversion and CO₂ sequestration and utilization due to their economic and ecological impacts. Both C-H activation including MTM pathways and catalytic conversion of CO₂ have been widely explored previously using cationic and neutral forms of TMs in their atomic and oxide forms,³⁻⁸ however, the potential of negatively charged TMs in CO₂ and TM-oxides in MTM pathways is still poorly explored.

1.2. Objectives and outline of the dissertation

The goal of this dissertation is to theoretically study the catalytic potential of negatively charged TM ions in MTM and CO₂ carboxylation reactions with unsaturated hydrocarbons. The study is mainly focused on the energetics of the gas phase catalytic pathways using DFT and post-HF electronic correlation methods, geometries, and electronic structures of intermediates and transition states. Additionally, the catalytic efficiency improvement through ligand design is also examined in both targeted reactions. The efficiency of each catalytic pathway is assessed using the energetic span model which provides a quantitative description of catalyst performance through turnover frequency (TOF) calculations.^{9, 10} Our hypothesis behind using anionic TM centers is that higher activation power is attributable to their capability to populate the anti-bonding C-H orbital in methane for example, thus disrupting the bond.¹¹ On the other hand, finding ligands that enhance

the electron affinity (E_{ea}) of the metal center to enable them to regain their electrons at the end of the cycle is a challenging task. Moreover, the weak ion-dipole interaction force between the anionic metal center and hydrogen atom of generated methanol, as compared to that in cationic metal and oxygen of methanol, results in a short interaction period with the created product (CH_3OH), facilitating the product release and preventing over-oxidized products. The following is a concise and general description of the computational methods used in this dissertation. The complete and detailed accounts of the electronic structure theory can be found in Modern Quantum Chemistry, a book by Szabo and Ostlund.¹²

1.3. Wave function-based ab initio methods

Electronic structure calculations based on analytical approximate solutions of Schrödinger's equation (SE) provide the core requirement for most common computational chemistry methods. The SE can be described as time-independent SE with the following formula:

$$\hat{H}\Psi(\mathbf{R}_1, \mathbf{R}_2 \dots \mathbf{R}_N, \mathbf{r}_1, \mathbf{r}_2 \dots \mathbf{r}_n) = E\Psi(\mathbf{R}_1, \mathbf{R}_2 \dots \mathbf{R}_N, \mathbf{r}_1, \mathbf{r}_2 \dots \mathbf{r}_n) \quad (1.1)$$

Where \mathbf{R} and \mathbf{r} are the coordinates of the nuclei and the electrons respectively.

The Hamiltonian operator \hat{H} for the time-independent, non-relativistic Schrodinger equation is:

$$\hat{H} = -\sum_A \frac{1}{2M_A} \nabla_A^2 - \sum_i \frac{1}{2} \nabla_i^2 - \sum_{iA} \frac{Z_A}{r_{iA}} + \sum_{A<B} \frac{Z_A Z_B}{r_{AB}} + \sum_{i<j} \frac{1}{r_{ij}} \quad (1.2)$$

Where A and B are the nuclear indices and i and j are the electronic indices. The first two terms in the Hamiltonian represent the kinetic energy of the nuclei and electrons, respectively. The

third, fourth, and fifth terms involve the potential energy due to the attraction of the electrons and nuclei, the nuclear-nuclear repulsions, and the electron-electron repulsion, respectively. Applying the Born-Oppenheimer approximation de-couples the electronic and nuclear degrees of freedom and the Hamiltonian takes the form:

$$\hat{H}_{ele} = -\sum_i \frac{1}{2} \nabla_i^2 - \sum_{iA} \frac{Z_A}{r_{iA}} + \sum_{A<B} \frac{Z_A Z_B}{r_{AB}} + \sum_{i<j} \frac{1}{r_{ij}} \quad (1.3)$$

Here, we focus on the electronic motion which can be described assuming the nuclear motion is omitted.

1.3.1. Hartree equation and self-consistent field (SCF) method

Hartree proposed the idea that individual electrons can be separated as well, and many-electron wave function would be a product of one-electron wave functions ϕ as follows:

$$\psi_{ele}(\mathbf{r}_1, \mathbf{r}_2 \dots \mathbf{r}_n) = \phi_1(\mathbf{r}_1) \phi_2(\mathbf{r}_2) \dots \phi_n(\mathbf{r}_n) \quad (1.4)$$

This wave function assumes that an individual electron moves in a mean-field (V_i^{eff}) of all other electrons and the solution of individual Hartree equations depends on the iterative solution of all other equations via (V_i^{eff}). The iterative process is called self-consistent field (SCF)¹³ as shown below in figure 1.1 :

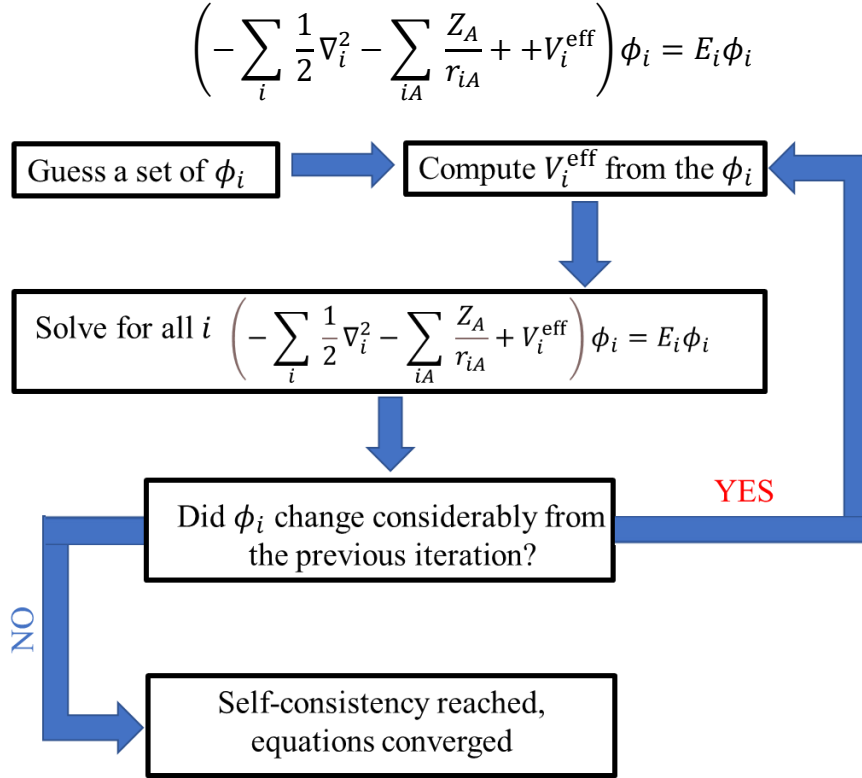


Figure 1.1. Schematic representation of the self-consistent field (SCF) method.

1.3.2. The Hartree-Fock method

Because the Hartree product wave function is not antisymmetric (as required by the Pauli principle), it does not result in sign adjustment upon exchanging two electrons (which it should), and the Slater determinant (SD) which was introduced by Fock to represent the wave function as follows:

$$\psi(\mathbf{r}_1, \mathbf{r}_2 \dots \mathbf{r}_n) = \frac{1}{\sqrt{n!}} \begin{vmatrix} \phi_1(r_1) & \phi_2(r_1) & \dots & \phi_n(r_1) \\ \phi_1(r_2) & \phi_2(r_2) & \dots & \phi_n(r_2) \\ \phi_1(r_n) & \phi_2(r_n) & \dots & \phi_n(r_n) \end{vmatrix} \quad (1.5)$$

Using this determinant, a multi-electron system can be represented with a set of spatial and spin functions where each row uses a different spin-orbital (ϕ) for the same electron while each

column uses a different electron with the same spin-orbital. The consequence of such construction is that switching any electron pair, by interchanging two rows or two columns, results in ψ sign change satisfying the Pauli-exclusion principle. Based on the HF method, the energy of the system is obtained variationally by equation 1.6 assuming a normalized wavefunction and the term $\langle\langle\psi | \psi\rangle\rangle = 1$:

$$E_{HF} = \frac{\langle\psi|\hat{H}_{\text{ele}}|\psi\rangle}{\langle\psi|\psi\rangle} = \langle\psi|\hat{H}_{\text{ele}}|\psi\rangle \quad (1.6)$$

To obtain ϕ , rearrange E_{HF} , and obtain the Fock equation solved in a Self-Consistent Field (SCF) approach.

Here, the electronic Hamiltonian consists of electronic energy, nuclear attraction, and electron-electron repulsion terms as follows:

$$E_{HF} = \sum_{i=1}^{N_{\text{elec}}} h_i + \frac{1}{2} \sum_{i=1}^{N_{\text{elec}}} \sum_{j=1}^{N_{\text{elec}}} (J_{ij} - K_{ij}) + V_{\text{nn}} \quad (1.7)$$

Where h_i is one-electron energy term that comprises both kinetic energy and electron-nuclear attraction terms as follows:

$$h_i = -\frac{1}{2} \nabla_i^2 - \sum_{iA} \frac{Z_A}{r_{iA}} \quad (1.8)$$

J_{ij} is an integral obtained by the Coulomb operator, arising from the Coulomb repulsion between electrons, K_{ij} is obtained by the exchange operator, it ensures anti-symmetry and removes the self-interaction arising from the J_{ij} integrals.

1.3.3. Linear Combination of Atomic Orbitals (LCAO)

The solution to the one-electron wave function such as the hydrogen atom case, gives the atomic orbital as an analytical expression, while the solution to the HF wave function is provided by the molecular orbitals:

$$\phi_i = \sum_{\mu=1}^n c_{i\mu} \chi_{\mu} \quad (1.9)$$

The sum over μ runs over all n atomic orbitals of the atoms. The $c_{i\mu}$ are called molecular orbital coefficients and are optimized to minimize the total energy χ_{μ} is the basis function, for example, in the H_2 molecule, this simple minimal basis set leads to two HF orbital solutions based on the 1s AOs.

The HF SCF produces in addition to energy, a set of molecular orbitals, and the number of the later depends on the number of basis functions (BFs) used. Using small numbers of BFs results in crude results only, while using an infinite number of BFs brings the HF energy close to the exact solution of HF equations. However, a balance must be achieved between the quality of results and the level of theory since using many BFs significantly raises the cost of computation, especially for post-HF.

While a HF wave function advantage is producing size-consistent energy, both its variational nature and lack of electronic correlation make the HF energy always higher than the exact value. It follows that the HF method has limited value in chemical applications, instead, HF has been used today only as a reference wave function and reference energy for correlated wave-function methods such as coupled-cluster (CC) theory.

1.3.4. Post-Hartree-Fock methods

For chemical systems that involve TMs, diradicals, and bond stretching, two or more different configurations might be important to accurately describe the wave function. Choosing one of them leads to an inaccurate energy description of the system. This inadequacy in single-referenced methods required the development of the Multi-Configuration Self-Consistent Field (MCSCF) method, which is more commonly named multireference method. Several methods have been developed using this approach such as the Complete Active space self-consistent Field (CASSCF) method where both the coefficients in front of the different configurations and the orbitals for each determinant are optimized. Another MCSCF method used in this dissertation is the multi-reference configuration interaction (MRCI) as described in section 1.3.4.2.

1.3.4.1. Complete Active Space Self-Consistent field (CASSCF)

In this method, only orbitals that involve large variations in the electronic configurations (chemically active) are included in the active space and undergo full Configuration Interaction (Full CI). For example, consider the d-orbitals of TMs. All other orbitals are either frozen (always doubly occupied in the core) or virtual (empty). The wave function in CASSCF is obtained by optimizing a linear combination of configuration state functions (CSFs) that comprise all possible occupations of the orbitals and electrons in the active space. The active space specification is important for the accuracy of proper bond cleavage and excited states descriptions.

1.3.4.2. Multi-reference configuration interaction (MRCI)

In this method, more configurations are added to the wave function by promoting electrons from the active to the virtual orbitals. The wave function is obtained by optimizing the linear combination of all possible state functions. Thus, CI will provide a better representation of correlated systems having more electronic configurations compared to CASSCF. To solve the size-consistency problem in MRCI, it is often approximated with the Davidson correction MRCI+Q.^{14, 15}

1.3.4.3. Coupled cluster method (CC)

The lack of size-consistency^{16, 17} and excessive computational cost of MRCI result in the development of coupled cluster theory. Unlike the MRCI method where the wave function is expressed as a linear combination of individual state functions, the CC uses an exponential operator to express all possible excitations such as single (CCS), double (CCSD), and triple excitations (CCSDT), etc... A special case arises when the triple excitation is included in scaling the CCSD where triple excitation is added using perturbation theory (CCSD(T)) avoiding the prohibitive computational cost of CCSDT. The CCSD(T) is referred to as the “gold standard of quantum chemistry” provided a single determinant serves as a proper reference.

1.4. Density functional theory (DFT)

In this method, the energy is obtained as a functional of the electronic density of the system, thus, neither prior knowledge of the wave function nor solving SE is required. The mathematical structure of DFT reduces the prohibitive computational cost resulting from exponential scaling with the number of electrons required to solve SE into the dimensionality of 3 in DFT, regardless of the number of electrons of the molecules. Such features make DFT an efficient method for large systems. The DFT method has passed through several transformative stages of development

starting from Hohenberg–Kohn theorem¹⁸ and ending with the Kohn-Sham DFT¹⁹ functional that has the form :

$$E[\rho] = T[\rho] + E_{ext}[\rho] + E_{Coul}[\rho] + E_{xc}[\rho] \quad (1.10)$$

Here, $T[\rho]$ is the kinetic energy of non-interacting electrons, $E_{ext}[\rho]$ is the electron-nuclear attraction term, $E_{Coul}[\rho]$ is the electron repulsion term and $E_{xc}[\rho]$ is the exchange and correlation potential term. The later term replaces the exact exchange term in the HF method making DFT superior to HF, having the additional feature of correlation effects. Unfortunately, the exact expression of the $E_{xc}[\rho]$ is unknown and is the subject of much method development research.²⁰ The exact functional has been approximated with several empirical modules to give a reasonable electronic energy result for complex systems. Thus, the selection of functional is critical to obtain accurate results, which may be sensitive to functional choice. For example, adding an empirical dispersion correction such as the B3LYP-D3 functional significantly improves results for systems with long-range interactions that usually B3LYP²¹ alone fails to describe. Noteworthy, the MN15 functional used in this dissertation is one of the Minnesota series of functionals proposed by Truhlar's group.²² This type of functional has been well parameterized for both main group and transition metal elements and is thus very suitable in organometallic catalytic reaction modeling.

1.5. Choice of basis sets for anionic systems

For anions or electron-rich atoms/pairs, the basis set must be augmented with diffuse functions to allow the electron density to expand into a larger volume. On the other hand, the addition of polarization functions is necessary to give more freedom to electrons to move away

from each other, thus reducing electron-electron repulsion. This is done by adding a basis function of a higher angular momentum to the existing one, for example, for s-type orbital, we add a set of p orbitals, and for p-electrons, we add a set of d-type orbitals. The correlation consistent basis sets used in this dissertation denote the use of maximum electron correlation energy for each atom, while the valence denotes it has been applied to valence electrons only.

1.6. Pseudo Potential Basis Sets

For late (heavy) transition metals, these potentials are used to reduce the computational cost by describing the inner (core) electrons by a potential that is placed in the Hamiltonian. Their implementation is also important to account for the relativistic effect of these late TMs. These basis sets comprise two parts: the effective core potential (ECP) describing the inner electrons and the basis set describing the valence electrons. For example, the Los Alamos National Lab two double zeta basis set (LANL2DZ) is one of the commonly used effective core potential (pseudo potential) in computational chemistry, proposed by Hay and Wadt^{23, 24} that involves relativistic effects for elements in the fifth and sixth periods; however, it only provides acceptable accuracy suitable for geometry optimization but not energetics. On the other hand, for accurate energetics, a higher level of theory basis sets is used.

1.7. Calculation of gas-phase chemical reaction rate constant from DFT data

There are two important assumptions when using *ab-initio* calculations to calculate thermodynamic data. First, the equations are derived for non-interacting particles, thus, legitimate only for an ideal gas. Second, the first low-lying and higher excited states are inaccessible, thus, it is applicable only for the ground state of the interacting molecules²⁵. The thermodynamic data generated by Gaussian software²⁶ such as entropy, free energy, and heat capacity are heavily dependent on partition function $q(V, T)$ calculations which have four contributions: translational,

vibrational, and rotational which comprises electronic motion (linear, non-linear, and electronic) according to equation 1.11:

$$Q_{\text{tot}} = Q_{\text{trans}} \times Q_{\text{vib}} \times Q_{\text{rot}} \times Q_{\text{elec}} \quad (1.11)$$

The detailed mathematical formulas required to calculate each component are based on statistical mechanical modeling and are discussed in detail in “Molecular Thermodynamics” by McQuarrie and Simon²⁷. For a given reaction that involves an activation barrier, the Transition State Theory²⁸ rate constant can be obtained based on the following equation:

$$k^{\text{TST}}(T) = \sigma \frac{k_{\text{b}}T}{h} \frac{Q^{\text{TS}}(T)}{N_{\text{A}}Q^{\text{R}}(T)} e^{-\frac{V^{\ddagger}}{k_{\text{b}}T}} \quad (1.12)$$

where σ is the reaction path degeneracy, k_{b} is Boltzmann’s constant, T is the temperature, h is Planck’s constant, N_{A} is Avogadro’s number (it disappears for unimolecular reaction rate constants with units of s^{-1}). V^{\ddagger} is the difference in the potential energy between the transition state (TS, assumed to be located at the saddle point on the PES) and the reactant(s) (zero-point energy contributions are included in the partition functions). Q^{TS} and Q^{R} denote the total partition functions of the TS and the reactant(s) with the translational partition functions expressed in per unit volume. Q^{TS} excludes the reaction coordinate. In the calculation of $\Delta G^{\ddagger}(T)$ (except when the tunneling correction computation is used)²⁹, the imaginary frequency associated with the reaction coordinate degree of freedom is removed from the vibrational partition function of the transition state and, as a result, from the kinetic treatment. Thus, we express Q^{TS} by the following formula:

$$Q_{TS}(T) = Q_{trans}^{TS} \times Q_{vib}^{TS} \times Q_{rot}^{TS} \times Q_{ele}^{TS} \quad (1.13)$$

after replacing Q^{TS} and Q^R from the above equation to the equation of k^{TST} and some algebraic manipulations, the zero-point energy corrections and entropy terms are incorporated in the exponential part (thus V^\ddagger converts to ΔG), while the V introduced via the Q_{trans} terms remain in the pre-exponential factor and the final formula for rate constant will be expressed as shown in eq 1.14 below²⁹:

$$k^{TST}(T) = \sigma \frac{k_b T}{h} \left(\frac{RT}{P^0} \right)^{\Delta n} e^{-\frac{\Delta G^\ddagger(T)}{k_b T}} \quad (1.14)$$

where $\Delta G^\ddagger(T)$ represents the standard Gibbs free energy of activation ΔG^0 at temperature T , Δn is 1 or 0 for gas-phase bimolecular or unimolecular reactions, respectively; RT/P^0 has the unit of the inverse of a concentration).

2. CHAPTER 2: Methane to Methanol Conversion

2.1. Significance and Background

Presently, the MTM pathway is gaining significant attention from the scientific community due to its environmental and economic impact. Although CH_4 exists at a low atmospheric concentration (compared to CO_2), its global warming potential is 28-36 times higher than that of CO_2 ,³⁰ due to its high atmospheric residence time and heat absorptivity. Typically, CH_4 can be found in coal, natural gas, and oil. It can also be produced by livestock and other agricultural activities as well as by the decay of municipal solid waste landfills.³⁰ Methane's vast abundance and sustainability make it an excellent feedstock and source of convertible energy to build several chemically and industrially important molecules such as methanol, ethylene, ethanol, ethylene glycol, isopropanol, and propylene glycol, etc.³¹

Due to the growing demand, methanol came to the forefront of extensively produced chemicals worldwide due to its scientific and industrial importance.^{32, 33} About 110 million metric tons are produced worldwide, 40% of which is converted to fuel.³⁴ Historically, it is produced by distillation of burning wood but with low capacity. However, it can also be produced at industrial levels from both CH_4 and CO_2 , raising the economic importance of these molecules and providing a solution to mitigate their negative environmental impact. Methanol economy gained its solid ground owing to its unique chemical, physical, and safety properties. Firstly, it is less volatile and flammable compared to gasoline. Secondly, methanol vapor is only marginally denser than air which accounts for its low combustibility and thus its high safety profile. Lastly, methanol ignites about 25% faster than gasoline but releases heat at 1/8 the rate of that of gasoline. To sum up, the above-mentioned properties make methanol hard to ignite compared to gasoline causing less damage when burned and safer to transport and store compared to gaseous CH_4 .³⁰

In essence, direct, and selective conversion of CH₄ in MTM pathway is contingent upon developing a highly selective catalyst that ensures a high conversion to methanol with minimal side products. However, activating CH₄ is a high-stakes challenge owing to its inertness as a closed-shell molecule. Both methane's ionization and C-H dissociation energies^{35,36} entail a high oxidation energy requirement. Moreover, its oxidation to methanol is both an intricate and highly sensitive process concerning its stoichiometric ratio with O₂ that demands a high level of thermal control to avoid combustion.³⁷ In addition to thermodynamic difficulty, selectivity is yet another obstacle that needs to be addressed for the MTM pathway to be practical. Thus, MTM imposes a challenge for scientists and environmentalists and represents a promising pathway among other sustainable energy methods.

2.2. Current MTM status and previous work

Industrially, CH₄ is transformed to methanol through a costly and endothermic centralized process where natural gas is steamed and passed over a catalyst in a steam reformer producing syngas initially. The latter (a mixture of H₂ and CO) is passed over a catalyst producing methanol.³⁷ Thermodynamically, producing methanol via the syngas pathway entails as much as +27.6 kcal/mol of steam energy as shown in figure 2.1.

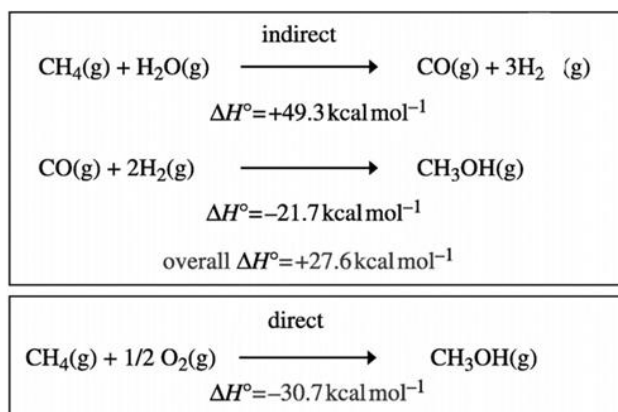


Figure 2.1. Reaction enthalpies for the direct and indirect CH₄ to CH₃OH conversion.

Moreover, both the hazardous shuttling of CH₄ to the main syngas production plant and the low cost of other energy alternatives including crude oil represent barriers confronting methane utilization and commercialization. A comprehensive detailed study on syngas history and production is discussed in a review paper.³¹ At the laboratory level, several experimentalists have reported a single-step methanol synthesis using different TM with homogenous and heterogenous catalysis. However, the low conversion yield and promiscuous selectivity are hampering further development of these catalysts.^{5, 38-44} On the other hand, any attempts to enhance methanol yield will be at the expense of catalyst selectivity.⁴⁵ Biological enzymes such as methane monooxygenase can also convert CH₄ to methanol using their catalytic binding pockets. Another work⁴⁶ reported that methanotrophic bacteria can undertake MTM reactions utilizing redox active copper or iron centers based on bacterial subtypes; however, factors like scalability, genetic engineering intricacy, limited rate of conversion as well as a co-enzyme requirements are hindering the commercialization of this method.⁴⁷ Concurrently, research spearheaded by Chan et al. developed a selective and efficient molecular tri-copper cluster catalyst with different ligands inspired by the monooxygenase enzyme catalytic binding pocket.⁴⁸ However, its success is challenged by technical difficulties pertaining to experimental design which requires continuous removal of (CH₃OH/H₂O) and continuous supply of oxidant (H₂O₂/H₂O) in the reactor.⁴⁸ On the other hand, metal oxides are a common family of catalysts with unique properties that catalyze several important reactions, particularly oxidation (selective and total), acid-base reactions, depollution, and biomass conversion.⁶ The fact that oxide surfaces are covered by oxide O²⁻ anions, as their size is much larger than that of Mⁿ⁺ cations, adds a nucleophilic character to the catalyst and possibly improves catalyst reactivity and selectivity compared to atomic catalysts. The pronounced catalytic efficiencies of metal oxides have stimulated further research to be used in

homogenous catalysis. One tangible advantage of metal oxides is overcoming the endothermic nature of oxidative addition of methane with bare TM metal ions M^+ ($M = \text{Ti, V, Co, Fe, Nb, Rh, Sc, Y, La, Lu, Ni, Zn, and U}$).^{4, 8, 49-51} However, cases where the bare TMs (M^+) are electronically excited such as (Ti^+, Cr^+) or the kinetic excitation energy is compensating for the oxidative addition energy cost, are exceptions, and makes those bare TMs superior to their TM oxides counterparts in terms of catalytic power.⁴

One of the nascent attempts to explore the role negatively charged TM atoms play in the MTM pathway was published by Msezane et al. where anionic gold (Au^-) was theoretically studied using dispersion-corrected DFT.⁵² In a different work, the authors extended their previous study to include atomic $\text{Y}^-, \text{Ru}^-, \text{At}^-, \text{In}^-, \text{Pd}^-, \text{Ag}^-, \text{Pt}^-$, and Os^- .⁵³ Although their work involved mainly DFT and thermodynamics calculations, the authors have shown that anionic catalysts may make a significant contribution to reducing the energy requirements for the MTM pathway, especially in stabilizing the transition states. The first systematic experimental investigation of the Pt^- potential in C-H activation belongs to Bowen et al.⁵⁴ Bowen's work has provided valuable insight into the mechanism underlying C-H activation by Pt^- and casts doubt on the previously accepted inadequacy of Pt^- in methane activation.⁵⁵ His work is the first experimental evidence of Pt^- capability of activating CH_4 molecule proven by mass spectroscopy data as well as computational study.⁵⁴

2.3. Computational details

Quantum calculations were carried out using Gaussian 16 and MOLPRO packages.^{26, 56} Initially, we investigated the wave function stability of all intermediate and transition states by applying the stable=opt option in Gaussian; the obtained wave function was used as a reference for subsequent geometry optimizations of intermediates and transition states (TS) which were

obtained with DFT methods using the Minnesota hybrid exchange-correlation functional (MN15).⁵⁷ Real and imaginary frequencies were obtained to confirm that local minima (stationary points) or 1st order saddle points (transition states) were reached. The correlation consistent polarized valence triple zeta basis set augmented with diffuse functions aug-cc-pVTZ^{58, 59} was used for all atoms. These diffuse functions are essential for the accurate description of the chemical properties of anions, which is particularly important in our studied systems. To account for Pt relativistic effect, the Stuttgart relativistic effective core pseudo-potential (ECP) was utilized to represent the 60 inner electrons of Pt atom ($1s^2$ through $4d^{10}$) and 28 inner electrons of Pd atom ($1s^2$ through $4d^8$).⁶⁰

In the cases of negatively charged ions, the calculations of correlation energy are generally more demanding than in cations or neutral atoms due to more efficient screening of the nucleus by electrons. Thus, it is of paramount importance to consider accurately the electron correlation effects in such systems. In fact, the stability of a negative ion depends on how competitively the extra electron experiences the attractive force from the nucleus against other electrons.⁶¹

To this end, we performed complete active space self-consistent field (CASSCF) single-point energy calculations for these structures to assess the multireference nature of wave function. For Ni^- , Pd^- , and Pt^- , the doublet and quartet spin states are all having a high single-reference character. The dominant configuration has a coefficient of 0.85 or larger. For these singly referenced systems we performed restricted coupled cluster calculations with single, double, and perturbative triple electron replacements, RCCSD(T).^{17, 62} Previous work done by our group showed that single point CCSD(T) energy using the MN15 optimized geometries are quite accurate for single-reference nature systems.¹¹ In the case of iron quartet spin structures, we further performed internally contracted multireference configuration interaction (MRCI)⁶³ with single and

double electron replacements of active electrons of the CASSCF wave function to the virtual orbital space to assess their multireference nature. The quartet RCCSD(T) energies of iron were obtained through a combination of RCCSD(T) of the sextet and MRCI of the quartet-sextet energy splitting through the following formula:

$$E \left[\text{qRCCSD(T)}; S = \frac{3}{2} \right] = E \left[\text{RCCSD(T)}; S = \frac{5}{2} \right] + E \left[\text{MRCI}; S = \frac{3}{2} \right] - E \left[\text{MRCI}; S = \frac{5}{2} \right]$$

(2.1)

Here, qRCCSD(T) is the quasi-RCCSD(T) energy of the quartet spins state of Fe, and E(X) is the total electronic energy. The validity of this approach lies in the single-reference nature of the high-spin $S = 5/2$ wave function (ferromagnetic coupling of the electronic spins). The active space selection for both MRCI and CASSCF calculations was based on valence orbitals actively participating in the chemical reaction studied. However, non-participating orbitals such as C-H bonds and 2s of oxygen were closed (frozen) to reduce the computational cost of calculations.

Another important factor, especially for 2nd and 3rd row TMs, is the Spin-Orbit (SO) coupling. SO calculations at the MRCI level were done for Pt-containing compounds through diagonalization of the Breit- Pauli Hamiltonian ion based on their lowest energy CASSCF wave functions.⁶⁴

2.3.1. Multi-reference calculation details for assessing the reference state of metal oxides

All calculations were performed using MOLPRO 2015.1 software package⁶⁵ and the C_{2v} point group symmetry was assigned to all structures of studied metal oxides. The molecular

orbitals were optimized at the state-averaged complete active space self-consistent field (CASSCF) level. The active space for PtO^- and PtO^- consists of 15 electrons allocated as follows: 4 in A_1 , 2 in B_1 , 2 in B_2 , and 1 in A_2 orbitals, which correspond to 5s and 4d atomic orbitals of metal and 2p of oxygen at large M–O distances (we closed 1s of oxygen). We expanded the active space to include three additional orbitals (3p orbitals of oxygen at infinity) resulting in 12 active orbitals ($5A_1$, $3B_1$, $3B_2$, $1A_2$). The inclusion of these orbitals was necessary to obtain better electron affinities, better convergence, and smoother PECs. For NiO^- and FeO^- , the active space consists of 15 electrons/ NiO^- and 13 electrons/ FeO^- allocated as follows: 4 in A_1 , 2 in B_1 , 2 in B_2 , and 1 in A_2 orbitals.

2.4. Metal oxide electronic structure and relevance to methane activation

It is well known that transition metal oxides exist in two electronically equivalent forms; TM-oxyl ($\text{M}^{n+}\text{O}^{\bullet-}$) and TM-oxo ($\text{M}^{(n+1)+}\text{O}^{2-}$) species.^{66, 67} Factors such as the nature of metal, the valence of the metal core, and the first coordination sphere can dictate which form is prevalent. Such distinction is important in determining the reactivity and reaction mechanisms of TM oxides with CH_4 . In this regard, the “oxo” form is believed to perform a proton-coupled electron transfer (PCET) or [2+2] while “oxyl” can perform hydrogen atom transfer (HAT) as shown in figure 2.2

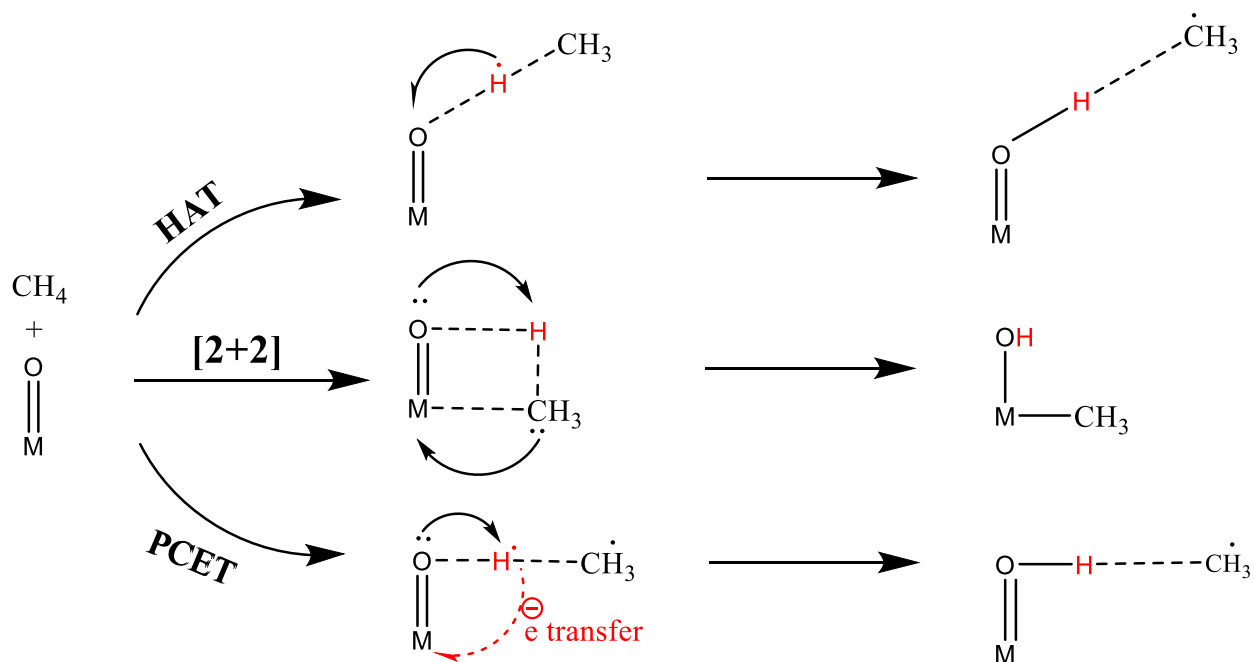


Figure 2.2. Possible CH₄ activation mechanisms by metal oxide.

Experimentally, an oxyl form, for example, can be confirmed with EPR and IR methods that show a low valency of the metal center.⁶⁷ However, to understand the relative stability of these two forms, we compare the energies of the complex (i.e. metal oxide molecules) with the reactants $\text{M}^{(n+2)+} + \text{O}^{2-}$ and $\text{M}^{(n+1)+} + \text{O}^-$. The latter is always lower in energy and their separation is determined by the ionization energy (IE) of the metal ($\text{M}^{(n+1)+}$ to $\text{M}^{(n+2)+}$). The O^{2-} ion is unstable with respect to O^- (negative electron affinity, E_{ca}).⁶⁸ The energy required to go from the oxyl to the oxo fragments, $\text{IE} - E_{\text{ca}}$ ($E_{\text{ca}} < 0$), is proportional to the square of the metallic charge, as can be observed by the experimental values⁶⁸, and inferred by the hydrogenic model.⁶⁹ It follows that the oxo form will dominate whenever the oxidation state of the metal permits, due to oxo's relative stability compared to oxyl. Otherwise, the oxyl form will win over the oxo, especially when progressing toward late transition metals, where the occupancy of π -antibonding metal d orbitals increases and metal-oxo bonds become weaker and more reactive. In fact, metal oxo species are

scarcely reported in the literature beyond group 8 unless they exist in special coordination geometries such as square-pyramidal, trigonal-pyramidal, and, importantly, square-planar.⁷⁰ This type of behavior has been so far identified as the “oxo-wall” phenomenon.^{66, 71, 72} This has been confirmed computationally by our group recently.⁷³ The oxyl character of M-O implies an elongation of the M-O bond and the presence of high spin density on the oxygen atom which can also be confirmed computationally.

From a different angle, since the methane C-H bond is considerably strong ($pK_a = 46$), it requires a strong base (the oxygen of metal oxide) to be extracted. This suggests that metal-oxygen bond dissociation energy can be a major factor in methane activation. This was supported by our recent publication where the acidity of the metal hydroxides of (NiO^- , PdO^- , PtO^-) is reversely correlated with the activation barrier of methane.¹¹

2.5. MTM mediation with cationic vs. anionic TMs

To highlight the distinctions between metal oxide cations and anions in terms of their selectivity towards methanol production, we compared the energy requirements for both methanol and other hydrogenated products for cationic, neutral, and anionic metal oxides. Experimental research on the $MO^+ + CH_4$ reaction in the gas phase has been done for $M = Ni, Pd,$ and Pt .⁷⁴ Three distinct reaction pathways have been reported: $M^+ + CH_3OH$, $MCH_2 + H_2O$, $MOCH_2 + H_2$ ($M = Pd$), and $MH_2^+ + OCH_2$ ($M = Pt$) were observed. Table 2.1 contains the relative energy for the three product types and the three metals. Our numerical values for Ni and Pd differ significantly (20–30 kcal/mol in some situations) from those of reference⁷⁴, but the relative energies of the various products are consistent. There was no energetics for Pt in reference⁷⁴ reported. The major reaction products are $M^+ + CH_3OH$ due to the high activation barriers for the oxidation of methanol to formaldehyde (CH_2O) on the M^+ center, even though $MOCH_2^+ + H_2$ for $M = Ni$ and Pd are the

lowest energy products.⁷⁴ In contrast, PtO⁺ allows for the 98% yield of the lowest energy PtCH₂⁺ + H₂O products (see Table 2.1). The selective oxidation of methane to methanol turns out to be extremely poorly mediated by PtO⁺ (0% yield; see Table 2.1). Compared to PtCH₂⁺ + H₂O, the production channel for methanol is 36.9 kcal/mol more endothermic. The two channels PtCH₂ + H₂O and Pt + CH₃OH become almost isoenergetic when PtO⁻ is used (see Table 2.1). Spin-orbit effects are anticipated to stabilize the latter further due to its large influence in late-transition metals including Pt⁻.⁷⁵

Table 2.1. MN15/aug-cc-pVTZ^a relative energy (kcal/mol) and experimental yields (gas phase reactions at room temperature) in parenthesis of different products of the NiO⁺/PdO⁺/PtO⁺/PtO⁻ + CH₄ reaction^b. Detailed data can be found in S19 of reference¹¹ (attached to this dissertation).

Products	M = Ni⁺	M = Pd^{+(c)}	M = Pt⁺	M = Pt⁻
M + CH₃OH	17.7 (100 %)	15.1 (78 %)	36.9 (0 %)	0.1
MCH₂ +	39.8	22.3	0.0	0.0
H₂O	(0 %)	(0 %)	(98%)	
MOCH₂ +	0.0	0.0	9.3 ^d	33.8
H₂	(0 %)	(15 %)	(2 %)	

^a The aug-cc-pVTZ-PP basis set is used for Pt and Pd (see section 2.3).

^b Exact electronic energies are given in S19 of reference 11.

^c 7 % for Pd was unreactive and collected as a MO⁺(CH₄) complex.

^d Pt produced PtH₂⁺ + CH₂O.

Another worthwhile distinction is the energy requirement for the release of methanol from the metal center. Our MN15 calculations predict an energy difference between Pt⁺ + CH₃OH and the produced Pt⁺(CH₃OH) adduct is 60.3 kcal/mol and is higher than the upper limit of the range calculated theoretically (DFT/B3LYP) for first-row transition metals (31.0–56.8 kcal/mol).⁷⁶ The detachment energy of methanol from Pt⁻ is only 13.6 kcal/mol, more than four times less than that

from Pt^+ . The product (methanol) will be easily removed from the catalytic center in the presence of a polar solvent, such as water or methanol, enhancing the reaction's selectivity towards the synthesis of methanol. On the other hand, the C–H activation energy barrier for PtO^- is relatively high (39.6 kcal/mol), and certainly higher than the 9.4–34.4 kcal/mol range (DFT/B3LYP) for first-row transition metal oxide cations.⁷⁶

Overall, the selectivity of PtO^- is predicted to be higher than PtO^+ , but the activation of the C–H bond is less efficient. The wise choice of ligands is expected to reduce the activation barrier and maintain higher selectivity for the anionic catalytic center.

Concerning the heterogeneous catalytic applicability of anionic catalysts in the MTM pathway, we hypothesize that the anionic centers will have a shorter methanol residence time at the catalytic site, avoiding methanol overoxidation and facilitating methanol removal.⁷⁷ This is due to the weak charge-dipole interaction of the formed $[\text{M}^- \dots \text{HOCH}_3]$ compared to that of $[\text{M}^+ \dots \text{HOCH}_3]$. Additionally, we demonstrated previously¹¹ that the activation energy barriers for anionic centers in the oxidation step are negligibly small. Since anions are unstable and CH_4 , N_2O and CH_3OH have small or negative electron affinities, the return of the electron to the metal is certain in this situation. A significant focus must be placed on avoiding compounds with higher electron affinities for practical applications. Alternately, ligands that raise the metal center's electron affinity must be used.

2.6. Proposed reaction mechanism of MTM catalyzed by atomic M^-

Once the metal oxide is produced, methane activation and conversion are believed to proceed through three main steps: (a) The oxidation of the metal center by the nitrous oxide (N_2O) and subsequent formation of either metal oxide, this found to occur either in a single step or three

consecutive steps (b) Methane activation step which occurs either via a radical pathway or a proton-coupled electron transfer (PCET) or [2+2] producing either a hydroxylated metal center with a free methyl radical or a bound methyl. The former implies the homolytic dissociation of the CH bond and the latter a heterolytic one, and (c) Methanol product release to regenerate the catalyst. (Figure 2.3) shows a schematic representation of the overall catalytic reaction.

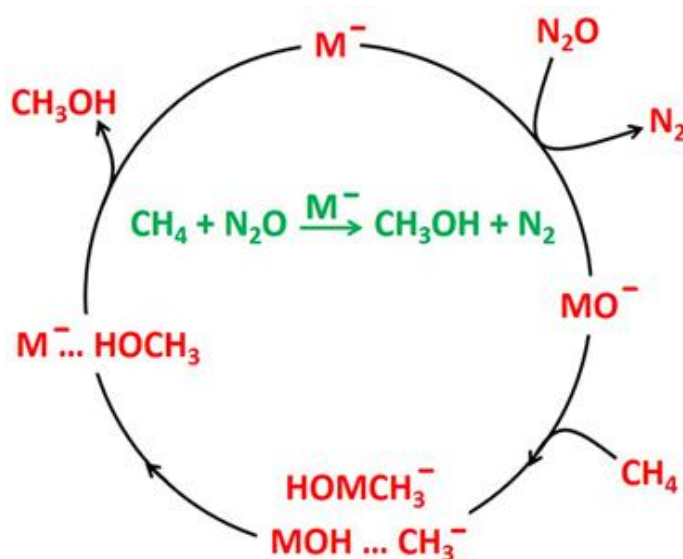


Figure 2.3 Catalytic cycle for the oxidation of CH₄ to CH₃OH by the anionic metal center (M⁻) using N₂O as an oxidant.

2.7. Results

2.7.1. DFT calculated reaction geometries and pathway for Pt⁻ oxidation

Metal oxidation can occur via two different mechanisms: a single-step mechanism via TS₂ and a multistep mechanism via TS1_a, IS1_a, TS1_b, IS1_b, and TS1_c. The oxygen atom can be transferred directly from N₂O to Pt⁻ using TS₂. Along the second path, N₂O binds to Pt⁻ with its nitrogen terminus first, then oxygen binds to Pt⁻, forming a PtNNO ring, and finally, N₂ is released (Figure 2.4). In agreement with our calculations¹¹, the ground states of both Pt⁻ and PtO⁻ (reactant

and product) have been identified experimentally as doublet states (2D and $^2\Pi$)⁷⁸⁻⁸⁰. Furthermore, our CASSCF calculations revealed that the ground state spin multiplicity and single-reference character (one unpaired electron) are preserved across the two mechanisms' structures. As a result, the RCCSD(T) numerical results should be considered quite accurate. Figure 2.4 part A shows detailed reaction steps.

Figure 2.5 illustrates the MN15 and CCSD(T) energy landscapes for the two mechanisms. The contributions of the ZPE (at MN15) and SO (at CASSCF) effects are also considered. All methods predict that the multi-step mechanism will be more advantageous. The oxidation of Pt is highly exothermic, according to the MN15 and CCSD(T) energetics, and the energy of the IS and TS structures for the multi-step is less than the energy of the reactants (Pt + N₂O). The transition state for the single-step mechanism (TS2) has at least 7.4 kcal/mol more energy than the reactants (MN15). TS1c has the largest energy difference of 3.5 kcal/mol between MN15 and CCSD(T). The relatively minor differences between CCSD(T) and MN15 support the use of the MN15 functional.

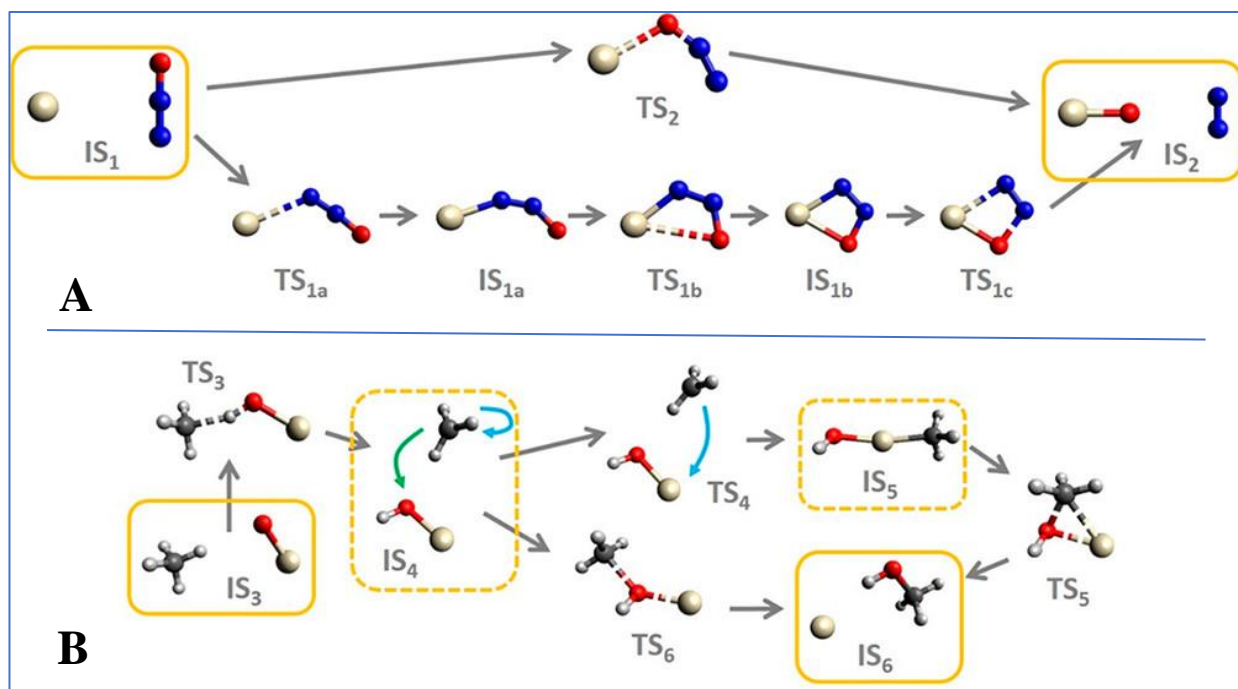


Figure 2.4. MN15 intermediate structures (IS) and transition states (TS) for the reaction's steps 1–3 with M = Pt. Part A corresponds to the two possible mechanisms for step 1 connecting IS₁ and IS₂. Part B relates to steps 2 and 3. Step 2 goes from IS₃ to either IS₄ or IS₅, and step 3 completes the cycle via TS₅ and TS₆ and forms IS₆.

Details on geometries including bond lengths and bond angles for all structures are shown in Figure S1 in appendix 1.

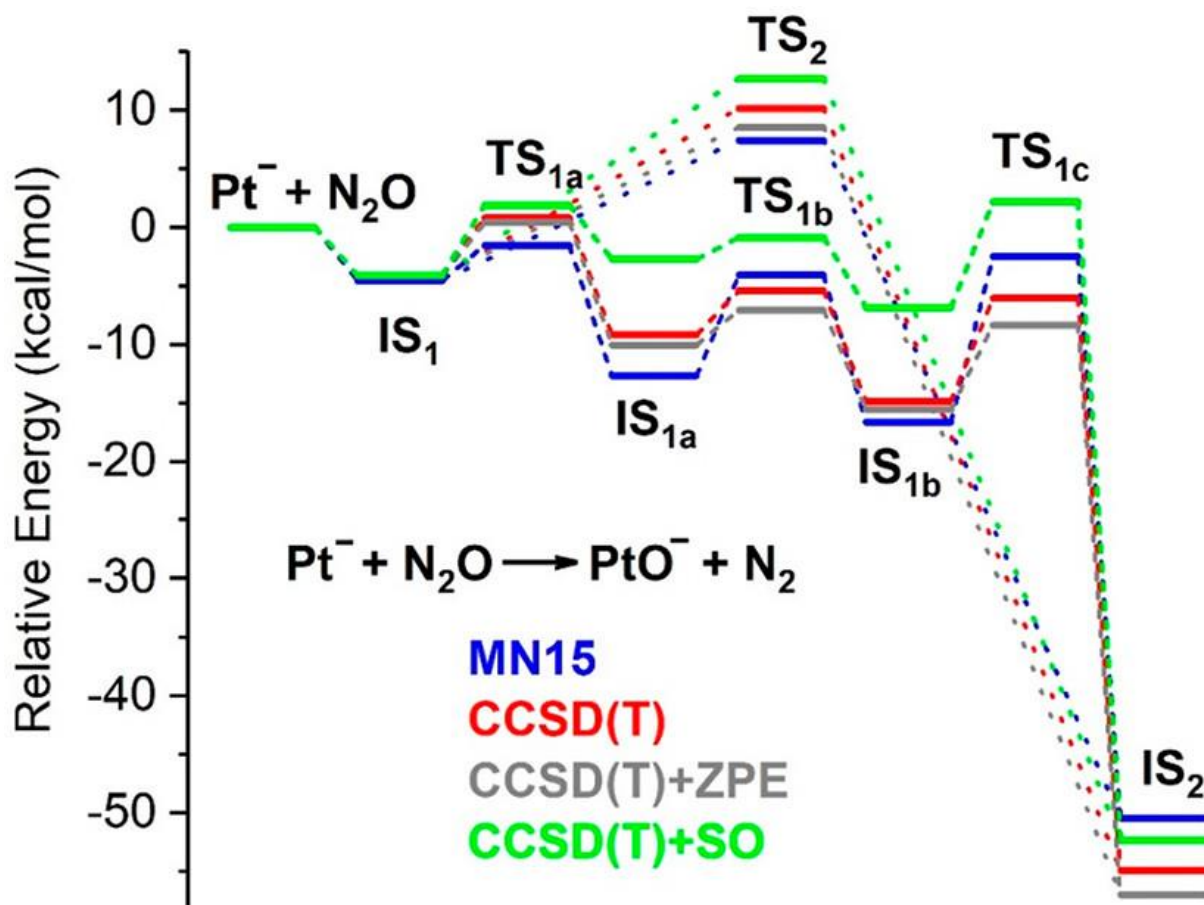


Figure 2.5. Energy diagram for the oxidation step of the metal center (see eq 1 of figure 2.11) for different methodologies: DFT/MN15 (blue lines), RCCSD(T) (red lines), ZPE-corrected RCCSD(T) (gray lines), spin-orbit-corrected RCCSD(T) (green lines). See Figure 2.4 for the notation of all IS and TS structures.

2.7.2. DFT and CCSD(T) Calculated reaction energy landscape for Pt⁻-mediated CH₄

oxidation

Once the metal oxide is generated (IS₂), it attracts a methane molecule to form IS₃. The PtO⁻ oxygen terminus extracts a hydrogen atom from methane using TS₃ (see Figure 2.4). The resulting [PtOH...CH₃]⁻ interacting complex (IS₄) is extremely unstable, and a slight rotation of the methyl radical (see the blue curved arrow at IS₄ in Figure 2.4) leads to the formation of the extremely stable [HOPtCH₃]⁻ (IS₅) via TS₄. IS₄ can also pass through TS₆ (methyl radical attacks oxygen; see the green arrow at IS₄ in Figure 2.4 part B) to produce [Pt...HOCH₃]⁻, which is also formed from IS₅ via TS₅. The energy diagram for the conversion of methane to methanol

(reactions (2) and (3)) is shown in Figure 2.6 For PtO^- , the doublet spin multiplicity is still in effect.

2.7.3. DFT and CCSD(T) Calculated energy landscape for PCET mechanism in $\text{Pt}^- + \text{CH}_4$ reaction.

The energy landscape for the reactions that transform methane into methanol is shown in Figure 2.6 For all intermediate and transition states, the Pt^- doublet spin state offers the lowest energy path for both computational methods. The energy barrier for hydrogen abstraction is around 40 kcal/mol. With a negligible activation barrier of 0.1 kcal/mol, the conversion of the generated IS_4 to IS_5 is nearly barrier-free (TS_4). The ultimate IS_6 structure, which is 25–30 kcal/mol more energetic, must overcome a barrier of 80 kcal/mol to develop since IS_5 is the global minimum of the energy landscape. As an alternative, IS_4 can pass through an activation energy barrier of only about 20 kcal/mol and then immediately reach IS_6 through TS_6 . It requires time for IS_6 to release methanol. The energy range due to the different methods is no more than 5.5 kcal/mol, including spin-orbit effects.

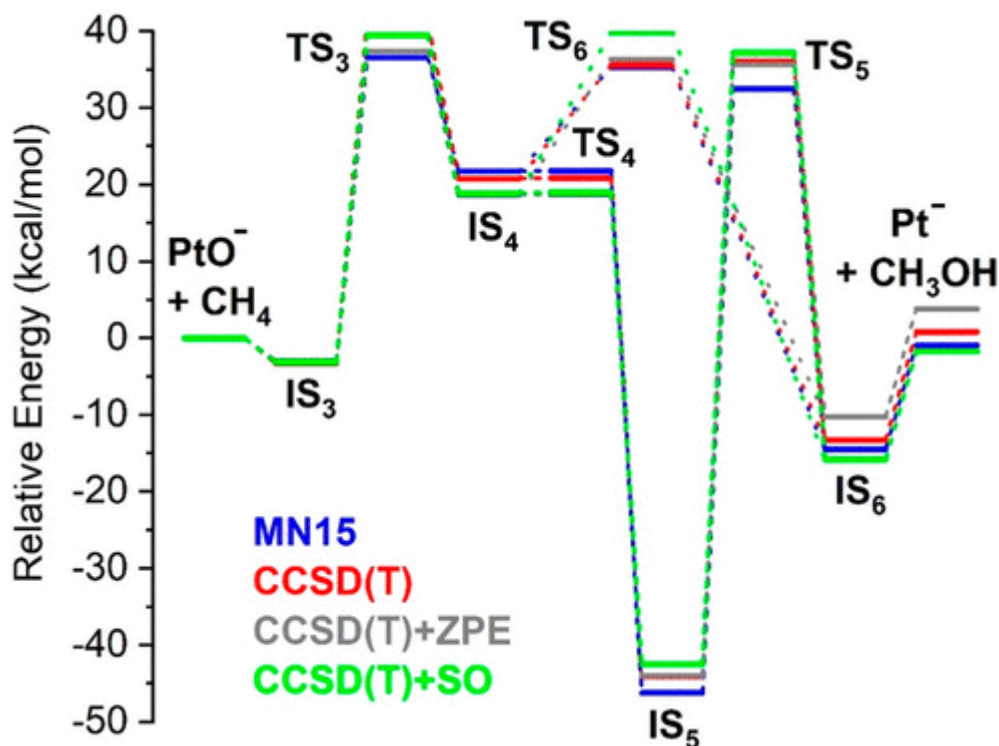


Figure 2.6. Energy diagram for the methane functionalization steps for different methodologies: DFT/MN15 (blue lines), RCCSD(T) (red lines), ZPE-corrected RCCSD(T) (gray lines), and spin-orbit-corrected RCCSD(T) (green lines). See Figure 2.4 for the notation of all IS and TS structures.

For the MO^- to be practically efficient, the C-H activation energy barrier should decrease by around 15 kcal/mol, and the production of IS_5 should be avoided. By using the right ligands, it is possible to get around both bottlenecks. As is the case for positively charged completely coordinated metal-oxide complexes, the space required for the creation of IS_5 can be constrained by finishing the metal's first coordination sphere.⁸¹

2.7.4. Pt^- -mediated methane activation via PCET orbital analysis

We used Natural Orbital analysis^{82, 83} to track the electronic density movement during the hydrogen atom abstraction process of methane activation. The PtO 's related molecular orbitals are depicted in Figure 2.7. One of the two π^*_{PtO} orbitals is the only orbital in the system that is singly occupied. The other orbital is doubly occupied, as are the two π_{PtO} orbitals. In addition, the valence

space of PtO^- contains the following doubly occupied orbitals: a PtO^- bonding molecular orbital, the $2s\text{O}$ orbital, two Pt orbitals, and one Pt orbital with the $4s\text{Pt}$ character (see reference ⁸⁴ for information on PdO 's equivalent orbitals). When CH_4 reacts with PtO^- , the closed-shell PtOH^- is produced along with a methyl radical. The singly occupied orbital of $[\text{CH}_3\dots\text{PtOH}]^-$ is shown in Figure 2.7. According to the orbitals of PtOH^- (see Figure 2.7), the hydrogen atom is bonded to PtO^- in the following manner: the π_{PtO^-} electrons "attack" H^+ (Lewis acid/base binding; see $\pi_{\text{PtO}^-}/\sigma_{\text{OH}}$ orbitals of Figure 2.7) and the unpaired electron of H atom couples with the unpaired electron in the π_{PtO^*} orbital (see $\pi_{\text{PtO}^*}/d_{\pi,\text{Pt}}$ orbitals of Figure 2.7), which shifts towards the Pt end. Overall, the process can be seen as a kind of proton-coupled electron transfer (PCET). To further support this observation, we plotted the CCSD(T)//MN15 activation energy barrier against the proton affinity (PA) for the three metal oxides (NiO^- , PdO^- , PtO^-) at their doublet spin electronic state as $\text{PA} = E[\text{MO}^-] + E[\text{H}^+] - E[\text{MOH}]$. We found that larger PA (381.4, 386.4, 352.8 kcal/mol) corresponds to smaller activation energy barriers (30.9, 21.7, 44.3 kcal/mol), which suggests that PA can be a good descriptor for future theoretical investigations.

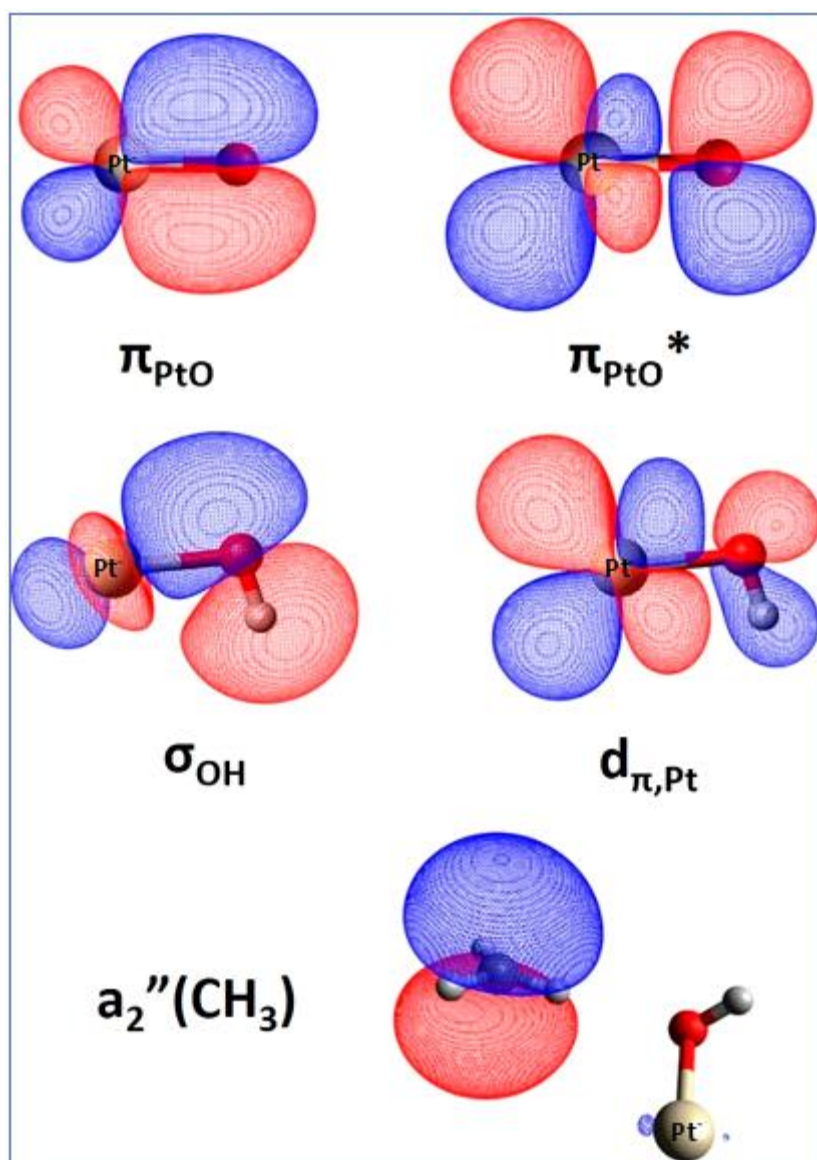


Figure 2.7. Molecular orbital contours of PtO^- (top), PtOH^- (middle), and $[\text{CH}_3 \dots \text{PtOH}]^-$ (bottom) involved in the C-H activation process.

2.7.5. DFT Calculated reaction energy landscape for Pd^- and Ni^- oxidation reactions.

To see the impact of the metal identity on oxidation efficiency, we studied Ni^- and Pd^- oxidation reactions with N_2O . Figure 2.8 shows the energy curves for the oxidation of the Ni^- centers with N_2O . We also add Pd^- in the same figure for comparison's sake. We also considered the path of the lowest quartet spin state for Ni^- and Pd^- . All three metal oxide anions have a doublet ground state, which has been experimentally identified as $^2\Pi$.⁷⁹ Our current calculations on PtO^-

and our recent computations on PdO^- confirm that these systems have a doublet ground state.⁸⁴ Given that the expected ground state of NiO^- is a $^4\Sigma^-$ at CCSD(T) but a $^2\Pi$ at MN15, we were led to explore the whole quartet reaction pathway for Ni^- . See figure 2.8 below:

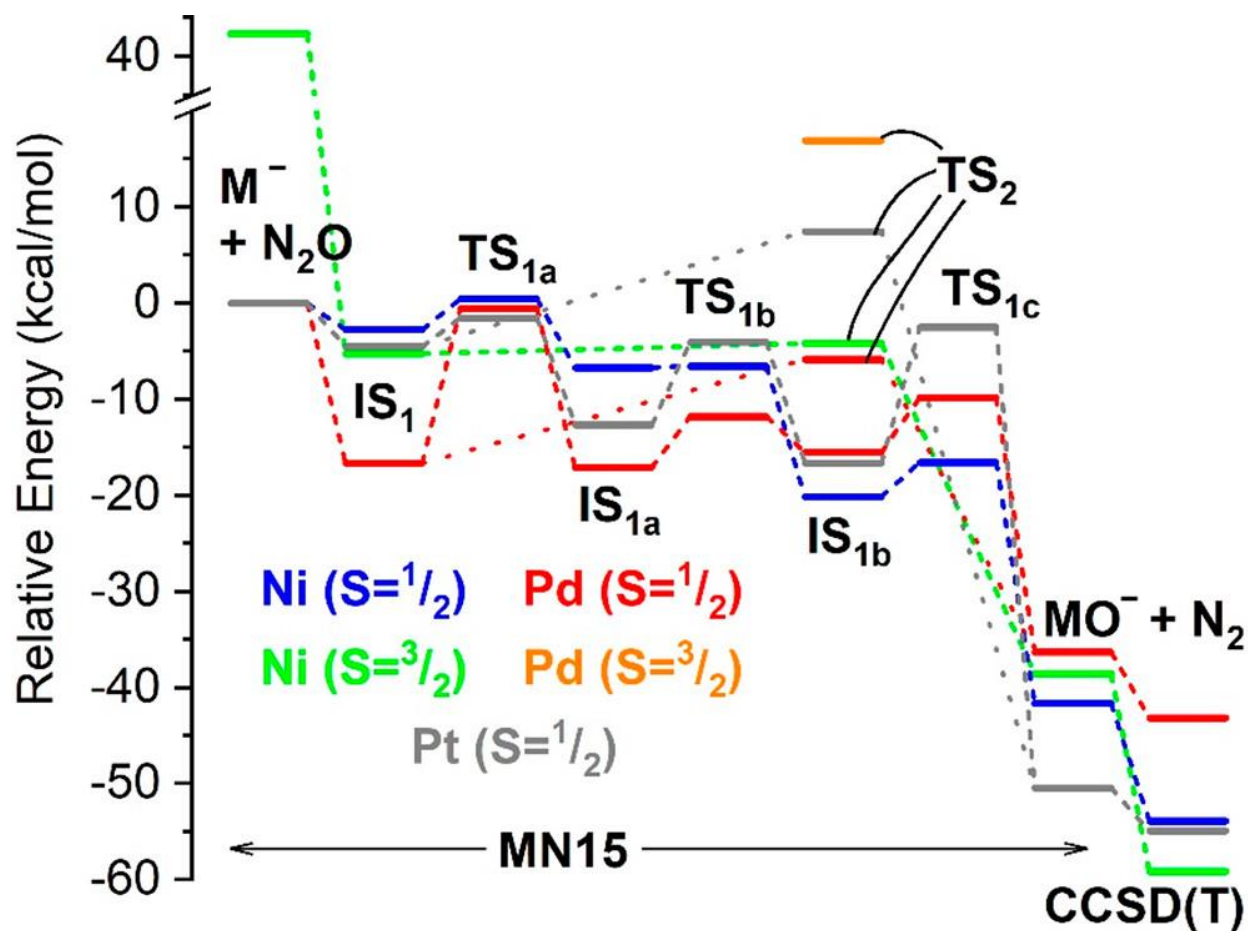


Figure 2.8. MN15 energy diagram for the oxidation of Ni^- , Pd^- , and Pt^- to NiO^- , PdO^- , and PtO^- by N_2O . Blue and green lines correspond to Ni with doublet and quartet spin multiplicity, respectively, red and purple to Pd with doublet and quartet spin, and grey to Pt (doublet spin). The CCSD(T) energies of the final products $\text{MO}^- + \text{N}_2$ ($M = \text{Ni}, \text{Pd}, \text{Pt}$) are also shown at the right end of the plot.

Not long ago, Sakellaris and Mavridis highlighted worries regarding the ground state of NiO^- in their earlier high-level theoretical work.⁸⁵ At the MRCI level, they discovered a $^4\Sigma^-$ ground state, but a $^2\Pi$ at CCSD(T). They expressed reservations about their CCSD(T) results because of

the rich multi-reference nature of $^2\Pi$ (their coefficient for the dominant configuration is just 0.44), and they advocated a $^4\Sigma^-$ ground state as a result. At the same level of theory, we repeated the calculations and observed less multi-reference character (the largest coefficient is 0.62 and the next one is -0.32). In addition, our CCSD(T) calculations point to a $^4\Sigma^-$ ground state in harmony with the MRCI calculations of Sakellaris and Mavridis, but in disagreement with their CCSD(T) results. Our CCSD(T)/aug-cc-pV5Z energy for the $^2\Pi$ is in absolute agreement with their energy (-1582.44192 a.u.), but our CCSD(T)/aug-cc-pV5Z energy for $^4\Sigma^-$ is 10^{-2} a.u. lower than theirs (-1582.44321 vs. -1582.43324 a.u.). A similar difference is found at the C-CCSD(T) level, where the $3s^23p^6$ electrons of Ni are also correlated (-1582.92327 vs. -1582.91407 a.u.). We believe that the CCSD(T) energies of Sakellaris and Mavridis correspond to a higher energy $^4\Sigma^-$ state and that the ground state of NiO^- is $^4\Sigma^-$, as indicated by the previous MRCI and present CCSD(T) calculations.

Considering both multiplicities in Ni, we show that the excited state of Ni could permit an extra oxidation pathway facilitated by the excited state of $\text{Ni}^- (^4G; 4s^23d^84p^1)$. This Ni state is above the ground state, but the NiON_2 complex with $S=3/2$ is lower than $S=1/2$ and interacts nearly without a barrier to create $\text{NiO}^- (^4\Sigma^-)$, which is an excited state at MN15 but the ground state at CCSD(T); see Figure 2.8. The $S=3/2$ pathway's response mechanism is a one-step process that passes through TS2 in the previous figure. The reaction mechanism for the $S=3/2$ pathway is a one-step mechanism running through TS2 (figure 2.8). The $\text{Ni}^- + \text{N}_2\text{O}$ reaction (following the three-step mechanism of Figure 2.8) bears minimal activation barriers of less than 5 kcal/mol along the $S=1/2$ as well. The activation energy barrier for the $S=3/2$ pathway for Pd^- is high, and we were unable to identify this transition state for Pt. Therefore, the $S=1/2$ potential energy hypersurface is followed by Pt^- and Pd^- . However, because TS2 has less energy than TS1a, Pd^- (as opposed to Pt^-)

prefers the one-step process for $S=1/2$ (see Figures 2.8 and 2.4 part A). The activation energy barrier for Pd^- is 10.7 kcal/mol (TS1c-IS1 energy difference). Finally, it can be said that the oxidation of any of the three metal anions is quite simple (regardless of the mechanism), has low activation barriers, and is quite exothermic. The order is decreasing as follows: $\text{Pt}^-/\text{Pd}^-/\text{Ni}^-$.

Figure 2.9 shows the energy landscape for the $\text{MO}^- + \text{CH}_4$ reaction ($M = \text{Ni}, \text{Pd}, \text{and Pt}$). To precisely represent the energy of the doublet and quartet states of NiO^- , we employed CCSD(T)/MN15 energies. For Ni and Pd, the TS₄ structure linking IS₄ and IS₅ was not found. According to the Pt findings, we think that IS₄ is almost a shoulder in the potential energy surface and that IS₄ "slides" to IS₅ with a small slope (nearly non-existent energy barrier). TS₄ is not represented in 2.9 as a result. In contrast to Ni, whose journey begins with $\text{NiO}^- + \text{CH}_4$ ($S=3/2$) and ends with $\text{Ni}^- + \text{CH}_3\text{OH}$ ($S=1/2$), Pd^- and Pt^- are always in their doublet spin state. Both spin multiplicities are included in figure 2.9 for both mechanisms of Figure 2.6 (radical and 2+2).

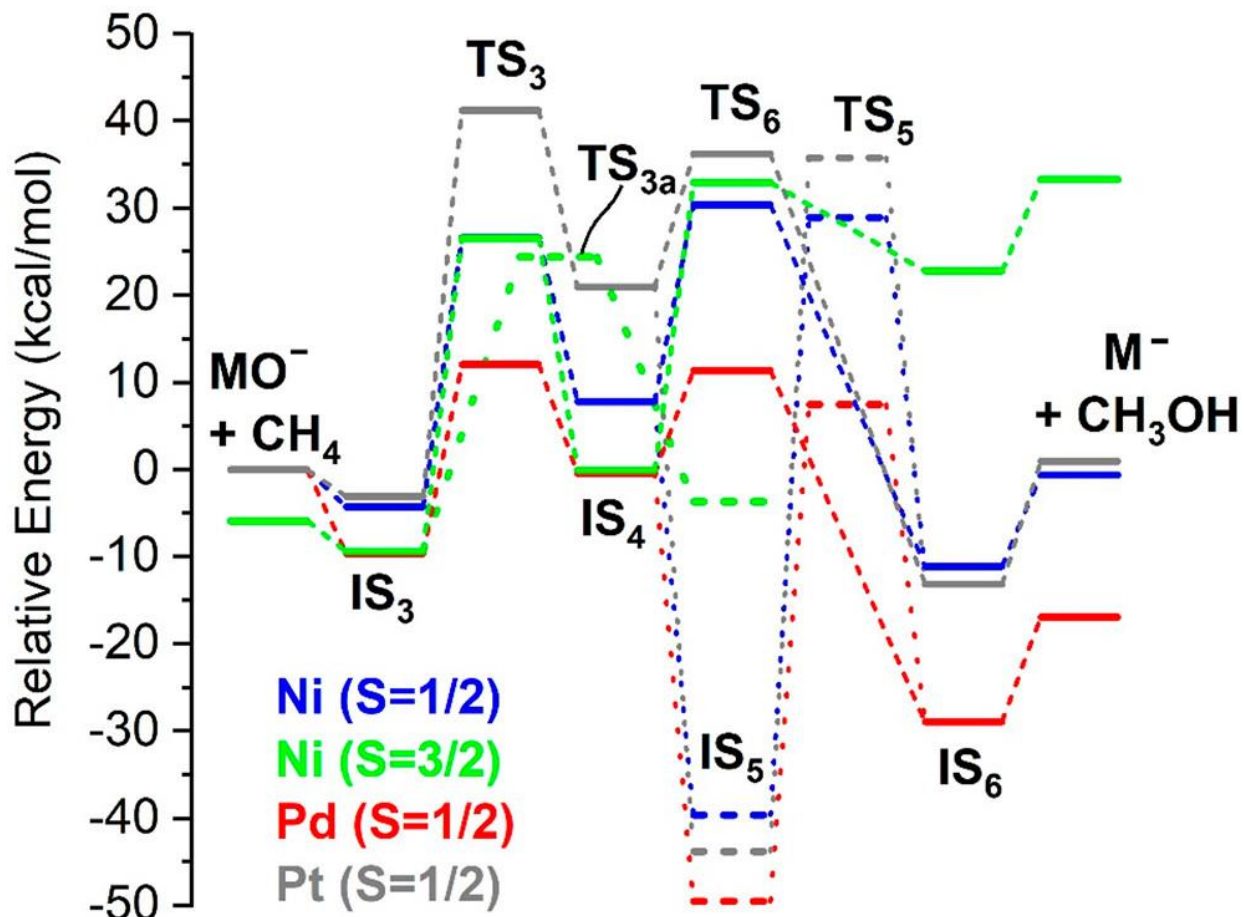


Figure 2.9. RCCSD(T)/MN15 energy diagram for the $\text{MO}^- + \text{CH}_4 \rightarrow \text{M}^- + \text{CH}_3\text{OH}$ reaction ($\text{M} = \text{Ni}, \text{Pd}, \text{Pt}$). Solid lines correspond to the hydrogen abstraction mechanism and dashed horizontal lines the 2+2 mechanism. Blue/green colors correspond to the doublet/quartet paths of Ni, and red/grey to the doublet paths of Pd/Pt.

Only for Pd, the $\text{MO}^- + \text{CH}_4$ reaction is exothermic. For Pt and Ni, the energy of the products is within 1 kcal/mol of the energy of the reactants. In fact, the $\text{MO}^- + \text{CH}_4$ component can be driven by the exothermic nature of the overall $\text{N}_2\text{O} + \text{CH}_4 \rightarrow \text{N}_2 + \text{CH}_3\text{OH}$ process. The energy activation barriers in Pd^- are the smallest, whereas those in Pt^- are the largest. The activation energy barriers for Pd^- are 22 and 12 kcal/mol, indicating a feasible pathway, in contrast to the twice as large barriers for Pt and Ni (solid red lines in figure 2.9). The 2+2 mechanism's CH_3MOH intermediate is the multi-dimension energy surface's global minimum and is extremely stable with respect to the final products by at least 33 kcal/mol (in the Pd^- case). As a result, as will be shown

later in this work, the addition of ligands is required to restrict the available coordination space and remove it.

As observed in Figure 2.9, Ni^- has a competitive quartet spin channel that, while having a lower energy at the beginning of the $\text{MO}^- + \text{CH}_4$ reaction, abandons its position to the doublet for both mechanisms to ultimately release a doublet M^- . For the radical mechanism, the transition occurs between IS_4 and TS_6 , while for the 2+2 pathway, it occurs between TS_{3a} and IS_5 . The transition state (TS_{3a}) directly connects $\text{MO}^- + \text{CH}_4$ and $[\text{CH}_3\text{MOH}]^-$ (see S3 of reference¹¹ attached to this dissertation).

In conclusion, Pd^- has the lowest electron affinity yet offers the most promising energy diagram. Greater electron affinity can further guarantee that the metal will receive its negative charge back at the conclusion of the catalytic cycle. Therefore, the removal of IS_5 and an increase in the catalyst's electron affinity should be the goals of the addition of ligands. Also worth noting is that the energy required to liberate the methanol from the metal anion is in the 10–14 kcal/mol range and is essentially unaffected by the metal identity.

2.7.6. Alternative MTM reaction pathway for Pt^-

We found more possible MTM channels. Up until now, we thought that the activation of the C-H bond, which is caused by the terminal oxygen atom, came after the oxidation phase (gray energy diagram in Figure 2.10). Other pathways found involve either initial or post-oxidation activation of the C-H bond by the metal center (rather than the oxygen terminal). Figure 2.10 shows the energy plot for these pathways together with the SI values for the corresponding structures, energies, and frequencies.

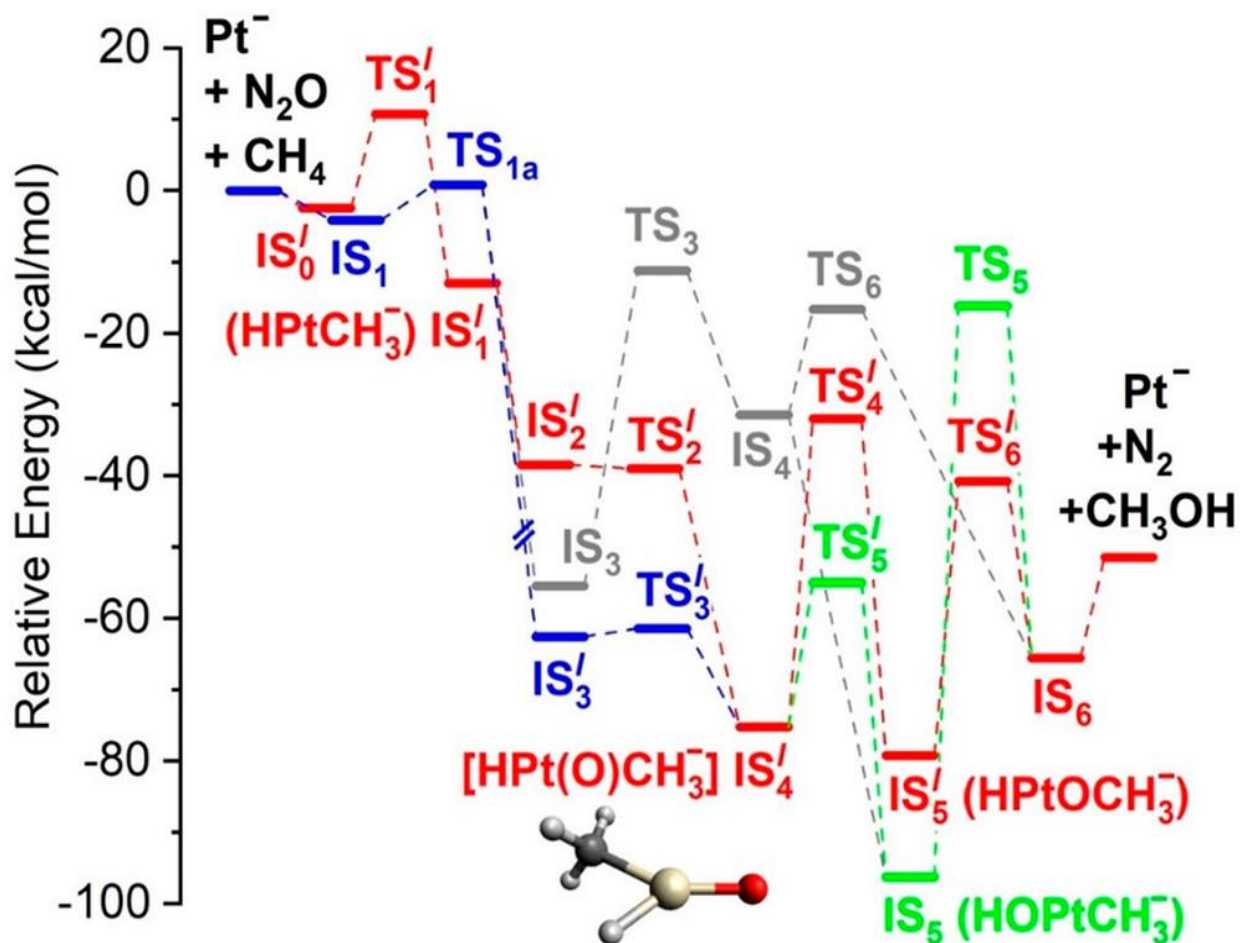


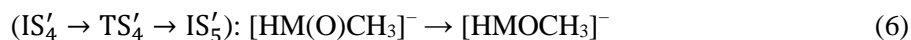
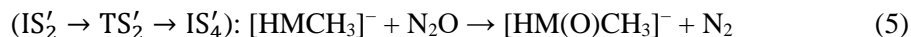
Figure 2.10. RCCSD(T)/MN15 energy diagrams for several pathways of the $\text{Pt}^- + \text{CH}_4 + \text{N}_2\text{O} \rightarrow \text{Pt}^- + \text{CH}_3\text{OH} + \text{N}_2$ reaction.

Specifically, the red path pertains to the activation of the C-H bond first by Pt^- , followed by the oxidation of the metal center forming $\text{HM}(\text{O})\text{CH}_3^-$, where all three active units (H, CH_3 , O) are attached to the metal (see inset for IS'_4 of Figure 2.11). The re-combination of these fragments to form methanol has two alternatives with either CH_3 (red path) or H (green path) migrating first to oxygen. The blue path runs through IS'_4 , but the C-H bond splits after the oxidation of the metal center ($\text{IS}'_3 \rightarrow \text{TS}'_3$). The reaction network of Figure 2.10 for a metal M (here $\text{M} = \text{Pt}^-$) is summarized by the ensuing chemical equations (gray path corresponds to equations (1) + (2) + (3)):

Grey path



Red path



Blue path



Green path



Figure 2.11. alternative reaction pathways for CH₄ activation

Regardless of the approach taken, (4) + (5) or (8) + (9), the second step to produce IS₄' is almost barrier-free; see TS₂' and TS₃'. Observe that at CCSD(T)/MN15 (Figure 2.10), the energy of TS₂' is lower than that of the equivalent reactants (IS₂'), however at the MN15 level, where completely optimized structures are utilized, it is higher. Another finding is that in reactions (4) and TS₁', the energy barrier for activating the C-H bond from the metal is just 12.3 kcal/mol, in contrast to 44.3 kcal/mol when oxygen is involved (2). For reactions (2) and (4), the activation

barriers are 21.7 and 30.8 kcal/mol and 15.3 and 33.0 kcal/mol for Pd and Ni, respectively. These figures indicate that Pd can activate the C-H easier from either site (metal or oxygen).

For practical applications, the metal must first be oxidized before CH₄ is introduced to the metal center. This prevents the catalytic center from being blocked from receiving oxygen. Metal anions are preferable to neutral and cationic metal centers because reaction (4) necessitates a certain activation energy barrier. For instance, experimental and theoretical studies on the interactions of Pt and Pt⁺ with CH₄ revealed that Pt undergoes a barrier-free transition to the HPtCH₃ path,⁸⁶ while Pt⁺ encounters a low barrier of 2.5 kcal/mol.⁸⁷

The reaction barriers to produce coordinated OCH₃ or OH in [HMOCH₃]⁻ and [HOMCH₃]⁻ after IS 4' is generated, are 20.3 and 43.2 kcal/mol respectively (see figures 2.10 and 2.11), while the reaction barriers for the final attachment of CH₃ or H to make methanol are 80.1 and 38.5 kcal/mol (reactions (6) + (7) or (10) + (11)). From the (1)-(3) gray path, both have activation barriers that are overall greater (44.3 and 14.8 kcal/mol). However, the catalyst may get contaminated by the rapid production of IS 4' and IS 5. When ligands are coordinated, this impact will be abolished. We carried out a chemical kinetics analysis with the aid of the COPASI software⁸⁸ to support upcoming gas-phase experiments on the Pt⁻ + N₂O + CH₄ reaction. The pre-exponential factor, which is computed as kT/h (k = Boltzmann's constant; h = Planck's constant; T = temperature in K), was used to estimate the reaction rates using the Arrhenius equation. Various temperature values were used. (See S9 in reference 103 and table 2.3.

Finally, we explored the iron catalytic pathway, which is the most common transition metal element. We chose iron for other reasons as well. Given that the Ni, Pd, and Pt metals with the lowest E_{ea} values perform the best and that there may be a relationship between E_{ea} and catalytic performance, iron can be considered an even stronger possibility due to its low E_{ea} value. Iron

calculations proved to be extremely difficult, necessitating the adoption of a composite approach that combines MRCI and CCSD(T) (qCCSD(T); see Section 2.3). It takes vast basis sets and highly correlated techniques to calculate the E_{ea} for a single iron atom accurately. The experimental E_{ea} for iron is (0.151 ± 0.003) eV.⁸⁹ While CCSD(T)/aug-cc-pVTZ forecasts an unstable anion ($E_{ea} = -0.07$ eV), our MN15/aug-cc-pVTZ value greatly overestimates the E_{ea} (0.76 eV). The value of 0.05 eV, which is still one-third of the experimental value, is more plausible when the basis set is increased to aug-cc-pV5Z CCSD(T).

On the other hand, it is simple to obtain the E_{ea} of FeO. The experimental value of 1.494 0.010 eV is in remarkable agreement with the CCSD(T)/aug-cc-pVTZ and MN15/aug-cc-pVTZ values of 1.469 and 1.467 eV, respectively.^{40, 90, 91} In the past, a great deal of research has been done on the electronic structure of FeO.⁹² At MRCI, there are three contending states (${}^6\Sigma^+$, ${}^6\Delta$, and ${}^4\Delta$), and their arrangement is dependent on relativistic effects, sub-valence electron correlation, and treatment with electron correlation. MN15 predicts a ${}^4\Delta$ ground state X with the first sextet state (${}^6\Sigma^+$) being 0.15 eV higher, while experimentally the ground state is $X^4\Delta_{7/2}$. However, CCSD(T)/aug-cc-pVTZ forecasts an entirely different order; the initial quartet state (${}^4\Delta$) is 0.15 eV higher than the ground state, which is a ${}^6\Sigma^+$. When aug-cc-pV5Z is employed, this difference is reduced to 0.07 eV. The ${}^6\Delta$ is located between them at the CCSD(T)/aug-cc-pVTZ and CCSD(T)/aug-cc-pV5Z levels of theory, or 0.08 eV and 0.02 eV, respectively. Given that the interaction of FeO^- with methane brings these three states even closer together, the issue gets much more complicated. To provide fair comparisons, we now choose to employ the same methods (MN15 and CCSD(T)/MN15 with an expanded triple-basis set) as in the Ni, Pd, and Pt species. Our findings do not accurately compare the relative energies of the sextet and quartet spin routes since they are often practically degenerate.

For the high spin case ($S=5/2$), there is some agreement between the MN15 and CCSD(T)/MN15 values; however, for the quartet spin multiplicity ($S=3/2$), there is a significant difference. The quartet-sextet (${}^4F; 4s^23d^7/{}^6F; 4s^23d^64p^1$) energy splitting for Fe between MN15 and CCSD is different, and the MN15 energy diagram for $S=5/2$ is parallel (within 7 kcal/mol) to the CCSD(T)/MN15 one but separated by roughly 0.7 eV. The S1 in reference¹¹ (attached to this dissertation), contains comprehensive energy diagrams for both spins and all procedures. The $S=3/2$ MN15 and CCSD(T) energy landscapes, on the other hand, are more similar, though their structural differences are roughly 20 kcal/mol. $[\text{FeOH}\dots\text{CH}_3]^-$ is one such structure, where the $S=3/2$ is a result of anti-ferromagnetic coupling between the $S=2$ state of $[\text{FeOH}]^-$ and the ${}^2A_2''$ state of CH_3 . The spin contamination is dramatic (larger than 1.0) and suggests the use of multi-reference approaches in this case. To combine the size-extensivity benefit of CCSD(T) and the proper description of the quartet state at the MRCI, we used the qCCSD(T) approach described in eq. 2.1 of Section 2.3. The CCSD(T)//MN15 energies are used for the sextet path and the qCCSD(T)//MN15 energies for the quartet path for all structures.

The reaction energies for steps (1) through (3) with $M = \text{Fe}^-$ are shown in Figure 2.12. In this instance, for both the low and high spin instances, we were able to pinpoint transition states for the radical (hydrogen abstraction; TS_3) and 2+2 (proton abstraction; TS_{3a}) processes. Insets in Figure 2.12 depict these structures for the sextet state. An initial comparison with Figures 2.8 and 2.9 shows that the metal center's oxidation is still simple and exothermic. Future research can therefore concentrate on the metal oxide and methane process. Another finding is that, in contrast to Ni^- , Pt^- , or Pd^- , which are either thermoneutral or exothermic, the $\text{FeO}^- + \text{CH}_4$ reaction is significantly endothermic. This is a result of the stronger iron-oxygen bond in FeO^- , therefore the

metal-oxygen binding energy can be used as an initial criterion for screening efficient catalysts, and it should not be larger than 50 kcal/mol.

2.7.7. CCSD(T)/MN15 Calculated reaction energy landscape for Fe^- (S = 3/2 and 5/2)

oxidation reactions

Nearly parallel routes for the quartet and sextet overlap at various points (figure 2.12). The early activation of the C-H bond is the most obvious distinction. Lower energy barriers are clearly provided by the sextet spin multiplicity, particularly for the [2+2] mechanism. Specifically, TS_{3a} leads to the global IS_5 (CH_3FeOH) minimum and is just 16.7 kcal/mol above $\text{FeO}^- + \text{CH}_4$. It is interesting that the radical method demands more energy and needs 29.7 kcal/mol to activate the C-H bond. The radical mechanism's energy barrier for the recombination of OH and CH_3 is 28.3 kcal/mol, while the [2+2] mechanism's activation barrier is 79.6 kcal/mol, making it impossible. Fe^- is generally not an efficient MTM conversion mediator. Additionally, the $\text{Fe}^- + \text{CH}_4$ reaction must overcome 44.4 (S=3/2) and 32.0 (S=5/2) kcal/mol barriers.

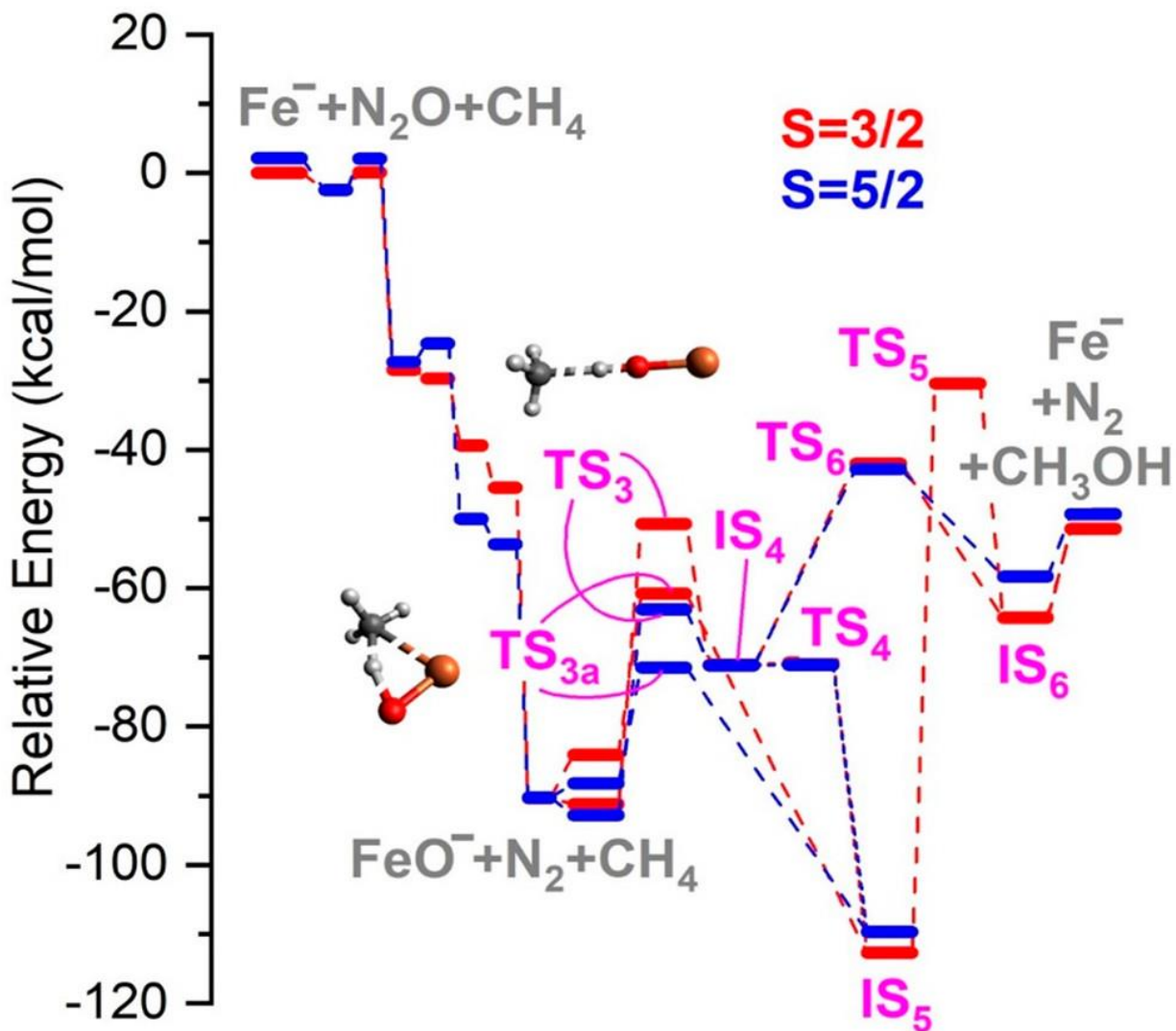


Figure 2.12. RCCSD(T)/MN15 ($S=5/2$) and qCCSD(T)/MN15 ($S=3/2$) energy diagrams for the radical and 2+2 mechanisms of the $\text{Fe}^- + \text{CH}_4 + \text{N}_2\text{O} \rightarrow \text{Fe}^- + \text{CH}_3\text{OH} + \text{N}_2$ reaction.

2.8. Conclusion and outlook

A fundamental, high-level computational investigation of the transition metal anion-mediated conversion of methane to methanol is presented in this work. An advantage of anionic metal centers is that they have little interaction with the methanol that is produced. This means that methanol can stay close to the catalytic center for shorter periods and there is less chance that it will be overoxidized. This observation is in line with the idea that methanol should be quickly

removed from the catalytic center as stated in the literature. Metal anions have the advantage of creating an activation barrier in their direct reaction with CH₄, preventing the formation of stable CH₃MH, which could potentially harm the catalyst. While this work paves the way for future research, a more in-depth search is required to locate effective catalysts that can be used in everyday life.

Methanol has a low interaction energy (10-15 kcal/mol) with the negative-charged metal center that is practically unaffected by the metal's nature. Although there is no direct correlation between the metal's E_{ea} and the catalytic cycle's energetics, a high E_{ea} value will ensure that the electron returns to the metal's center at the conclusion of each cycle. The C-H activation and CH₃-OH recombination barriers should be the primary focus of future research, according to our findings. The metal-oxygen binding energy should be used as an indicator, and it should be less than 50 kcal/mol. Locating ligands that promote the radical mechanism while maintaining the metal's negative charge and preventing the formation of CH₃MOH units is necessary for actual applications. In contrast to claims in the literature that the radical mechanism must be avoided for increased selectivity, it appears that this is less important in anionic systems if methanol is quickly picked up and removed by the solvent because of the weak metal-methanol attraction. Finally, we saw a correlation between the activation barrier and the metal oxide's proton affinity when we presented the radical C-H activation mechanism as a sort of PCET.

The lowest and highest E_{ea} metals (Fe and Pt) presented the largest activation energy barriers among the four metals used (group 10 metals and iron), and the best performance was found for Pd. Since the calculations for Fe proved to be quite demanding, we devised a new method. At the high-level and size-extensive CCSD(T) level, an electronic state with a single

reference wavefunction—not necessarily the ground state—is identified and studied. For the rest of the electronic states, the MRCI calculations use this CCSD(T) energy as the reference energy.

Future gas-phase experiments that are comparable to those conducted on cationic species can benefit from our findings. More metal centers will be screened, and the right ligands will be found in the next section.

We did not observe any direct relationships between E_{ea} and activation barriers or other energy variables. Pd^- , one of the metals being researched now, had the lowest energy barriers, and its oxide-form-mediated reaction was the only one that was obviously exothermic. The lowest and highest E_{ea} atoms, Fe and Pt, were discovered to rest at the opposite extreme. This was particularly true for Fe^- , which has a substantial activation barrier and an endothermic $[\text{FeO}]^- + \text{CH}_4$ route. The characteristic shared by all metals is that the release of methanol requires just 10 to 15 kcal/mol and is essentially independent of the metal.

2.9. Impact of ligand addition on catalytic MTM reaction pathway

2.9.1. Background on ligands in organometallic chemistry

The development of ligands in metal catalysts has been a common practice due to its substantial impact on the stability and reactivity of the metal complexes, especially in the primary coordination sphere. Most of the TMs studied so far are either neutral or cationic, their corresponding ligands have been formally classified either as Lewis acids or Lewis bases based on the way they share their electrons with the metal. Broadly speaking, ligands are classified into four main classes: (1) A neutral electron pair donor (L: type) such as pyridines and phosphines, (2) An anionic electron pair donor (X: type) such as halides and alkoxides, (3) Electron pair acceptor (Lewis's acid or Z: type) which typically include Lewis acidic elements (B, Al, Ga, In,

Si, Sn, Sb, etc.), (4) Hydrocarbyl ligand (R: type) such as methyl, phenyl or for substitution for an organic molecule.⁹³ Metals can make a sigma (σ) bond through an overlapping interaction of orbitals lobes pointing at one another (figure 2.13) or they make a Pi (π) bond with an unsaturated compound.

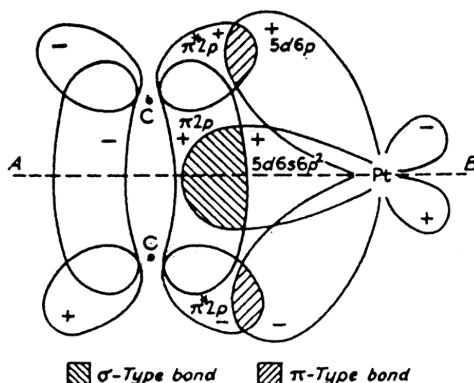


Figure 2.13. Ethylene-Platinum orbitals overlap showing competing π and σ bonds. "Reprinted (adapted) with permission from [Organometallics 2001, 20, 1, 2–6]. Copyright [2001] American Chemical Society".

For the isolated (non-ligated TM) the 5d orbitals are degenerate. The ligand introduction to the metal sphere can impact the metal binding capability through lifting of d-orbitals degeneracy. In the case of octahedral (O_h) geometry, both $d_{x^2-y^2}$ and d_{z^2} will be destabilized much higher than those d orbitals located in between axes (d_{yz} , d_{xz} , d_{xy}). Interestingly, several publications reported a change from oxo to oxyl behavior for late TMs oxides depending on the ligand used⁷⁰. There are two ligands studied in this work for MTM reaction: 4 methyl groups and biphenyl ligands (Bp). Both of which exist in a see-saw coordination geometry with the metal as can be seen in figure 2.14.

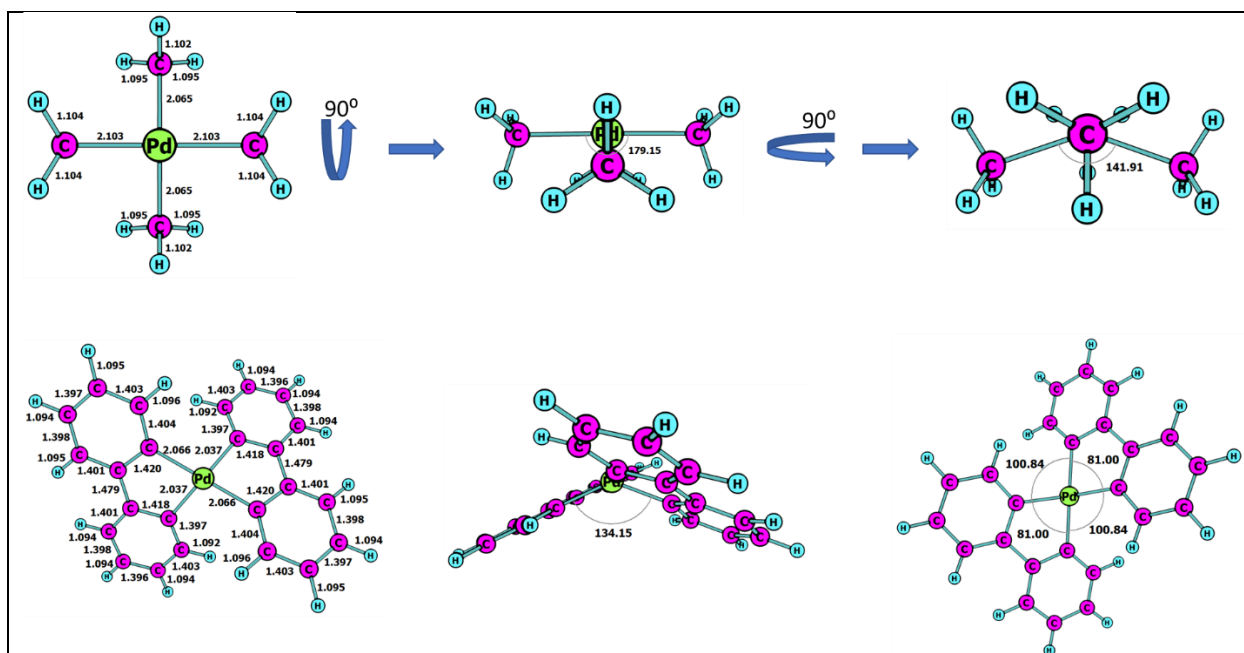


Figure 2.14. Optimized geometries of Structures of $[\text{Pd}(\text{CH}_3)_4]^-$ (top) and $[\text{Pd}(\text{Bp})_2]^-$ (bottom) catalysts used in the MTM pathway. Both structures are calculated at MN15/stable=opt/MN15/aug-cc-pVTZ level of theory. Bond lengths and angles are in angstrom and degree, respectively.

2.9.2. Computational details

All structures were optimized with the DFT method using the MN15 functional.⁹⁴ The aug-cc-pVTZ basis set (TZ) is used for H, C, N, O, Ni, and aug-cc-pVTZ-PP for Pd, Pt.⁹⁵⁻¹⁰¹ All intermediate structures are confirmed to be minima in their potential energy surface (real frequencies) and all transition states have one imaginary frequency (see S5 of reference¹⁰² attached to this dissertation). Single point energy calculations are performed at the Coupled Cluster Singles Doubles and perturbative Triples, CCSD(T),^{17, 62} with aug-cc-pVDZ (DZ) basis sets. The unrestricted version for both DFT and CCSD(T) calculations is employed as implemented in Gaussian 16.²⁶ Finally, CCSD(T)/TZ energies are estimated as $E[\text{CCSD(T)/TZ}] = E[\text{CCSD(T)/DZ}] + E[\text{MN15/TZ}] - E[\text{MN15/DZ}]$.

2.9.3. Results and discussions

2.9.3.1. $[\text{Pd}(\text{CH}_3)_4]^-$ -catalyzed MTM pathway/PCET reaction channel under ligand

influence

In figure 2.15 (top), the reactants, transition states, and products for the PCET pathway are labeled TS1R, I1, and TS1P, respectively. The mechanism is similar to the one reported previously for the free Pd^- where methane dissociates in a heterolytic manner and involves a concerted movement of methane proton and an electron to oxygen and metal center, respectively. The TS2R, I2, TS2P and P, correspond to the [2+2] pathway which also occurs similarly to the free Pd^- . They are shown in the middle part of the figure. The methanol release and catalyst and subsequent oxidation pathway are represented by P, TSOR, TSO, and TSOP in the bottom part of figure 2.15.

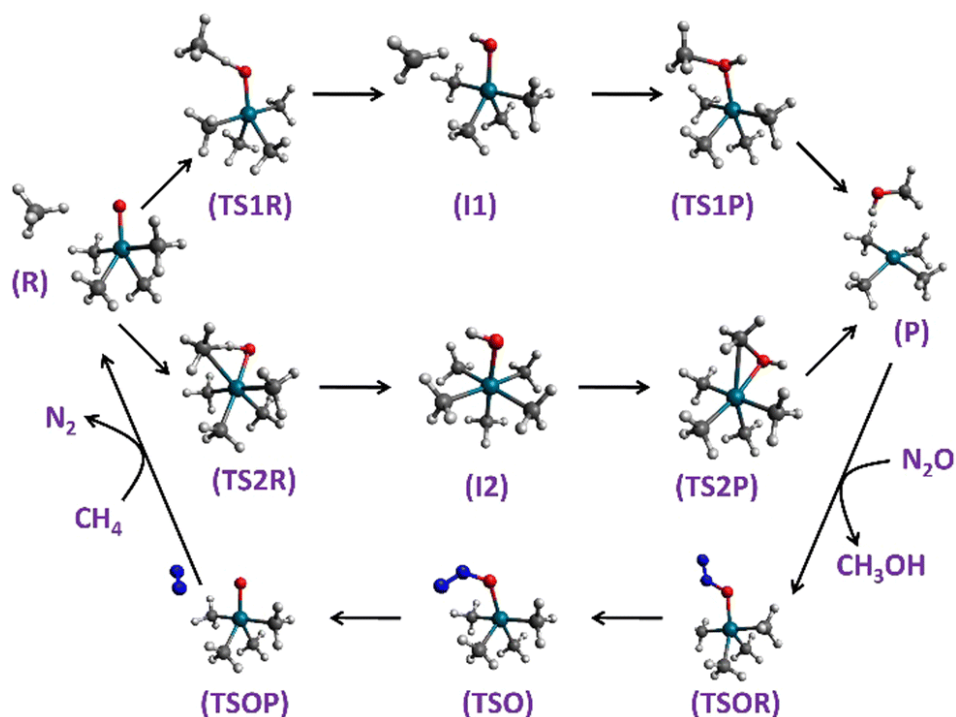


Figure 2.15. Structures of all intermediates and transition states for the $\text{CH}_4 + \text{N}_2\text{O} \rightarrow \text{CH}_3\text{OH} + \text{N}_2$ reaction facilitated by $[\text{PdO}(\text{CH}_3)_4]^-$. The PCET/[2+2] mechanisms are shown in the top/middle lines, while the bottom line corresponds to the oxidation step.

The overall energy diagram for PCET and [2+2] channels is demonstrated in figure 2.16.

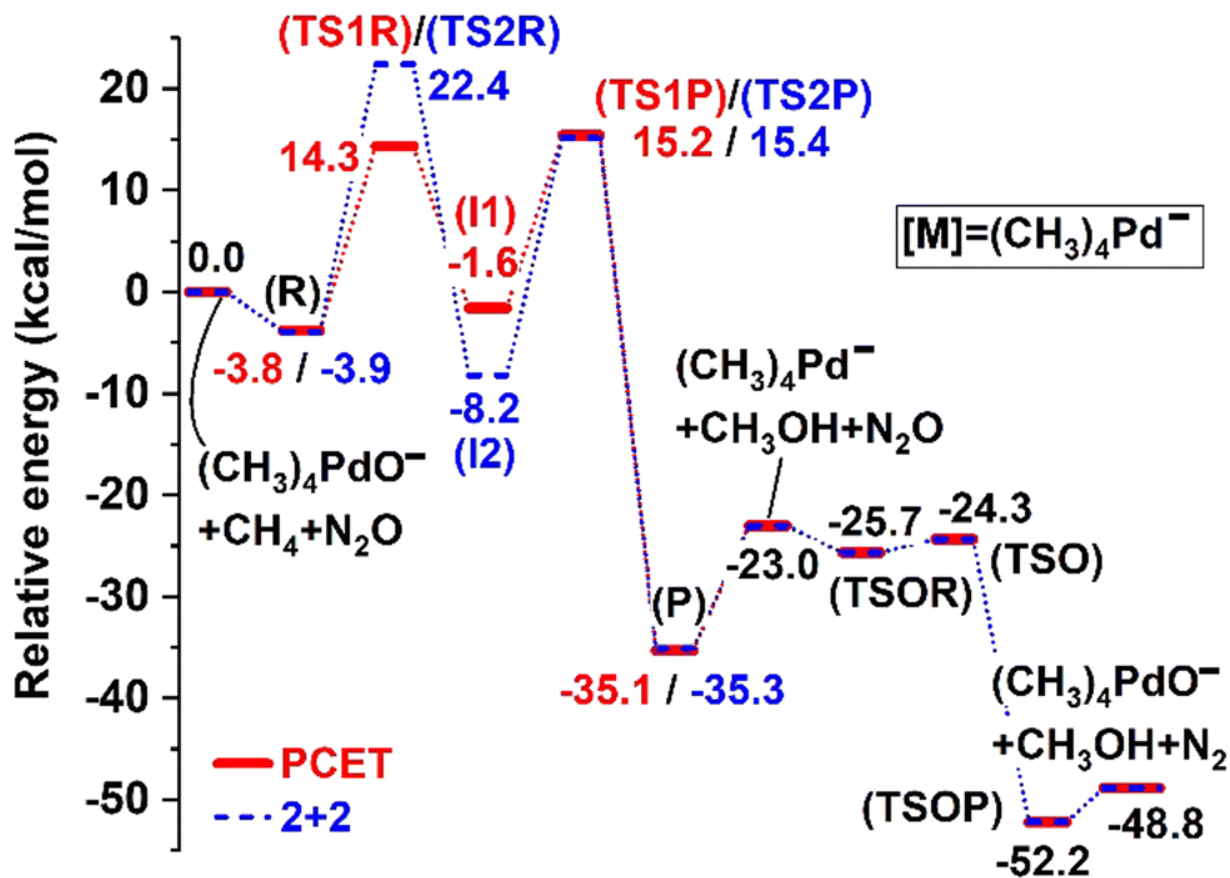


Figure 2.16. MN15/TZ potential energy diagram for the $\text{CH}_4 + \text{N}_2\text{O} \rightarrow \text{CH}_3\text{OH} + \text{N}_2$ reaction facilitated by $[\text{PdO}(\text{CH}_3)_4]^-$. The structures for both PCET and [2+2] are shown in figure 2.15.

2.9.3.2. Activation energy barrier for PCET and [2+2] for $\text{PdO}^-(\text{CH}_3)_4$ catalyzed reactions

The activation energies of TSs and interacting complexes in kcal/mol are listed in Table

2.2

Table 2.2. Activation energy barriers for the Ni, Pd, and Pt species with methyl or biphenyl (Bp) ligands.

Method	$E_a(1R)^a$	$E_a(1P)^b$	$E_a(2R)^c$	$E_a(2P)^d$	E_{TS}^e	E_{ox}^f
[M] = Pd(CH₃)₄						
MN15/DZ	17.4	16.4	23.5	22.9	13.3	2.3
MN15/TZ	18.2	17	26.3	23.3	12.3	4
CCSD(T)/ DZ	16.7	18.1	25.4	24.3	12	2
CCSD(T)/ TZ	17.5	18.7	28.1	24.7	11	0.2
[M] = Ni(CH₃)₄						
MN15/TZ	21.4	17.6	30.7	16.7	13.6	10.7
[M] = Pt(CH₃)₄						
MN15/TZ	21.9	20.7	28.4	36.8	12.3	0.4
[M] = Pd(Bp)₂						
MN15/TZ	19.3	16.9	28.5	20.3	12	7.6

^a Calculated as the energy difference between TS1R and R (see Figure 2.15).

^b Same as a footnote a but TS1P and I1.

^c Same as footnote [a] but TS2R and R.

^d Same as a footnote a but TS2P and I2.

^e Same as a footnote a but P and [M] + CH₃OH.

^f Same as a footnote a but TSOR and TSO.

Except for $E_a(2R)$, which fluctuates by 5 kcal/mol from MN15/DZ to CCSD(T)/TZ and corresponds to the first step of the [2+2] route ($R \rightarrow TS2R$), the activation barriers fluctuate within 2.5 kcal/mol for the various levels of theory. The system is not anticipated to pass this barrier because it is the highest one. The barriers are raised by using bigger basis sets and adding electron correlation effects through CCSD(T), but the energy required to liberate methanol from the catalytic center is unaffected. Since the difference between our best results, CCSD(T)/TZ, and MN15/TZ is less than 2.0 kcal/mol, MN15/TZ is believed to be fairly accurate and less computationally expensive than other catalytic models.

2.9.3.3. Activation energy barrier for PCET and [2+2] for $[\text{PdO}(\text{Bp})_2]^-$ catalyzed reactions

The bottom part of Table 2.2 lists the activation energy data for the Pd^- with biphenyl (Bp) ligands; Since biphenyl is a relatively non-reactive ligand and is employed often in organic/organometallic catalysis, it is chosen as the more practical ligand.¹⁰³⁻¹⁰⁶ The patterns hold across all four systems: The lowest barriers are of the 20 kcal mol⁻¹ order (16.9-21.9 kcal mol⁻¹) and are seen for the PCET mechanism, $E_a(1\text{R})/E_a(1\text{P})$. The second ($\text{CH}_3\text{-OH}$ recombination) stage exhibits a wide range of values (16.7-36.8 kcal mol⁻¹), but the [2+2] process demands a significant CH activation barrier, $E_a(2\text{R})$, ranging from 28.1 to 30.7 kcal mol⁻¹. The interaction energy between $[\text{M}]^-$ and CH_3OH is rather independent of the metal center or ligands (12.0-13.6 kcal/mol). Finally looking at the energy diagrams in Figure 2.14, it is obvious that the $[\text{CH}_3[\text{M}]\text{OH}]^-$ intermediate is no longer the very stable intermediate observed in the base of bare metals¹¹ (except for $\text{M} = [(\text{CH}_3)_4\text{Pt}]^-$). In addition, the oxidation step is nearly barrier-free (activation energies smaller than 11 kcal/mol) closing readily the catalytic cycle (see Figures 2.14 and 2.15). However, this should be considered an upper limit since there is an alternative mechanism found earlier with even smaller barriers.¹¹

2.9.3.4. Impact of ligand addition on E_{ea} of anionic center

Ligand addition improved the E_{ea} of best-performing metals (PdO^-). Our calculation shows $[\text{Ni}(\text{CH}_3)_4]^-$, $[\text{Pd}(\text{CH}_3)_4]^-$, and $[\text{Pt}(\text{CH}_3)_4]^-$ have vertical E_{ea} values at CCSD(T)/DZ (MN15/TZ) of 2.65 (2.96), 2.28 (2.56), and 2.35 (2.56) eV, respectively (energy difference between anionic and neutral species at the geometry of the anion). The disparity between MN15/TZ and CCSD(T)/DZ may be attributed to the technique, not the basis set, according to the MN15/DZ value for $[\text{Pd}(\text{CH}_3)_4]^-$, which is 2.58 eV. The vertical E_{ea} value for $[(\text{Bp})_2\text{Pd}]^-$ is 3.33 eV at MN15/DZ, which is 0.3 eV greater than $[(\text{CH}_3)_4\text{Pd}]^-$ and should be overestimated. These numbers all exceed the E_{ea}

of platinum, which has one of the highest E_{ca} of any metal (experimentally 2.128 eV).¹⁰⁷ Additionally, compared to bare metals, E_{ca} is essentially independent of the metal (1.156/1.04 eV for Ni, 0.562/0.39 eV for Pd, and 2.128/2.02 eV for Pt experimentally/CCSD(T)/DZ).

2.9.3.5. Natural Orbital Analysis (NO) of $\text{MO}^-(\text{CH}_3)_4$

The neutral form of Pd, Pt, Ni, and Fe are always closed-shell singlets, while their anions always have a doublet spin multiplicity with one unpaired electron on the metal. According to the Natural Population Analysis^{108, 109}, the unpaired electron in Figure 2.17 suggests that the extra electron is mostly shared by the Pd atom and two methyl groups. These two methyl units have an initial positive charge of (+0.16) and are given 0.36 electrons, whereas the metal has an initial positive charge of (+0.41) and is given 0.15 electrons. Only 0.06 e is added to the other two methyl groups, which already have a charge of 0.37. In conclusion, $[\text{Pd}(\text{CH}_3)_4]^-$ has charges of +0.26 for Pd and $-(0.19/0.43)$ for the two distinct methyl groups. The metallic charge on Pd remains almost unchanged when oxygen bonds to it (+0.27), while 0.14 electrons from each methyl group go to the oxygen center, which has a charge of 0.55. This is a sign of the cooperation between the metal and the ligands, where the ligands serve as an electron bank throughout the reaction.

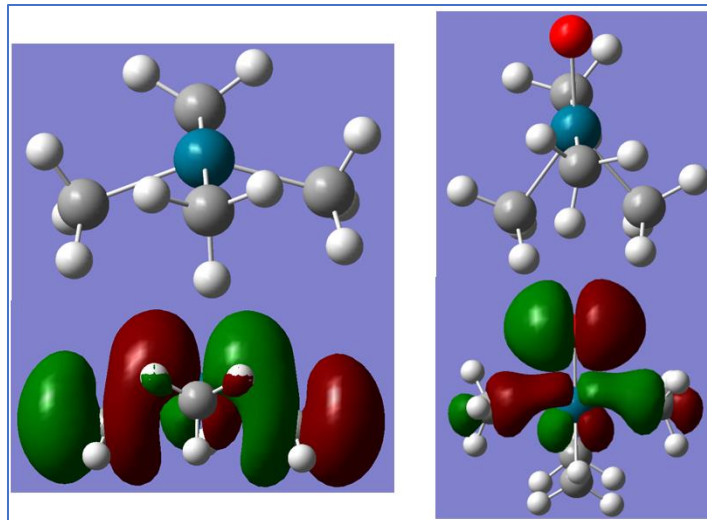


Figure 2.17. Natural orbital (NO) analysis of doublet $[\text{Pd}(\text{CH}_3)_4]^-$ and $[\text{PdO}(\text{CH}_3)_4]^-$ showing the spin density of the singly occupied orbital localized mainly on metal and the two bent methyl groups.

2.9.3.6. Reaction rate constant prediction from DFT free energies

The free energy diagrams at 298.15 K and 1.0 atm pressure were considered. The harmonic approximation, as implemented in Gaussian.¹¹⁰, yields free energy. Methanol may be quickly removed from the catalytic center without being overoxidized since the entropic factor reduces the energy required for its release to less than 2.0 kcal/mol.

We carried out a kinetic study to assess the performance of the chosen catalysts, pinpoint the predominant reaction pathway, and determine the rate-determining step. For each of the five reaction stages, we estimated the forward and reverse rate constants based on the formula below^{9, 111, 112}.

$$k = \frac{RT}{h} \left(\frac{RT}{p} \right)^n e^{-\Delta G^\ddagger/RT} \quad (2.2)$$

where k_B , T , p , h , ΔG^\ddagger , and R are Boltzmann's constant, temperature, pressure, Planck's constant, free energy activation barrier, and the universal gas constant, respectively ($n = 0/1$ for first/second order reaction steps).

The calculated k values utilized in the kinetics investigations are shown in Table 2.3. To solve the differential equations for the corresponding chemical kinetics equations, we used the COPASI program and took into account a 10% catalyst.⁸⁸ We evaluate the catalytic effectiveness using the half-life time ($t_{1/2}$) required to produce 50% of CH_3OH . To calculate the cycle's turnover frequency (TOF) and energetic span (E), we also used the energetic span model^{9, 111}. Since the PCET mechanism dominates exclusively in the COPASI work, we consider the PCET energy landscape for the energetic span model.

Table 2.3. Rate constants (k) for the reaction steps of Figure 2.15, and $t_{1/2}$, TOF, ΔE for the overall catalytic cycle employing $[M]O^-$ as catalysts. The notation $1.11E\pm 11$ means $1.11 \times 10^{\pm 11}$. Initial concentrations for CH_4 , N_2O and Catalyst ($[M]^-$) are 1 M, 1M and 0.1 M respectively.

Reaction step	$[Ni(CH_3)_4]^-$	$[Pd(CH_3)_4]^-$	$[Pt(CH_3)_4]^-$	$[Pd(Bp)_2]^-$
$[M]O^- + CH_4 \rightarrow I1$	3.16E+01	2.68E+02	2.26E-01	2.81E+02
$I1 \rightarrow [M]O^- + CH_4$	4.15E+01	1.51E+01	9.22E+01	5.49E+00
$I1 \rightarrow [M]^- + CH_3OH$	4.78E-03	1.28E-02	2.27E-05	1.39E-01
$[M]^- + CH_3OH \rightarrow I1$	5.41E-28	4.07E-24	9.92E-22	5.40E-20
$[M]O^- + CH_4 \rightarrow I2$	3.66E-09	8.05E-05	2.89E-07	2.40E-06
$I2 \rightarrow [M]O^- + CH_4$	1.04E-06	1.75E-08	7.25E-11	2.11E-10
$I2 \rightarrow [M]^- + CH_3OH$	2.15E+01	4.62E-05	4.49E-13	1.44E-02
$[M]^- + CH_3OH \rightarrow I2$	4.70E-26	4.43E-24	3.04E-23	6.22E-20
$[M]^- + N_2O \rightarrow [M]O^- + N_2$	9.79E+01	1.08E+06	5.56E+09	2.44E+06
$[M]O^- + N_2 \rightarrow [M]^- + N_2O$	6.57E-13	6.44E-11	5.12E-16	3.02E-13
$t_{1/2} / s$	3077	419	Undefined ^a	37.5
TOF / s^{-1}	1.40E-04	5.40E-03	2.30E-09	9.30E-02
$\Delta E / kcal/mol$	22.7	20.2	29.2	18.6

^a The reaction does not proceed beyond the first step (CH activation).

Rate constants (k) are in s^{-1} unit.

Our calculations support that the PCET mechanism (through I1) is faster and the primary route to the products, and that the CH activation phase, $[M]O^- + CH_4 \rightarrow I1$, invariably determines the rate (has the lowest rate constant and it is the rate-determining step), and that the oxygen reloads of the metal minimally contributes to the total rate. The initial reactants, $[M]O^- + CH_4$, are predicted to be the TOF-determining intermediate (TDI) and TS1P is predicted to be the TOF-determining transition state (TDTS) via the energetic span model (see Figure S11 in reference¹⁰²). This suggests that future research should consider both phases ($R \rightarrow I1 \rightarrow P$).

By contrasting the various systems, we observe that $M = [Pd(Bp)_2]^-$ has the lowest $t_{1/2}$, lowest ΔE , and highest TOF. The performance of $M = [Ni(CH_3)_4]^-$ and $[Pd(CH_3)_4]^-$ is also excellent, in contrast to $M = [Pt(CH_3)_4]^-$, whose high barriers prevent the reaction from being

completed. The $[(\text{Bp})_2\text{PdO}]^-$ looks to be a good catalyst given our anticipated $\Delta E = 18.6$ kcal/mol for $M = [(\text{Bp})_2\text{Pd}]^-$ and the precision of our electronic structure approaches (2 kcal/mol). Additionally, given the change in ΔE from four methyl ligands to two Bp ligands (18.6 to 22.7 kcal/mol), the ligands appear to offer some flexibility. Although Pd^- appears to be the most advantageous choice, the performance of Ni^- (as opposed to Pt^-) can be further refined by suitable ligands and result in a low-cost alternative. We also did computations for $M = [\text{Fe}(\text{CH}_3)_4]^-$ in this way. Our MN15/TZ data show that Fe, which has high activation barriers, performs relatively poorly. The identical patterns were discovered for "bare" FeO .¹¹ The approach of concentrating initially on pure oxides and subsequently adding methyl-type ligands for practical applications is supported by these tendencies.

2.10. Conclusion and final remarks

We demonstrate that the activation barriers for the conversion of methane to methanol may be reduced when metal oxide anionic units are complexed with the appropriate ligands. Adding the methyl-type ligands raises the metal center's attraction for electrons, stabilizing the metal's negative charge besides altering the metal center vacant sites available for substrate binding, thus favoring one reaction mechanism over the other such as following PCET and eliminating the [2+2] stable intermediate that was inhibiting the catalytic cycle in case of bare TMs. Our kinetic study demonstrates the $[(\text{Bp})_2\text{PdO}]^-$ has a strong potential to be an MTM catalyst. Finally, we found that the performance was highly both metal and ligand-dependent, but the ligand addition has a strong influence on the catalytic efficiency of poor-performing metals such as Ni^- .⁷

3. CHAPTER 3: TM-Catalyzed Carbon Dioxide Reactions with Unsaturated Alkanes

3.1. Significance and Background

Carbon Dioxide (CO₂) is an essential component of photosynthesis, and keeping a delicate balance between the levels produced and consumed is crucial to the survival of our planet. Sadly, aberrant human activity has recently caused its atmospheric levels to exhaust the geosphere's buffering capacity. Beside its direct impact on environmental warming, the economic potential of CO₂ as a freely available and sustainable raw material for fine chemicals has sparked several efforts worldwide to study various routes of its transformations. CO₂ can be catalytically converted into a variety of valuable chemicals such as CO, CH₄, and C₂H₄. Given the fact that CO₂ carbon is at the highest oxidation state, the only way to activate it is through reduction. Several promising catalysts have been developed that can facilitate the CO₂ reaction with hydrogen gas using different polyamines to capture CO₂ and a molecular ruthenium catalyst to produce methanol.¹¹³⁻¹¹⁵ The shortcoming of this method is the high energy cost required for CO₂ hydrogenation and amine decomposition-degradation. Prakash has also explored the use of solid adsorbents such as CaO, MgO, and hydrotalcite which are functional at high temperatures.

Alternatively, in a different approach, basic sorbents such as Ca(OH)₂, KOH, and NaOH were also utilized; however, they all require high temperatures to be regenerated which makes the whole process impractical.¹¹⁶ The negatively charged TMs efficiency in activating CO₂ has been reported by Bowen et al.¹¹⁷⁻¹¹⁹ Bowen's work has shown not only that Pt⁻ can efficiently activate CO₂ but also it forms a chemisorbed species (Pt⁻ covalently bound to CO₂) that is intriguingly stable. Furthermore, Bowen's work represents the first systematic experimental work showing the efficacy of negatively charged TMs such as Ni⁻, Pd⁻, Cu⁻, and Ag⁻ in CO₂ activation confirmed by high stable peak in mass spectroscopy and further confirmed by computational study.^{54, 117, 118}

Such efficiencies have been further confirmed for carbon monoxide catalytic conversion by Pt⁻ clusters.¹²⁰ Similarly, Weber et al. have reported that Sn⁻, Mn⁻, and Fe⁻ can activate CO₂ efficiently.^{121, 122} The benefit of using anionic metal centers in CO₂ conversion reactions is having a single step of CO₂ capture and conversion by TMs owing to their extra electron that can migrate to CO₂ via C atom and activate the molecule. Utilizing CO₂ as a synthon to produce more chemically useful entities usually involves either C-C or C-O catalytically driven bond formations.¹²³⁻¹²⁵ In a process known as carboxylation, CO₂ can react catalytically with a variety of hydrocarbons, specifically unsaturated ones, transforming CO₂ into a variety of chemicals like lactones and acrylic acid.¹²⁶⁻¹²⁹ Several reactions have been published in the past reporting five-membered metalo-rings produced from zero-valent nickel (Ni⁰) or zero-valent palladium (Pd⁰) as well as co-oligomerization of 1,3-dienes with CO₂, which proceeds via a bis- π -allyl intermediate.^{97, 130-135} To our knowledge, there is scarce computational data available on the energetics, geometries of intermediates and transition states that lead to delta lactone (δ -lactones) production from the readily available ethene. In this chapter, we have investigated the catalytic potential of the following TMs: Pt⁻, Pd⁻, and Ni⁻ on the CO₂ carboxylation reaction using ethene substrate. Both free and ligated forms of these metals were studied using the DFT method.

3.2. Computational details

All DFT calculations were performed in gas phase using Gaussian 16 software.^{26, 110} Equilibrium structures were obtained by geometry optimization using MN15 functional⁵⁷ and LANL2DZ pseudopotential basis set²³ that was applied to the metal, carbon, hydrogen, and oxygen atoms. The optimized structures were used to perform a single point energy calculation using MN15 and augmented correlation consistent polarized valence triple zeta basis sets (aug-cc-PVTZ) that were applied for C, H, and O atoms, while aug-cc-PVTZ-PP was used for TMs. Harmonic

vibrational frequency calculations were employed to confirm the structures were properly optimized. Intrinsic reaction coordinate (IRC)¹³⁶ was used to confirm the direct connection between each transition state and its reactants and products.

3.3. Proposed catalytic cycle of δ -lactone formation.

The initial step is the CO₂ capture and activation by anionic TM, followed by CO₂ insertion between coordinated ethylene and the metal leading to two types of metal rings depending on whether a C-C or C-O coupling reactions take place, represented by TS1 and TS2 in Figure 3.1. Subsequently, another ethylene molecule will coordinate to the metal center, and subsequent seven-membered metal ring formation will occur via TS3, TS4, TS5, and TS6 depending on the point of attack of the second ethylene. The final step is the metal release and δ -lactone formation via TS7, TS8, and TS9. We have investigated all possible routes leading to the product formation using DFT-calculated energy profiles as shown in Figure 3.2. Considering all different combinations of transition states that can lead to the δ -lactone, a total of four pathways has been proposed as follows: (1) Pathway A: via TS1 \rightarrow TS5 \rightarrow TS9, Pathway B: via TS1 \rightarrow TS6 \rightarrow TS8, pathway C: via TS2 \rightarrow TS3 \rightarrow TS7, and Pathway D: via TS2 \rightarrow TS4 \rightarrow TS8. In this chapter, we elucidate the mechanism of C-C and C-O couplings and metal release and lactone formation mediated by atomic and ligated TMs.

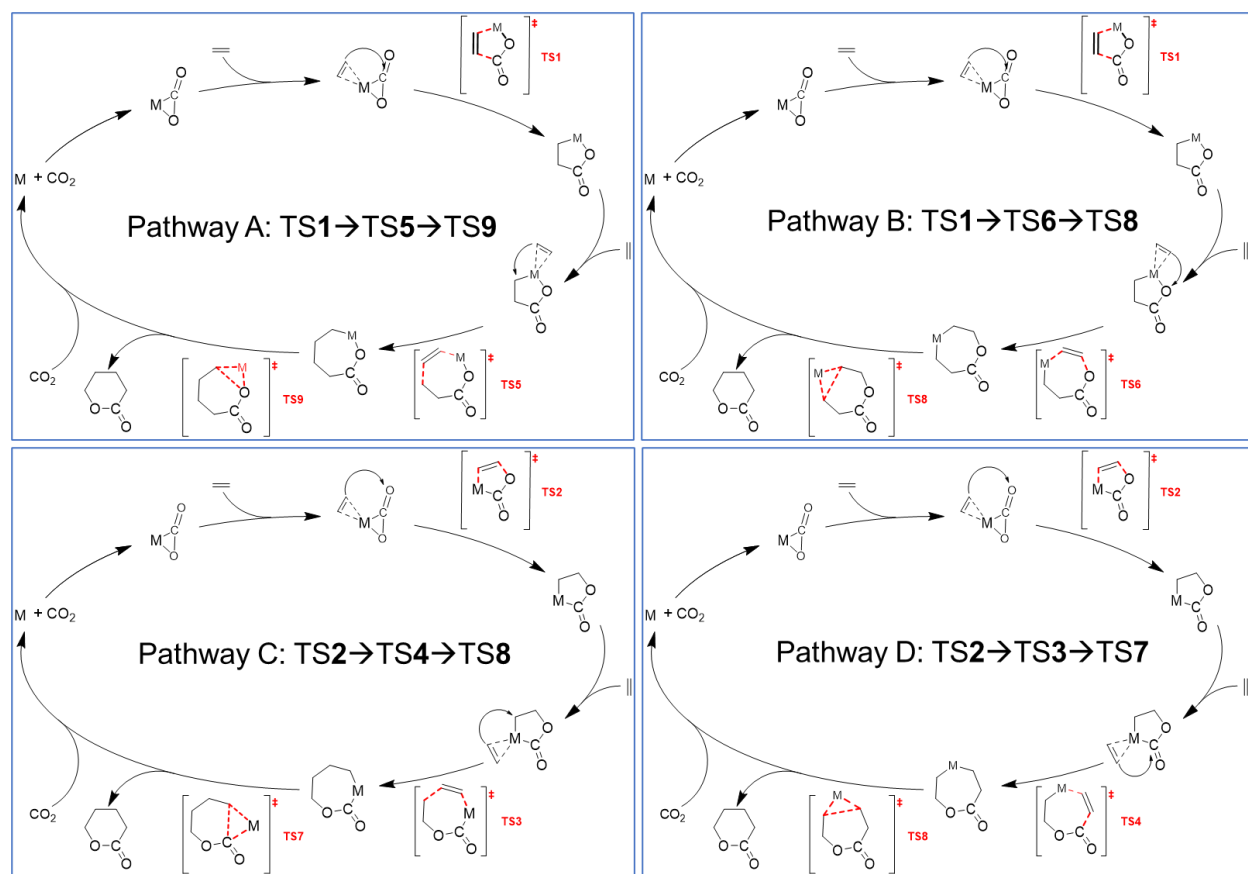


Figure 3.1. Different routes leading to lactone formation from CO₂ and two ethylene molecules. M= Pt⁻, Pd⁻, Ni⁻ in free and ligand-complexed forms.

3.4. Results

3.4.1. Atomic Pt⁻ catalyzed carboxylation with ethylene

Pathway A: TS1 → TS5 → TS9

The elementary reaction steps for CO₂ conversion into lactone are shown in Figure 3.2. The reaction begins with CO₂ capturing and coordination to Pt⁻ and subsequent first ethylene molecule coordination. The first C-C coupling occurs between ethylene and CO₂ via TS1 producing a five-membered metal ring with an energy requirement of 48.4 kcal/mol. A second ethylene will coordinate and C-C couples with the existing ethylene via TS5 producing a seven-membered metal ring that will ultimately undergo a C-O coupling that results in free metal release

and δ -lactone production. The energy barriers are 44.0 and 71.8 kcal/mol for TS5 and TS9, respectively.

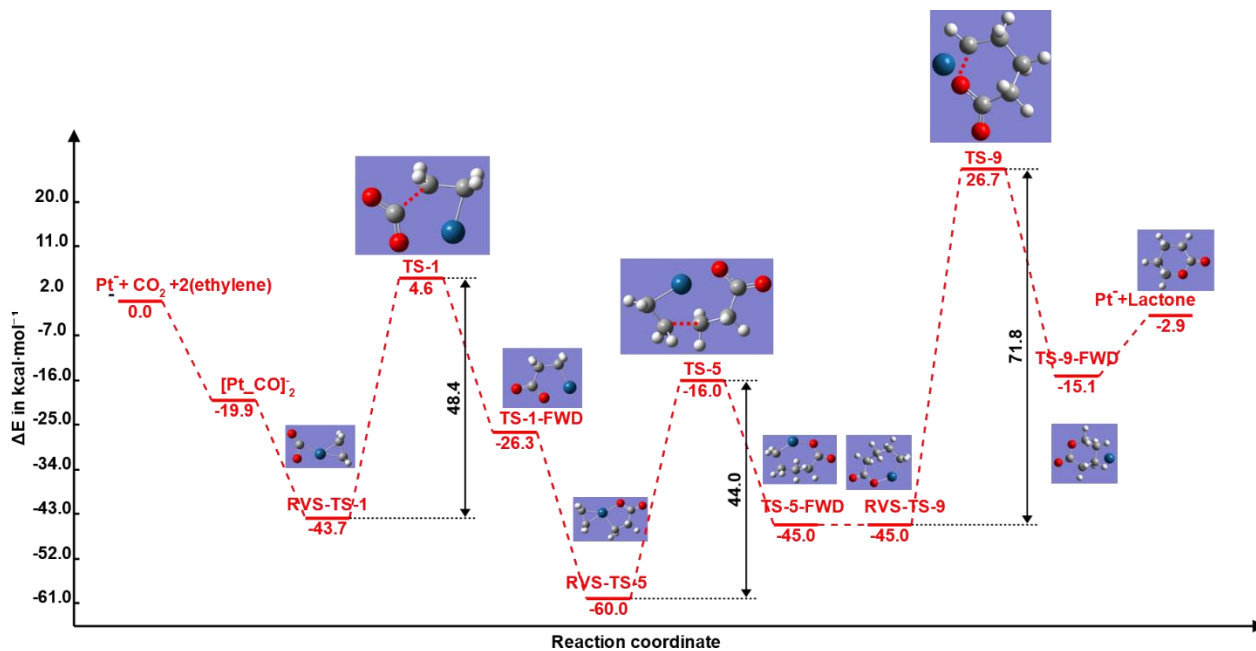


Figure 3.2. Free energy profile for Pt⁻-mediated C-C coupling (TS1 & TS5) and lactone formation (TS9). Energies are relative to the reactants.

Pathway B: TS1 → TS6 → TS8

In this path, a C-O coupling occurs between CO₂ and second ethylene via TS6 to make a seven-membered metal ring with an energy barrier of 48.4 kcal/mol followed by a C-O coupling to release the metal with an energy barrier of 48.8 kcal/mol. The energy diagram is shown in Figure 3.3.

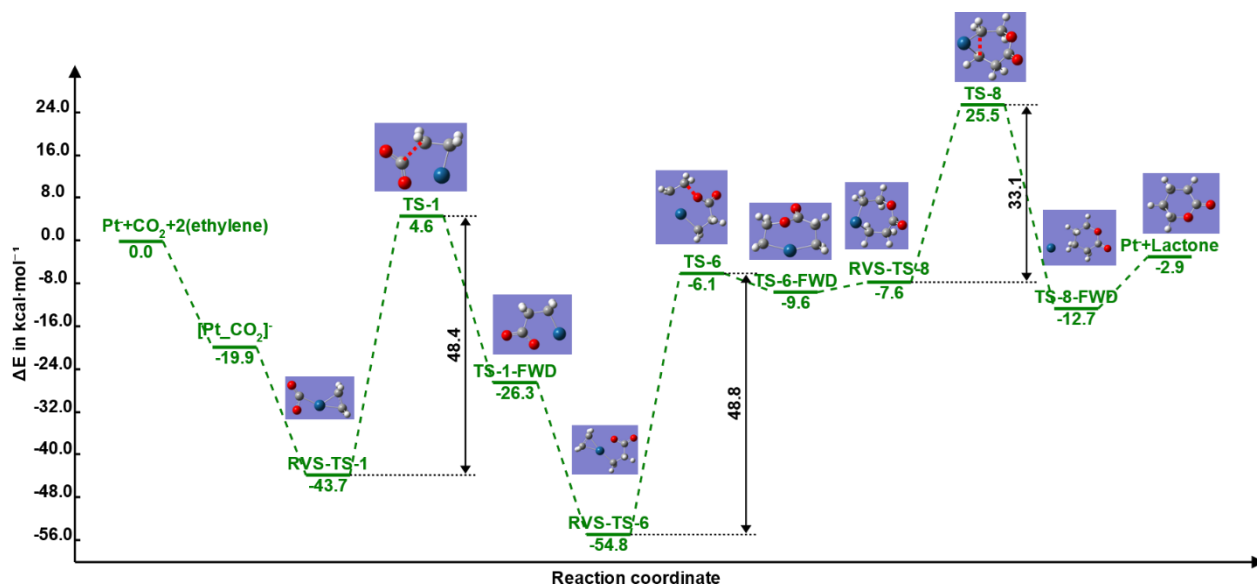


Figure 3.3. Free energy profile for the Pt-mediated C-C coupling (TS1), C-O coupling (TS6), and lactone formation (TS9). Energies are relative to the reactants.

Pathway C: TS2 → TS3 → TS7

In this path, TS2 involves a C-O coupling between CO₂ and ethylene and confers a five-membered metal ring with an energy barrier of 18.3 kcal/mol. TS3 is the C-C coupling between two ethylene molecules making a seven-membered metal ring, while TS7 is the C-C coupling of CO₂ carbon and ethylene carbon. Barriers for TS3 and TS7 are 48.6 and 20.4 kcal/mol, respectively (Figure 3.4)

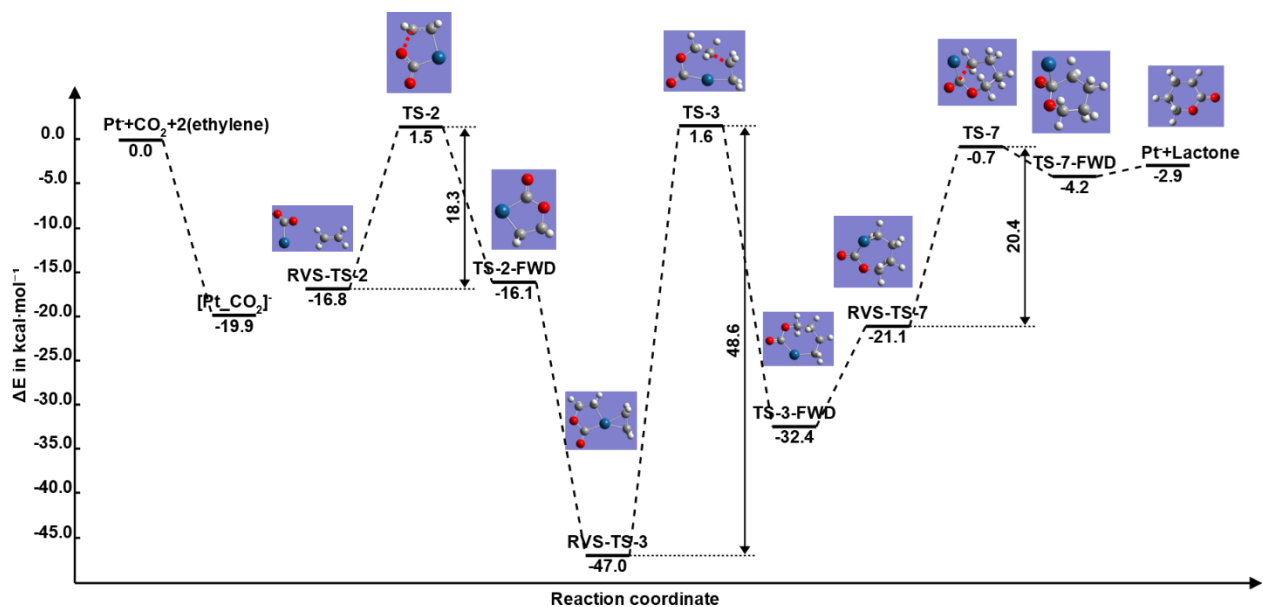


Figure 3.4. Free energy profile for the Pt⁻-mediated C-C coupling (TS3) and C-O coupling (TS2) and lactone formation (TS7). Energies are relative to the reactants.

Pathway D: TS2 → TS4 → TS8

The reaction pathway follows TS4 which represents a C-C coupling between the second ethylene and CO₂ with an energy requirement of 47.0 kcal/mol followed by TS8 which involves a C-C coupling between two ethylenes to release the metal and produces the lactone with an energy requirement of 33.1 kcal/mol.

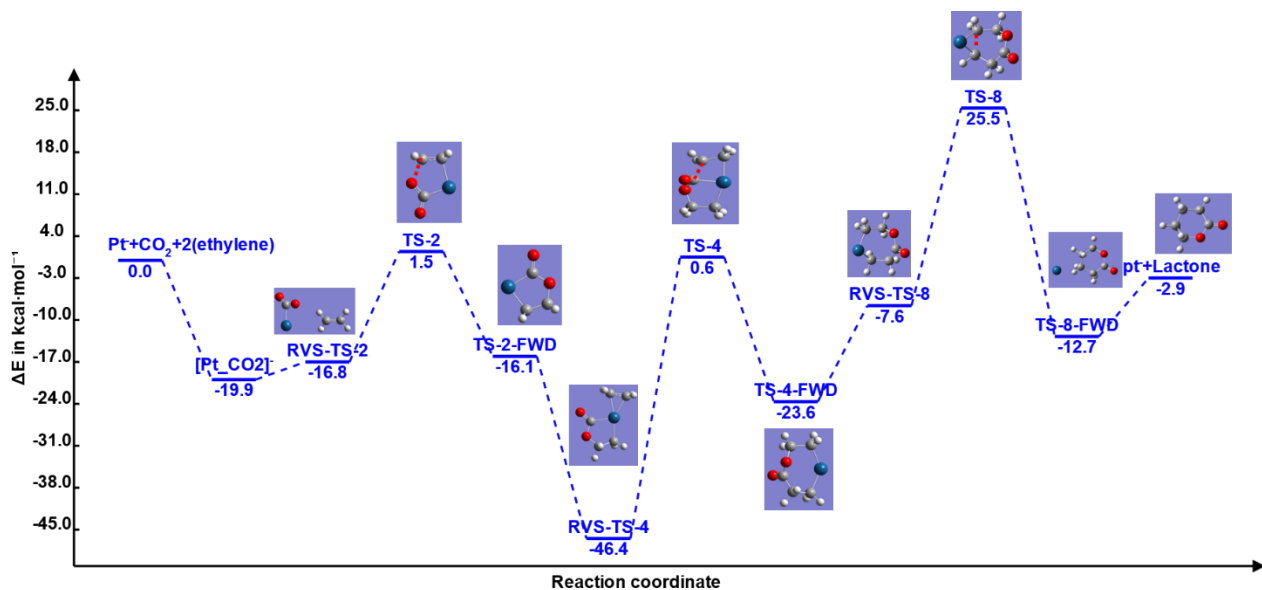


Figure 3.5. Free energy profile for the Pt⁻-mediated C-O coupling (TS2), C-C coupling (TS4), and lactone formation (TS8). Energies are relative to the reactants.

3.5. Discussion

3.5.1. Platinum-mediated five-membered metalolactone formation (TS1/TS2)

The oxidative coupling between ethylene and CO₂ is a well-established procedure mainly known to be mediated by zero-valent nickel (Ni⁰).^{7, 137} It is the first elementary step toward acrylic acid formation that occurs as a result of beta-elimination of hydrogen from the formed metalolactone. The previous work supports the initial coordination of ethylene first and subsequent CO₂ coordination to the metal since the former is relatively highly exothermic compared to the latter. In the present work, we considered CO₂ coordination to precede ethylene since both substrates can freely compete on the metal active site without any restrictions from a bound ligand. Figure 3.6 shows two possible pathways that lead to two different metalolactone depending on whether the O or the C of the CO₂ is bound to the metal in the metalolactone.

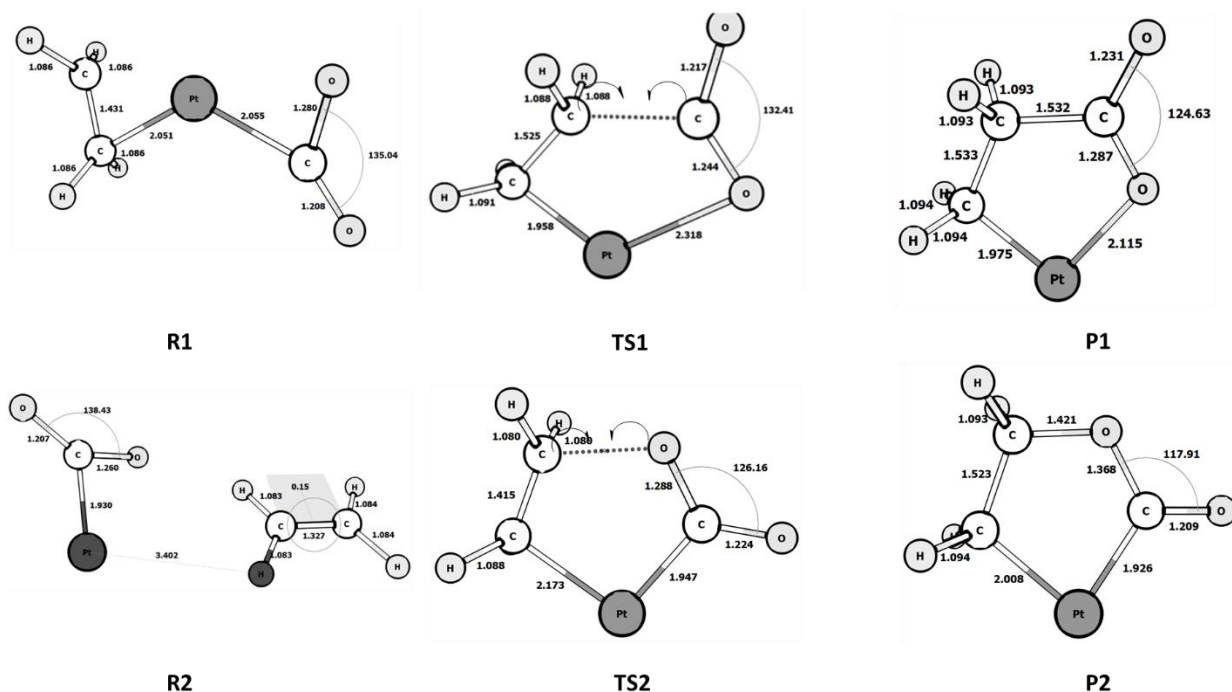


Figure 3.6. Optimized geometries of intermediates and transition states for metalolactone formation.

Observe that the Pt^- -coordinated CO_2 's average OCO angle is 130° , which significantly alters its electronic structure from a closed shell into an open shell system. The orbital with spin density in Pt^- - CO_2 is situated along the Pt^- - O axis, as seen in Figure 3.7. The O atom is more reactive than the C atom linked to Pt^- because of the partial spin density on the O center in the case of R2. As a result, the activation barrier in the TS2 situation is lower due to the increased efficiency of C-O coupling. The instability of the TS2 reactant (R2), where the ethylene is not within a coordination sphere of the metal center is also a contributing factor in lowering the TS2 barrier since the metal-carbon dissociation step is not a pre-disposing factor in TS2 initiation.

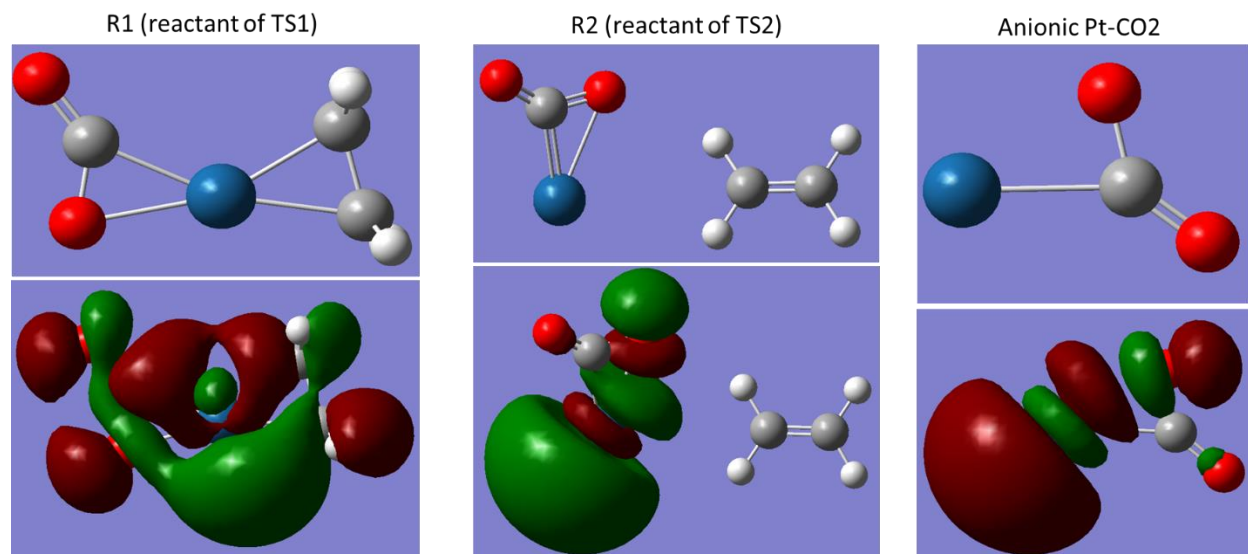


Figure 3.7. Natural orbital (NO) representation showing the spin density of the single electron in Pt^- (a) NO of the $[\text{ethylene-Pt-CO}_2]^-$ generated from the IRC calculation of TS1 (C-C coupling). (b) NO of the $[\text{ethylene-Pt-CO}_2]^-$ generated from IRC calculation of TS2 (C-O coupling). (c) is NO of $[\text{Pt-CO}_2]^-$ (added for comparison).

3.5.2. Seven-membered metalolactone formation via (TS3/TS4) or (TS5/TS6)

The two metalolactones produced from TS1 and TS2 can further undergo another transformation with an incoming ethylene molecule that coordinates to the metal center. Depending on the point of attack, following TS2, the incoming ethylene can undergo a C-C

coupling with either the C of the existing ethylene or with carbonyl's C vi TS3 and TS4, respectively. Similarly, following TS1, the incoming ethylene can perform a C-C or C-O coupling via TS5 and TS6 respectively. It is worth mentioning here that the four TSs involve ring opening of the metalolactone and subsequent C-C or C-O coupling with the incoming ethylene. The energy requirement for ring opening as well as the fact that the activated incoming ethylene attacks either a C or O atom inside a formed ring (both are sigma-bonded with Pt⁻) explains the high energy barriers of an average of 45 kcal/mol observed for TS3, TS4, TS5, and T6.

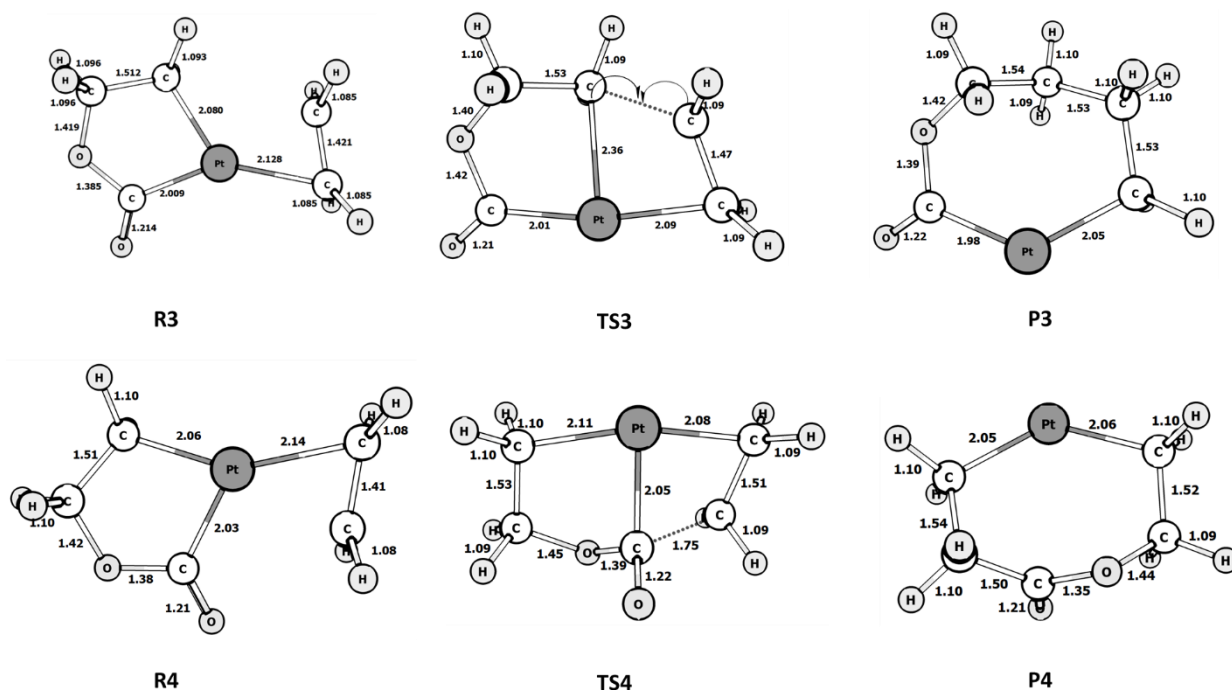


Figure 3.8. Optimized geometries of intermediates and transition states for 7-membered metalolactone formation.

3.5.3. Seven-membered metalolactone ring opening and metal release via (TS7/TS8/TS9)

The final step in lactone formation is the ring opening and metal release which occur via TS7, TS8, and TS9. In terms of energetic barriers, TS7 which involves the metal release from a

C_{sp} (carbonyl C) and a C_{sp^3} (ethane's C) is significantly lower than TS8 where the metal is released from two C_{sp^3} atoms. In TS9, the metal release energy barrier is significantly higher compared to TS7 and TS8 due to the higher bond dissociation energy of $Pt^- - O$ compared to that in $Pt^- - C$ ¹⁰⁷.

3.6. Ligand impact on Pt⁻-catalyzed carboxylation with ethylene

We considered the Bi-phenyl ligand (Bp) chelated with Pt⁻ and applied the same four different pathways for δ -lactone formation. The structure of the catalyst is shown below in figure 3.9

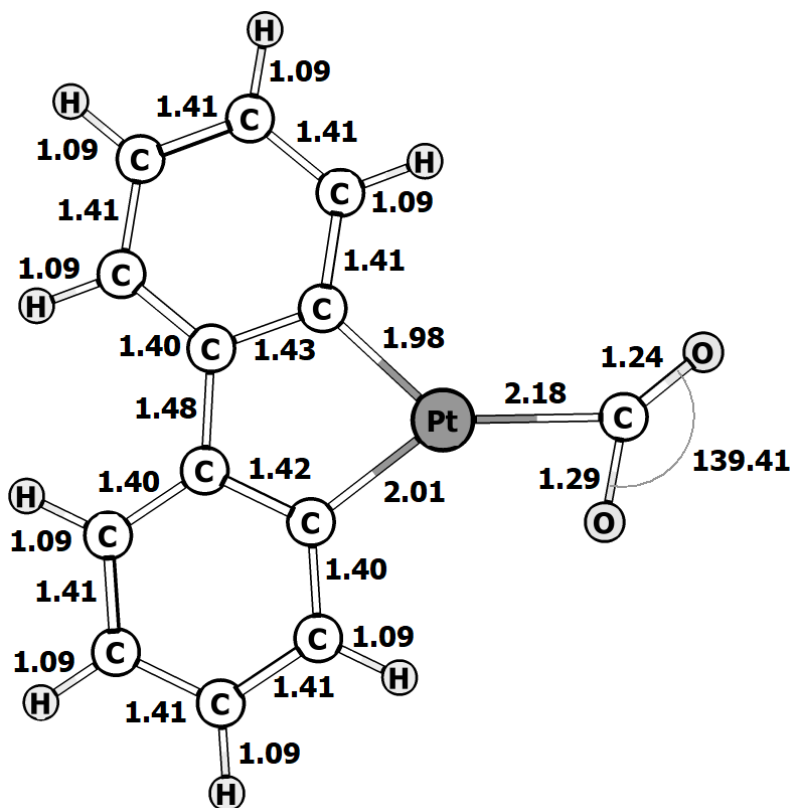


Figure 3.9. Optimized Pt⁻-based catalyst.

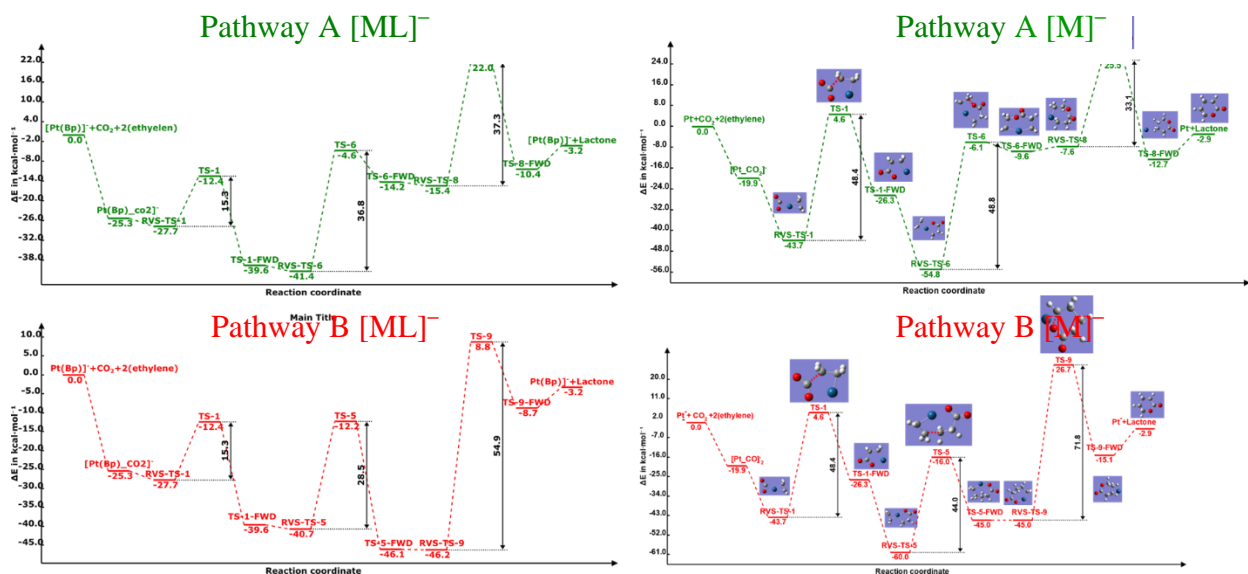


Figure 3.10. Energy landscape for atomic (right) and complexed Pt⁻ (left) for Pathways A & B.

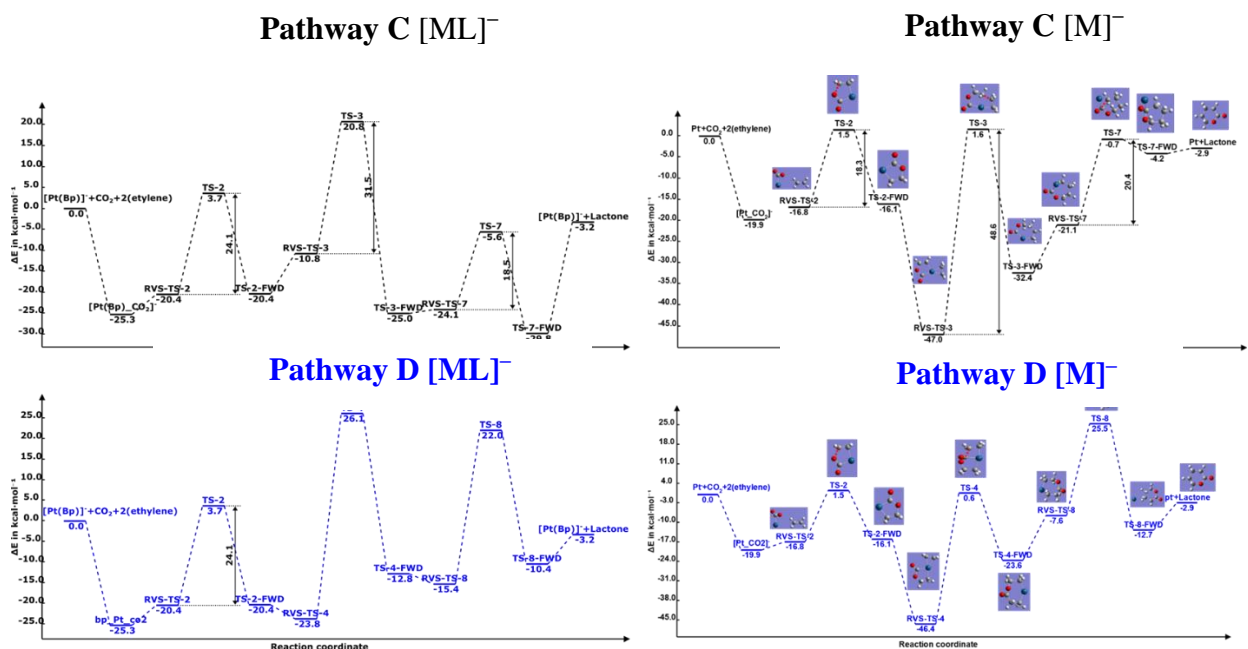


Figure 3.11. Energy landscape for atomic (right) and complexed Pt⁻ (left) for pathways C & D.

3.6.1. Results and Discussion

In terms of energetic profiles, the ligand introduction showed a significant impact by lowering the majority of transition states' activation barriers in routes A, B, C, and D. It is remarkably lowering the activation energy for TS1 but increasing that for TS2 in routes A and B. The ligand has altered the electronic density on the O-C-O molecule from being concentrated on one O atom to being distributed along the entire molecule especially the carbonyl C which is performing the C-C coupling with ethylene's C, as shown in figure 3.12, decreasing the activation energy barriers.

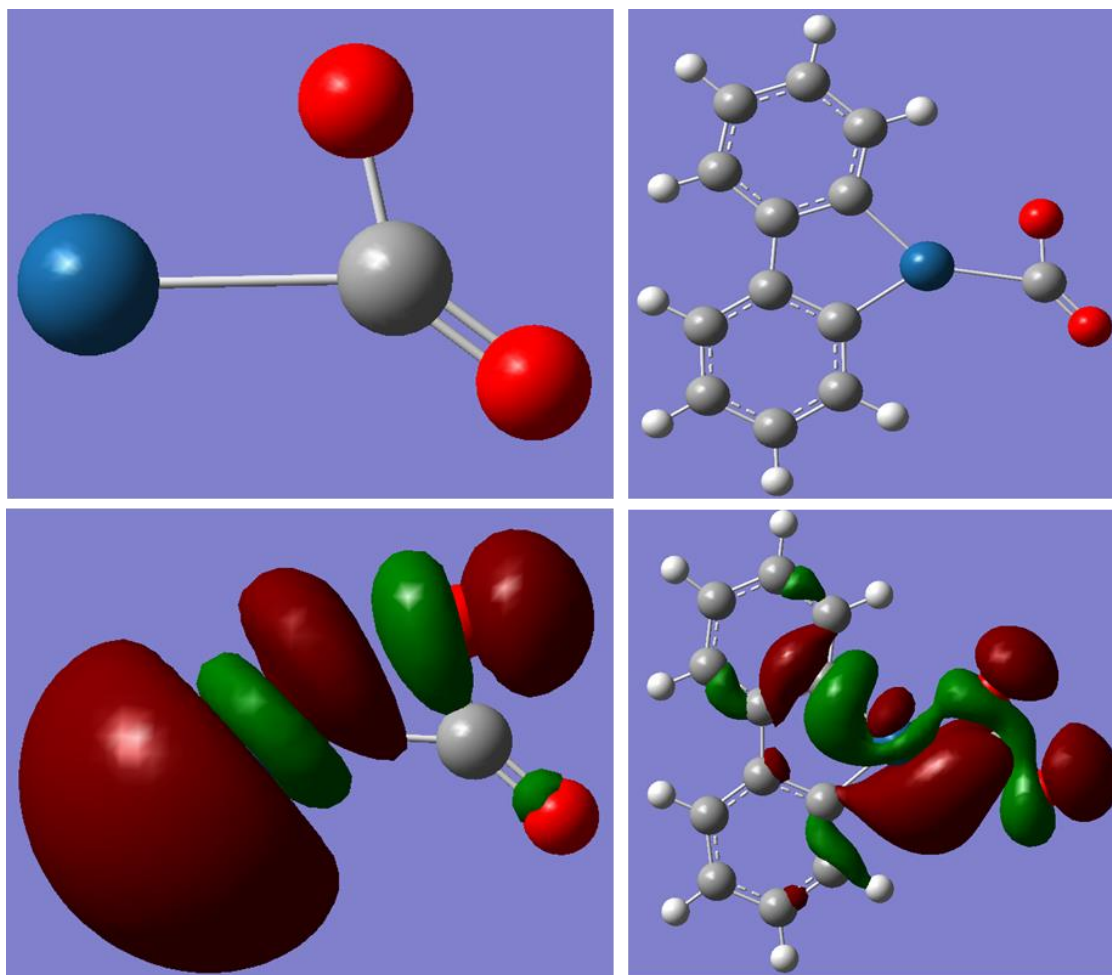


Figure 3.12. Natural orbital (NO) diagram showing the spin density of the single electron on atomic and complexed Pt.

Moreover, the ligand has another steric contribution in lowering the TS1 C-C coupling and increasing the TSs (C-O) barrier by competing with the ethylene on the metal center active site as shown in the same figure.

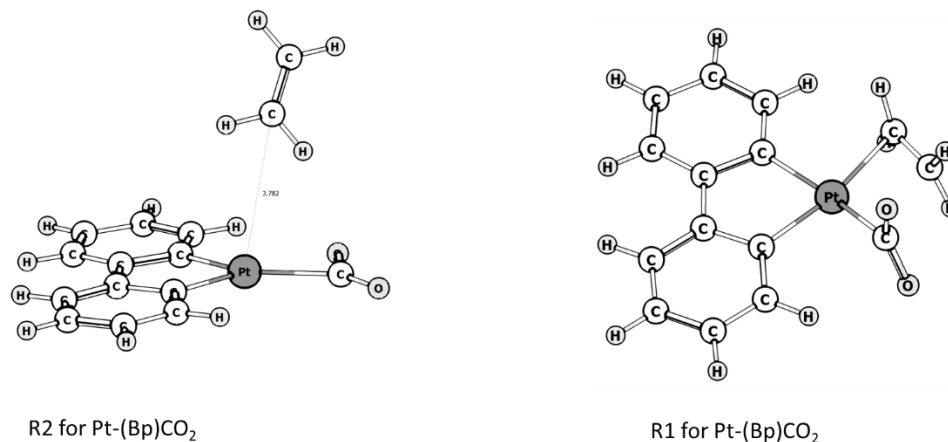


Figure 3.13. Ligand effect on the geometrical shape of reactants for TS1 (C-C) coupling and TS2 (C-O) coupling.

Collectively, based on energetic barriers, the best performance is observed in route B through $TS2 \rightarrow TS6 \rightarrow TS8$. While $TS2$ is a facile step, the subsequent $TS6$ and $TS8$ still have high energy barriers. Therefore, we decided to test the performance of other anionic metals to see if the metal identity can influence the activation barriers. We have tested the performance of another two anionic metals, nickel, and palladium, by applying the same level of theory and reproducing the four different pathways. The $Ni^-(Bp) + 2(\text{ethylene}) + CO_2$ and $Pd^-(Bp) + 2(\text{ethylene}) + CO_2$ energy diagrams are shown in Figure 3.14 and 3.15 respectively.

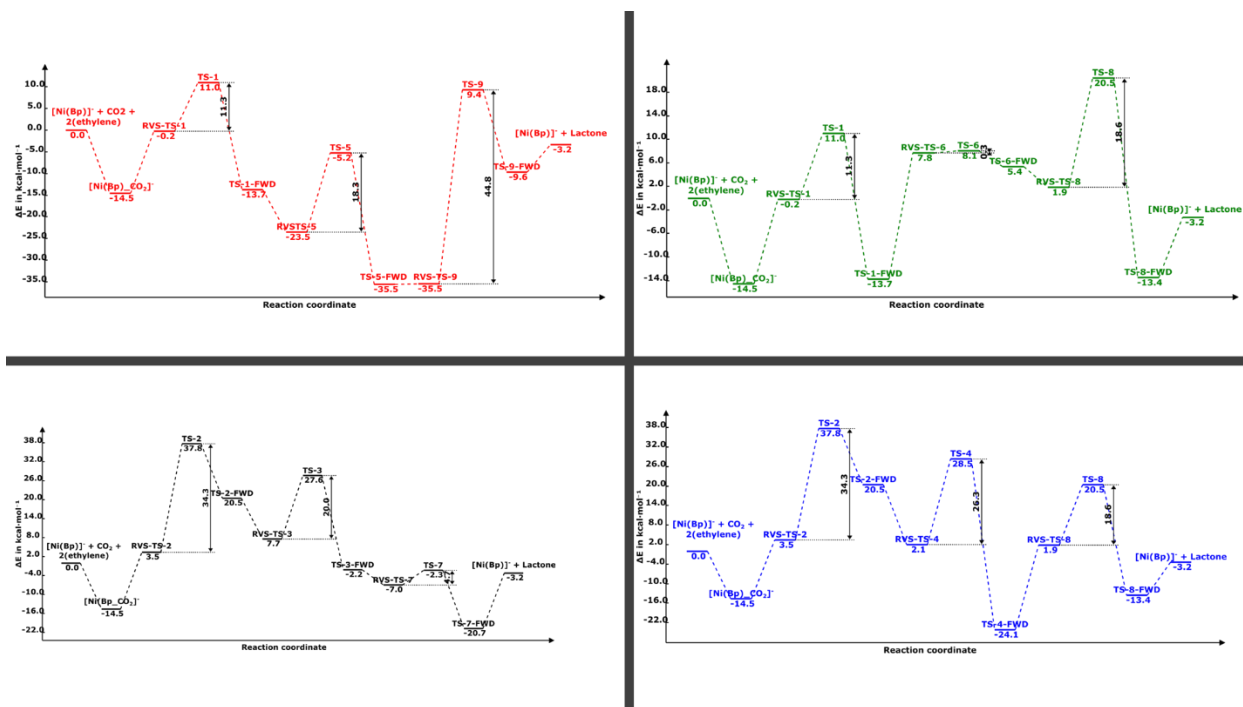


Figure 3.14. Ni⁻(Bp) catalyzed CO₂ reaction with ethylene.

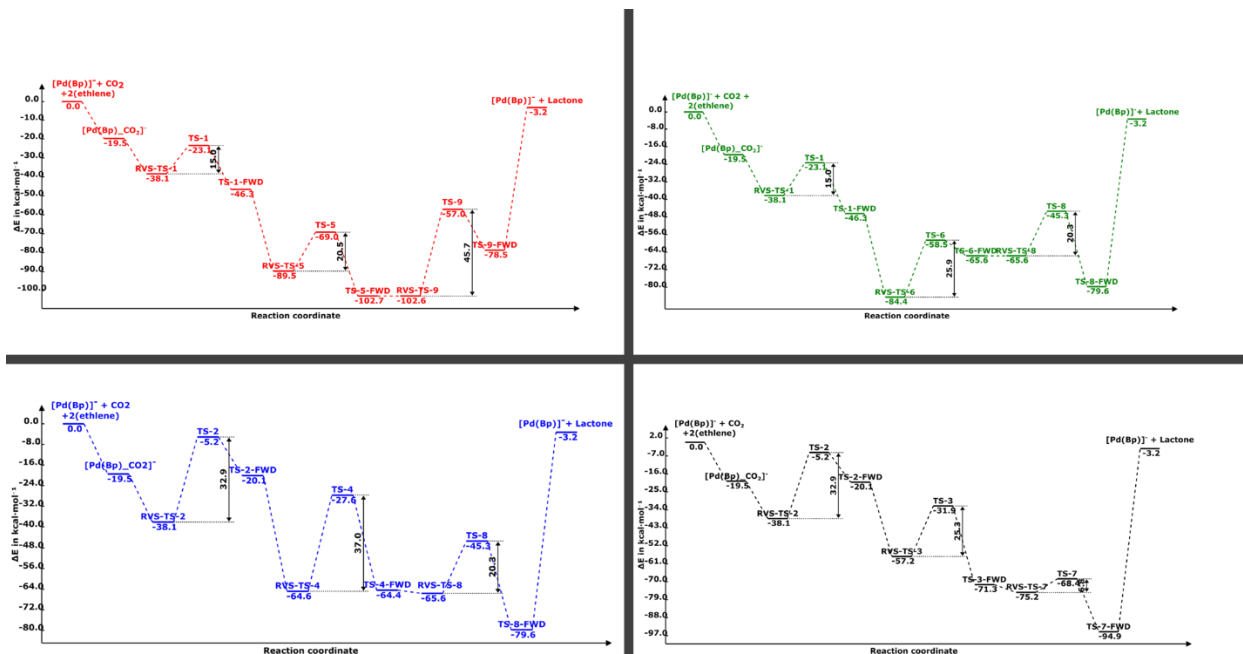


Figure 3.15. Pd⁻(Bp) catalyzed CO₂ reaction with ethylene.

Besides the ligand influence on the energetic profiles for the studied pathways, the metal identity played a role in reactions that involved C-C coupling reactions. Our calculations indicated that the metal-carbon Bond Dissociation Energy (BDE) was 67.25 kcal/mol, 59.75 kcal/mol, and

40.0 kcal/mol (calculated at MN15/aug-cc-PVTZ level of theory) for Pt⁻, Pd⁻ and Ni⁻, respectively with the following pattern: Pt-C > Pd-C > Ni-C considering the doublet spin state for all three metals. The formula used for BDE is shown below:

$$\text{BDE}_{\text{M-C}} = \text{E}[\text{CH}_3^\cdot] + \text{E}[\text{M}^\cdot] - \text{E}[\text{MCH}_3^\cdot] \quad (3.1)$$

However, this BDE pattern is not observed in the metal-oxygen bond where the BDE for all above three metals is similar with an average of 73.0 kcal/mol calculated at the same level of theory according to the formula below:

$$\text{BDE}_{\text{M-O}} = \text{E}[\text{OH}^\cdot] + \text{E}[\text{M}^\cdot] - \text{E}[\text{MOH}^\cdot] \quad (3.2)$$

The observed BDE_{M-C} pattern among Pt⁻, Pd⁻, and Ni⁻ is particularly important in understanding the TSs that involve metal release. In TS7, the TS activation energy is calculated to be 20.4, 18.3, 6.8, and 4.7 for Pt⁻, Pt⁻(Bp), Pd⁻(Bp) and Ni⁻(Bp), respectively, which agrees with the BDE_{M-C} observed previously. In TS8 and TS9, the same relationship holds between the metal identity and BDE_{M-C} for the corresponding metal. Moreover, the fact that complexed Pt⁻ follows this pattern compared to atomic Pt⁻ suggests ligand impact on lowering the activation energy of the three discussed TSs.

3.7. Conclusions

In this study, the mechanism of δ -lactone formation catalyzed by anionic TMs is explored for Pt⁻, Pd⁻, and Ni⁻. The effect of ligand introduction on activation energies of reaction barriers is also studied with all three metals. The initial step that involves the metalolactone formation involves either C-C or C-O couplings where the energy barriers are heavily dependent on the degree of ethylene and CO₂ activation by the metal catalyst. The subsequent steps involve both ring opening and a second ethylene addition through C-C and C-O couplings reactions. The activation energies in these steps can vary considerably by ligand introduction and metal identity variation or any combination of these two variables. The metal-carbon and/ or metal-oxygen BDE dictates the extent of activation energy required to overcome those barriers. Implications drawn from the current study can be applied to study the C-C and C-O couplings in other substrates.

REFERENCES

1. B. Chan, P. M. W. Gill and M. Kimura, *Journal of Chemical Theory and Computation*, 2019, **15**, 3610-3622.
2. R. J. Bartlett and G. D. Purvis, *International Journal of Quantum Chemistry*, 1978, **14**, 561-581.
3. K. Eller and H. Schwarz, *Chemische Berichte*, 1990, **123**, 201-208.
4. D. Schröder and H. Schwarz, *Angewandte Chemie International Edition in English*, 1990, **29**, 1433-1434.
5. D. Schröder and H. Schwarz, *Angewandte Chemie International Edition in English*, 1995, **34**, 1973-1995.
6. J. C. Védrine, *Catalysts*, 2017, **7**, 341.
7. J. Wu and X.-D. Zhou, *Chinese Journal of Catalysis*, 2016, **37**, 999-1015.
8. L. S. Sunderlin and P. B. Armentrout, *Journal of the American Chemical Society*, 1989, **111**, 3845-3855.
9. S. Kozuch and S. Shaik, *Accounts of Chemical Research*, 2011, **44**, 101-110.
10. S. Kozuch, *WIREs Computational Molecular Science*, 2012, **2**, 795-815.
11. S. Sader and E. Miliordos, *The Journal of Physical Chemistry A*, 2021, **125**, 2364-2373.
12. A. Szabo and N. S. Ostlund, *Modern quantum chemistry: introduction to advanced electronic structure theory*, Dover Publications, Mineola, N.Y, 1996.
13. P. Echenique and J. L. Alonso, *Molecular Physics*, 2007, **105**, 3057-3098.
14. S. R. Langhoff and E. R. Davidson, *International Journal of Quantum Chemistry*, 1974, **8**, 61-72.
15. E. R. Davidson, *Journal of Computational Physics*, 1975, **17**, 87-94.
16. J. A. Pople, R. Krishnan, H. B. Schlegel and J. S. Binkley, *International Journal of Quantum Chemistry*, 1979, **16**, 225-241.
17. K. Raghavachari, G. W. Trucks, J. A. Pople and M. Head-Gordon, *Chemical Physics Letters*, 1989, **157**, 479-483.
18. P. Hohenberg and W. Kohn, *Physical Review*, 1964, **136**, B864-B871.
19. W. Kohn and L. J. Sham, *Physical Review*, 1965, **140**, A1133-A1138.
20. S. Lehtola, C. Steigemann, M. J. T. Oliveira and M. A. L. Marques, *SoftwareX*, 2018, **7**, 1-5.
21. A. D. Becke, *The Journal of Chemical Physics*, 1993, **98**, 5648-5652.
22. H. S. Yu, X. He, S. L. Li and D. G. Truhlar, *Chemical Science*, 2016, **7**, 5032-5051.
23. L. E. Roy, P. J. Hay and R. L. Martin, *Journal of Chemical Theory and Computation*, 2008, **4**, 1029-1031.
24. W. R. Wadt and P. J. Hay, *The Journal of Chemical Physics*, 1985, **82**, 284-298.
25. P. D. Joseph W. Ochterski, 2000, Gaussian, IncJune 2, 2000.
26. M. J. Frisch, G. W. Trucks, H. B. Schlegel, G. E. Scuseria, M. A. Robb, J. R. Cheeseman, G. Scalmani, V. Barone, G. A. Petersson, H. Nakatsuji, X. Li, M. Caricato, A. V. Marenich, J. Bloino, B. G. Janesko, R. Gomperts, B. Mennucci, H. P. Hratchian, J. V. Ortiz, A. F. Izmaylov, J. L. Sonnenberg, Williams, F. Ding, F. Lipparini, F. Egidi, J. Goings, B. Peng, A. Petrone, T. Henderson, D. Ranasinghe, V. G. Zakrzewski, J. Gao, N. Rega, G. Zheng, W. Liang, M. Hada, M. Ehara, K. Toyota, R. Fukuda, J. Hasegawa, M. Ishida, T. Nakajima, Y. Honda, O. Kitao, H. Nakai, T. Vreven, K. Throssell, J. A. Montgomery Jr., J. E. Peralta, F. Ogliaro, M. J. Bearpark, J. J. Heyd, E. N. Brothers, K.

- N. Kudin, V. N. Staroverov, T. A. Keith, R. Kobayashi, J. Normand, K. Raghavachari, A. P. Rendell, J. C. Burant, S. S. Iyengar, J. Tomasi, M. Cossi, J. M. Millam, M. Klene, C. Adamo, R. Cammi, J. W. Ochterski, R. L. Martin, K. Morokuma, O. Farkas, J. B. Foresman and D. J. Fox, Wallingford, CT2016.
27. D. A. McQuarrie and J. D. Simon, *Molecular thermodynamics*, University Science Books, Sausalito, Calif, 1999.
 28. G. A. Petersson, in *Theoretical Chemistry Accounts: New Century Issue*, eds. C. J. Cramer and D. G. Truhlar, Springer Berlin Heidelberg, Berlin, Heidelberg 2001, pp. 190-195.
 29. S. Canneaux, F. Bohr and E. Henon, *Journal of Computational Chemistry*, 2014, **35**, 82-93.
 30. EPA, Environmental Protection Agency, <https://www.epa.gov/>, Accessed 11/07, 2019.
 31. A. York, T. Xiao and M. Green, *Topics in Catalysis*, 2003, **22**, 345-358.
 32. S. Kioes and W. Liebner, *Journal of Natural Gas Chemistry*, 2004, **13**, 71-78.
 33. G. C. Chinchin, P. J. Denny, J. R. Jennings, M. S. Spencer and K. C. Waugh, *Applied Catalysis*, 1988, **36**, 1-65.
 34. The Methanol Industry: Methanol Institute: www.methanol.org, <https://www.methanol.org/the-methanol-industry/>.
 35. W. A. Chupka and J. Berkowitz, *The Journal of Chemical Physics*, 1971, **54**, 4256-4259.
 36. Sunney I. Chan^{a,*}, Chih-Cheng Liu^a, Steve S.-F. Yu^a 2018, 'An efficient catalyst for selective methane oxidation under ambient conditions', *The 8th Tokyo Conference on Advanced Catalytic Science and Technology (TOCAT8), Yokohama, Japan, August 5 to 10, 2018*.
 37. H. D. Gesser, N. R. Hunter and C. B. Prakash, *Chemical Reviews*, 1985, **85**, 235-244.
 38. J. W. Chun and R. G. Anthony, *Industrial & Engineering Chemistry Research*, 1993, **32**, 259-263.
 39. J. W. Chun and R. G. Anthony, *Industrial & Engineering Chemistry Research*, 1993, **32**, 788-795.
 40. G. S. Walker, J. A. Lapszewicz and G. A. Foulds, *Catalysis Today*, 1994, **21**, 519-526.
 41. V. Y. B. Vladimir S. Arutyunov, and Vladimir I. Vedeneev, *Industrial & Engineering Chemistry Research*, 1995, **34**, 4238—4243.
 42. A. S. Chellappa and D. S. Viswanath, *Industrial & Engineering Chemistry Research*, 1995, **34**, 1933-1940.
 43. A. S. Chellappa, S. Fuangfoo and D. S. Viswanath, *Industrial & Engineering Chemistry Research*, 1997, **36**, 1401-1409.
 44. R. Horn and R. Schlögl, *Catalysis Letters*, 2014, **145**, 23-39.
 45. M. SOHRABI and L. VAFAJOO, *Journal of the Chilean Chemical Society*, 2009, **54**, 129-133.
 46. H. In Yeub, L. Seung Hwan, C. Yoo Seong, P. Si Jae, N. Jeong Geol, C. In Seop, K. Choongik, K. Hyun Cheol, K. Yong Hwan and L. Jin Won, *Journal of Microbiology and Biotechnology*, 2014, **24**, 1597-1605.
 47. I. Y. Hwang, S. H. Lee, Y. S. Choi, S. J. Park, J. G. Na, I. S. Chang, C. Kim, H. C. Kim, Y. H. Kim, J. W. Lee and E. Y. Lee, *Journal of Microbiology and Biotechnology*, 2014, **24**, 1597-1605.
 48. P. Nagababu, S. S. F. Yu, S. Maji, R. Ramu and S. I. Chan, *Catalysis Science & Technology*, 2014, **4**, 930-935.

49. N. Aristov and P. B. Armentrout, *The Journal of Physical Chemistry*, 1987, **91**, 6178-6188.
50. IPCC, 2005 - B. Metz, O. Davidson, H. de Coninck, M. Loos and L. Meyer (Eds). Cambridge University Press, UK. pp 431. Available from [Cambridge University Press](https://www.cambridge.org/core), The Edinburgh Building Shaftesbury Road, Cambridge CB2 2RU ENGLAND.
51. Y. Shiota and K. Yoshizawa, *Journal of the American Chemical Society*, 2000, **122**, 12317-12326.
52. A. Z. Msezane, Z. Felfli, K. Suggs, A. Tesfamichael and X.-Q. Wang, *Gold Bulletin*, 2012, **45**, 127-135.
53. A. Tesfamichael, K. Suggs, Z. Felfli and A. Z. Msezane, *arXiv [physics.chem-ph]*, 2014.
54. G. Liu, Z. Zhu, S. M. Ciborowski, I. R. Ariyaratna, E. Miliordos and K. H. Bowen, *Angewandte Chemie International Edition*, 2019, **58**, 7773-7777.
55. U. Achatz, C. Berg, S. Joos, B. S. Fox, M. K. Beyer, G. Niedner-Schatteburg and V. E. Bondybey, *Chemical Physics Letters*, 2000, **320**, 53-58.
56. H.-J. Werner, P. J. Knowles, G. Knizia, F. R. Manby and M. Schütz, *Wiley Interdisciplinary Reviews: Computational Molecular Science*, 2012, **2**, 242-253.
57. H. S. Yu, X. He, S. L. Li and D. G. Truhlar, *Chem Sci*, 2016, **7**, 5032-5051.
58. K. L. Schuchardt, B. T. Didier, T. Elsethagen, L. Sun, V. Gurumoorthi, J. Chase, J. Li and T. L. Windus, *Journal of Chemical Information and Modeling*, 2007, **47**, 1045-1052.
59. B. P. Pritchard, D. Altarawy, B. Didier, T. D. Gibson and T. L. Windus, *Journal of Chemical Information and Modeling*, 2019, **59**, 4814-4820.
60. D. Andrae, U. Haussermann, M. Dolg, H. Stoll and H. Preuss, *Theoretica Chimica Acta*, 1990, **77**, 123-141.
61. D. J. Pegg, *Reports on Progress in Physics*, 2004, **67**, 857-905.
62. R. J. Bartlett, J. D. Watts, S. A. Kucharski and J. Noga, *Chemical Physics Letters*, 1990, **165**, 513-522.
63. K. R. Shamasundar, G. Knizia and H.-J. Werner, *Journal of Chemical Physics*, 2011, **135**, 054101.
64. A. Berning, M. Schweizer, H.-J. Werner, P. J. Knowles and P. Palmieri, *Molecular Physics*, 2000, **98**, 1823-1833.
65. H.-J. Werner, P. J. Knowles, G. Knizia, F. R. Manby and M. Schütz, *WIREs Computational Molecular Science*, 2012, **2**, 242-253.
66. H. B. Gray and J. R. Winkler, *Accounts of Chemical Research*, 2018, **51**, 1850-1857.
67. Y. Shimoyama and T. Kojima, *Inorganic Chemistry*, 2019, **58**, 9517-9542.
68. *CRC Handbook of Chemistry and Physics, 93th ed; W. M. Haynes; CRC Press; 2012; Section 10, p 147.*
69. E. E. Claveau, S. Sader, B. A. Jackson, S. N. Khan and E. Miliordos, *Physical Chemistry Chemical Physics*, 2023, **25**, 5313-5326.
70. E. Andris, R. Navrátil, J. Jašík, M. Srnec, M. Rodríguez, M. Costas and J. Roithová, *Angewandte Chemie International Edition*, 2019, **58**, 9619-9624.
71. S. Mukerjee, K. Skogerson, S. DeGala and J. P. Caradonna, *Inorganica Chimica Acta*, 2000, **297**, 313-329.
72. K. Ray, F. Heims and F. F. Pfaff, *European Journal of Inorganic Chemistry*, 2013, **2013**, 3784-3807.
73. E. E. Claveau and E. Miliordos, *Physical Chemistry Chemical Physics*, 2019, **21**, 26324-26332.

74. A. Božović, S. Feil, G. K. Koyanagi, A. A. Viggiano, X. Zhang, M. Schlangen, H. Schwarz and D. K. Bohme, *Chemistry – A European Journal*, 2010, **16**, 11605-11610.
75. R. C. Bilodeau, M. Scheer, H. K. Haugen and R. L. Brooks, *Physical Review A*, 1999, **61**, 012505.
76. Y. Shiota and K. Yoshizawa, *Journal of the American Chemical Society*, 2000, **122**, 12317-12326.
77. J. Jang, K. Shen and C. G. Morales-Guio, *Joule*, 2019, **3**, 2589-2593.
78. S. J. Peppernick, K. D. D. Gunaratne and A. W. Castleman, *Proceedings of the National Academy of Sciences*, 2010, **107**, 975.
79. T. M. Ramond, G. E. Davico, F. Hellberg, F. Svedberg, P. Salén, P. Söderqvist and W. C. Lineberger, *Journal of Molecular Spectroscopy*, 2002, **216**, 1-14.
80. S. J. Peppernick, K. D. D. Gunaratne and A. W. Castleman, *Proc. Natl Acad. Sci.*, 2010, **107**, 975.
81. W. Rasheed, A. Draksharapu, S. Banerjee, V. G. Young Jr, R. Fan, Y. Guo, M. Ozerov, J. Nehr Korn, J. Krzystek, J. Telser and L. Que Jr, *Angewandte Chemie International Edition*, 2018, **57**, 9387-9391.
82. P.-O. Löwdin, *Physical Review*, 1955, **97**, 1474-1489.
83. E. Davidson, Science Direct, 1st Edition - January 28, 1976 edn., 1976, pp. 1-135.
84. N. M. S. Almeida, I. R. Ariyaratna and E. Miliordos, *Physical Chemistry Chemical Physics*, 2018, **20**, 14578-14586.
85. C. N. Sakellaris and A. Mavridis, *The Journal of Chemical Physics*, 2013, **138**, 054308.
86. M. Perera, R. B. Metz, O. Kostko and M. Ahmed, *Angewandte Chemie International Edition*, 2013, **52**, 888-891.
87. X.-G. Zhang, R. Liyanage and P. B. Armentrout, *Journal of the American Chemical Society*, 2001, **123**, 5563-5575.
88. S. Hoops, S. Sahle, R. Gauges, C. Lee, J. Pahle, N. Simus, M. Singhal, L. Xu, P. Mendes and U. Kummer, *Bioinformatics*, 2006, **22**, 3067-3074.
89. D. G. Leopold and W. C. Lineberger, *The Journal of Chemical Physics*, 1986, **85**, 51-55.
90. T. Andersen, K. R. Lykke, D. M. Neumark and W. C. Lineberger, *The Journal of Chemical Physics*, 1987, **86**, 1858-1867.
91. G. Drechsler, U. Boesl, C. Bälßmann and E. W. Schlag, *The Journal of Chemical Physics*, 1997, **107**, 2284-2291.
92. C. N. Sakellaris, E. Miliordos and A. Mavridis, *The Journal of Chemical Physics*, 2011, **134**, 234308.
93. A. Weller, *Angewandte Chemie International Edition*, 2015, **54**, 7747-7747.
94. H. S. Yu, X. He, S. L. Li and D. G. Truhlar, *Chemical Science*, 2016, **7**, 5032-5051.
95. T. H. Dunning, *Journal of Chemical Physics*, 1989, **90**, 1007-1023.
96. R. A. Kendall, T. H. Dunning and R. J. Harrison, *Journal of Chemical Physics*, 1992, **96**, 6796-6806.
97. N. B. Balabanov and K. A. Peterson, *Journal of Chemical Physics*, 2005, **123**, 064107.
98. D. Figgen, K. A. Peterson, M. Dolg and H. Stoll, *Journal of Chemical Physics*, 2009, **130**, 164108.
99. H.-J. Werner, P. J. Knowles, F. R. Manby, J. A. Black, K. Doll, A. Heßelmann, D. Kats, A. Köhn, T. Korona, D. A. Kreplin, Q. Ma, T. F. Miller, A. Mitrushchenkov, K. A. Peterson, I. Polyak, G. Rauhut and M. Sibaev, *Journal of Chemical Physics*, 2020, **152**, 144107.

100. D. Figgen, K. A. Peterson, M. Dolg and H. Stoll, *Journal of Chemical Physics*, 2009, **130**, 164108.
101. K. A. Peterson, D. Figgen, M. Dolg and H. Stoll, *The Journal of Chemical Physics*, 2007, **126**, 124101.
102. S. Sader and E. Miliordos, *Physical Chemistry Chemical Physics*, 2022, **24**, 21583-21587.
103. Z. J. Jain, P. S. Gide and R. S. Kankate, *Arabian Journal of Chemistry*, 2017, **10**, S2051-S2066.
104. C. N. Iverson and W. D. Jones, *Organometallics*, 2001, **20**, 5745-5750.
105. A. E. Kynman, S. Lau, S. O. Dowd, T. Krämer and A. B. Chaplin, *European Journal of Inorganic Chemistry*, 2020, **2020**, 3899-3906.
106. M. Zhu, Z. Chai, Z.-J. Lv, T. Li, W. Liu, J. Wei and W.-X. Zhang, *Journal of the American Chemical Society*, 2023, **145**, 6633-6638.
107. *CRC Handbook of Chemistry and Physics*, 97th ed; W. M. Haynes; CRC Press; 2016; Section 9, p 73.
108. E. D. B. Glendening, J. K.; Reed, A. E.; Carpenter, J. E.; Bohmann, J. A.; Morales, C. M.; Karafiloglou, P.; Landis, C. R.; Weinhold, F., *NBO 7.0. Theoretical Chemistry Institute: University of Wisconsin, Madison 2018*, <https://nbo6.chem.wisc.edu/>, accessed May 13, 2022.
109. E. D. Glendening, C. R. Landis and F. Weinhold, *Journal of Computational Chemistry*, 2019, **40**, 2234-2241.
110. M. J. Frisch, G. W. Trucks, H. B. Schlegel, G. E. Scuseria, M. A. Robb, J. R. Cheeseman, G. Scalmani, V. Barone, G. A. Petersson, H. Nakatsuji, X. Li, M. Caricato, A. V. Marenich, J. Bloino, B. G. Janesko, R. Gomperts, B. Mennucci, H. P. Hratchian, J. V. Ortiz, A. F. Izmaylov, J. L. Sonnenberg, Williams, F. Ding, F. Lipparini, F. Egidi, J. Goings, B. Peng, A. Petrone, T. Henderson, D. Ranasinghe, V. G. Zakrzewski, J. Gao, N. Rega, G. Zheng, W. Liang, M. Hada, M. Ehara, K. Toyota, R. Fukuda, J. Hasegawa, M. Ishida, T. Nakajima, Y. Honda, O. Kitao, H. Nakai, T. Vreven, K. Throssell, J. A. Montgomery Jr., J. E. Peralta, F. Ogliaro, M. J. Bearpark, J. J. Heyd, E. N. Brothers, K. N. Kudin, V. N. Staroverov, T. A. Keith, R. Kobayashi, J. Normand, K. Raghavachari, A. P. Rendell, J. C. Burant, S. S. Iyengar, J. Tomasi, M. Cossi, J. M. Millam, M. Klene, C. Adamo, R. Cammi, J. W. Ochterski, R. L. Martin, K. Morokuma, O. Farkas, J. B. Foresman and D. J. Fox, Wallingford, CT2016.
111. S. Kozuch, *WIREs Comput. Mol. Sci.*, 2012, **2**, 795-815.
112. J. A. Varela, S. A. Vázquez and E. Martínez-Núñez, *Chemical Science*, 2017, **8**, 3843-3851.
113. S. Kar, R. Sen, A. Goepfert and G. K. S. Prakash, *Journal of the American Chemical Society*, 2018, **140**, 1580-1583.
114. S. Kar, R. Sen, J. Kothandaraman, A. Goepfert, R. Chowdhury, S. B. Munoz, R. Haiges and G. K. S. Prakash, *Journal of the American Chemical Society*, 2019, **141**, 3160-3170.
115. J. Kothandaraman, A. Goepfert, M. Czaun, G. A. Olah and G. K. S. Prakash, *Journal of the American Chemical Society*, 2016, **138**, 778-781.
116. E. S. Sanz-Pérez, C. R. Murdock, S. A. Didas and C. W. Jones, *Chemical Reviews*, 2016, **116**, 11840-11876.
117. G. Liu, S. M. Ciborowski, Z. Zhu, Y. Chen, X. Zhang and K. H. Bowen, *Physical Chemistry Chemical Physics*, 2019, **21**, 10955-10960.

118. X. Zhang, E. Lim, S. K. Kim and K. H. Bowen, *Journal of Chemical Physics*, 2015, **143**, 174305.
119. X. Zhang, G. Liu, K.-H. Meiwes-Broer, G. Ganteför and K. Bowen, *Angewandte Chemie International Edition*, 2016, **55**, 9644-9647.
120. Y. Shi and K. M. Ervin, *Journal of Chemical Physics*, 1998, **108**, 1757-1760.
121. M. C. Thompson and J. M. Weber, *The Journal of Physical Chemistry A*, 2018, **122**, 3772-3779.
122. M. C. Thompson, J. Ramsay and J. M. Weber, *The Journal of Physical Chemistry A*, 2017, **121**, 7534-7542.
123. B. Yu and L. N. He, *Chemistry-Sustainability-energy-Materials*, 2015, **8**, 52-62.
124. M. Aresta and A. Dibenedetto, *Dalton Transactions*, 2007, 2975-2992.
125. Q. Liu, L. Wu, R. Jackstell and M. Beller, *Nature Communications*, 2015, **6**, 5933.
126. A. Behr and G. Henze, *Green Chemistry*, 2011, **13**, 25-39.
127. F. Julia-Hernandez, M. Gaydou, E. Serrano, M. van Gemmeren and R. Martin, *Topics Current Chemistry (Cham)*, 2016, **374**, 45.
128. L. Zhang and Z. M. Hou, *Current Opinion in Green and Sustainable Chemistry*, 2017, **3**, 17-21.
129. C.-X. Guo, B. Yu, R. Ma and L.-N. He, *Current Green Chemistry*, 2015, **2**, 14-25.
130. C. Bruneau and P. H. Dixneuf, *Journal of Molecular Catalysis*, 1992, **74**, 97-107.
131. Y. Sasaki, Y. Inoue and H. Hashimoto, *Journal of the Chemical Society-Chemical Communications*, 1976, 605-606.
132. F. Ferretti, M. Sharif, S. Dastgir, F. Ragaini, R. Jackstell and M. Beller, *Green Chemistry*, 2017, **19**, 3542-3548.
133. M. Liu, Y. Sun, Y. Liang and B. L. Lin, *ACS Macro Letters*, 2017, **6**, 1373-1378.
134. C. M. Williams, J. B. Johnson and T. Rovis, *Journal of the American Chemical Society*, 2008, **130**, 14936-14937.
135. H. Hoberg, S. Gross and A. Milchereit, *Angewandte Chemie International Edition in English*, 1987, **26**, 571-572.
136. K. Fukui, *Accounts of Chemical Research*, 1981, **14**, 363-368.
137. Y. Li, Z. Liu, R. Cheng and B. Liu, *ChemCatChem*, 2018, **10**, 1420-1430.

APPENDIX 1

Supporting Material for Chapter 2

Methane to Methanol Conversion Facilitated by Anionic Transition Metal Centers: The Case of Fe, Ni, Pd, and Pt

Safaa Sader and Evangelos Miliordos*



Cite This: *J. Phys. Chem. A* 2021, 125, 2364–2373



Read Online

ACCESS |

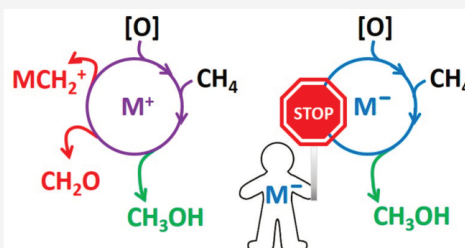
Metrics & More

Article Recommendations

Supporting Information

ABSTRACT: Density functional theory and high-level ab initio electronic structure calculations are performed to study the mechanism of the partial oxidation of methane to methanol facilitated by the titled anionic transition metal atoms. The energy landscape for the overall reaction $M^- + N_2O + CH_4 \rightarrow M^- + N_2 + CH_3OH$ ($M = Fe, Ni, Pd, Pt$) is constructed for different reaction pathways for all four metals. The comparison with earlier experimental and theoretical results for cationic centers demonstrates the better performance of the metal anions. The main advantage is that anionic centers interact weakly with the produced methanol. This fact facilitates the fast removal of methanol from the catalytic center and prevents the overoxidation of methane.

Moreover, a moderate or high energy barrier for the $M^- + CH_4 \rightarrow HMCH_3^-$ reaction step is observed, which protects the metal center from deactivation. Future work should focus on the identification of proper ligands, which stabilize the negative charge on the metal (electronic factors) and prevent the formation of the global CH_3MOH^- minimum (steric factors). Finally, a composite electronic structure method (combining size extensive coupled clusters approaches and accurate multireference configuration interaction) is proposed for computationally demanding systems and is applied to Fe^- .



INTRODUCTION

The ecological and economic impacts entailed by the growing global industrial activities have activated many efforts to develop a clean and sustainable source of energies as fossil fuel substitutes. One among the promising approaches is to trade in critically available fossil fuel with the methane to methanol (MTM) pathway. Methane is the main component of natural gas and can be readily produced from anthropogenic and nonanthropogenic resources, which makes it a superb candidate to supply several industrially valuable chemicals such as methanol. Additionally, MTM significantly contributes to both shielding the biosphere from the unsafe effect of methane's greenhouse and gas-flaring phenomena. Even more critically, the scientific and industrial importance of methanol put it within the forefront of produced chemicals worldwide with a foreseen market size of \$39 billion in 2025.^{1,2}

Industrially, CH_4 is transformed to methanol through an expensive and endothermic centralized procedure where natural gas is steamed and passed over a catalyst in a steam reformer producing syngas initially. The latter (a mixture of H_2 and CO) is passed over a catalyst producing methanol.³ At the laboratory level, several experimentalists have reported a single-step methanol synthesis using different transition metals (TM) through homogeneous and heterogeneous catalysis; however, the low conversion yield and uncontrolled selectivity hamper further development of these catalysts.^{13,16–22}

TM-based catalysts have a proven efficiency to activate the C–H bond with variable potentials.⁴ Recent studies for both heterogeneous and molecular systems demonstrated that any attempts to enhance methanol yield will be at the expense of catalyst selectivity.^{5,6} The high barriers required to activate methane, as well as the higher activity of the CH bonds in methanol compared to those in methane, deter the advancement of an efficient and selective catalyst.^{5,6} The indirect conversion process of Periana and co-workers bypassed this limitation,⁷ but the cost and recycling of agents has prevented any industrial applications.⁵ Norskov and co-workers suggested alternative strategies for the improvement of methanol yields, avoiding its overoxidation and preventing the catalyst poisoning due to the strong adsorption of methanol to the catalytic center.⁵ These include the use of collectors (chemical systems with strong methanol adsorption potential) or aqueous environments, both targeting the fast and efficient removal of methanol from the active sites.

Received: November 24, 2020

Revised: March 1, 2021

Published: March 12, 2021



ACS Publications

© 2021 American Chemical Society

2364

<https://dx.doi.org/10.1021/acs.jpca.0c10577>
J. Phys. Chem. A 2021, 125, 2364–2373

While the C–H activation including the MTM pathway has been widely explored previously using cationic and neutral forms of TMs in their atomic and oxide forms,^{4,5–11} the potential of negatively charged TM ions and anionic metal oxides in the MTM pathway is still poorly explored. Presently, we show that anionic systems reveal several advantages such as low oxidation energy barriers and weak adsorption of the produced methanol to the active sites. The latter effect can lead to short residence time and easy transport of methanol away from the catalytic site.

Fundamentally, both experimental and theoretical studies focus on the reaction of transition metal atoms or metal oxides with methane.^{12–15} Work published by Armentrout et al. shows that late first-row atomic TMs and third-row TMs favor dehydrogenation products ($\text{MCH}_2^+ + \text{H}_2$) over methane oxidation products ($\text{MH}^+ + \text{CH}_3$).^{12–19} Cationic metal oxides such as PtO^+ and FeO^+ yielded the same products as the bare cationic TMs.^{9,10,20} The nascent attempt to explore the role negatively charged TM atoms play in the MTM pathway was published by Msezane et al. in which anionic gold (Au^-) was theoretically studied using dispersion-corrected DFT.²¹ The major highlight of this work was the potential of Au^- to disrupt the C–H bond in CH_4 oxidation thereby avoiding CO_2 formation. In a different work, the authors extended their previous study to include atomic Y^- , Ru^- , At^- , In^- , Pd^- , Ag^- , Pt^- , and Os^- .²² Their energetics obtained mainly with density functional theory have shown that an anionic catalyst has a significant contribution of reducing the energy requirements for the MTM pathway, especially in stabilizing the transition states. The first systematic experimental investigation of the Pt^- potential in C–H activation belongs to Bowen et al.²³ Bowen's work demonstrated the selective activation of a single C–H bond and cast doubt on the previously accepted inadequacy of Pt^- in methane activation.²⁴ His work is the first experimental evidence of the Pt^- capability of activating the CH_4 molecule proven by mass spectroscopy data as well as computational study.²³

The present paper is part of our ongoing theoretical work on the MTM pathway^{25–28} and is grounded principally on the fact that weaker ion–dipole interaction between an anionic metal center and the formed product (CH_3OH), compared to the strong binding in cationic metal centers, facilitates the product release and avoids overoxidized products.⁵ On the other hand, finding high electron affinity (EA) metal centers is a challenging task but necessary to enable them to regain their electrons at the end of the cycle. To assess the role of the electron affinity, we selected the metals of group 10 (Ni, Pd, Pt) due to their relatively simple electronic structure (single-reference wave functions; see below), and they cover a wide EA range from 0.562 eV (Pd) to 1.156 eV (Ni) and 2.128 eV (Pt).²⁹ We also included in this work Fe as an example of an earth-abundant metal with an even lower EA (0.151 eV). The description of the electronic structure of iron compounds and the construction of the energy diagram for its catalytic cycle were proven substantially more demanding. Useful fundamental insights are deduced for future explorations on practical catalysts with adequate ligands that enhance the electron affinity (EA) of the metal center. The produced energy landscapes for the different metals are compared, and the efficiency of the corresponding catalytic cycles is assessed with the energetic span model.^{14,31}

METHODS

The optimal structures of all intermediates and transition states were obtained with Density Functional Theory (DFT). The MN15 functional³² is employed in this work combined with an aug-cc-pVTZ basis set for nonmetal atoms (O, C, H), Ni, and Fe.^{33–35} The 28 and 60 inner electrons of Pd and Pt are replaced with the Stuttgart relativistic pseudopotential, and the outer orbitals are constructed with the aug-cc-pVTZ-PP basis functions.^{36,37} The diffuse functions are necessary in these systems for the proper description of the negative charge. Harmonic vibrational frequencies are calculated for every structure to identify the nature of the located stationary structures. For all intermediates/transition states no/one imaginary frequency was obtained. The zero-point energies (ZPE) are also calculated with these frequencies. All of the optimized structures and frequencies are listed in the Supporting Information.

We further performed complete active space self-consistent field (CASSCF) single-point energy calculations for these structures to assess the multireference nature of the wave function. For Ni, Pd, and Pt, the doublet and quartet spin states are all of a high single-reference character. The dominant configuration has a coefficient of 0.85 or larger. For these systems, we further performed restricted coupled-cluster calculations with single, double, and perturbative triple electron replacements, RCCSD(T).^{38,39} Our recent work on the MTM conversion facilitated by FeCH_3^+ showed that RCCSD(T)/MN15 (RCCSD(T) energy at the MN15 optimized geometries) calculations are quite appropriate for systems of similar single-reference nature. Conversely, several quartet spin structures in the iron case reveal rich multireference character. For these structures we performed internally contracted multireference configuration interaction (MRCI)⁴⁰ calculations with single and double electron replacements of active electrons of the CASSCF wave function to the virtual orbital space. The RCCSD(T) energies of the sextet spin multiplicity and the MRCI quartet–sextet energy splitting are combined to provide a quasi-RCCSD(T) [qRCCSD(T)] energy for the quartet state as

$$E\left[\text{qRCCSD(T)}; S = \frac{3}{2}\right] = E\left[\text{RCCSD(T)}; S = \frac{5}{2}\right] + E\left[\text{MRCI}; S = \frac{3}{2}\right] - E\left[\text{MRCI}; S = \frac{5}{2}\right]$$

$E[X]$ is the total electronic energy. The validity of this approach lies in the single-reference nature of the high-spin $S = 5/2$ wave function (ferromagnetic coupling of the electronic spin). Information about the active space is provided in the relative sections in the Supporting Information (Tables S3 and S16a). The way we selected the active space is by eliminating from the complete valence space the molecular orbitals of bonds that are inactive during each specific reaction step. For example, we removed the σ and σ^* orbitals of the three CH bonds of methane that do not participate in any reaction.

Finally, the role of spin–orbit (SO) effects is studied for Pt compounds through the diagonalization of the Breit–Pauli Hamiltonian in the basis of their lowest energy CASSCF wave functions.⁴¹ The relative double- ζ basis sets are used, and the number of states employed is reported in the Supporting Information. The DFT/MN15 and RCCSD(T) calculations were carried out with Gaussian16.⁴² The CASSCF, MRCI, and SO calculations were done with MOLPRO 2015.^{43,44}

RESULTS AND DISCUSSION

The overall reaction and proposed main MTM cycle are shown in Figure 1. Initially, the metal center is oxidized by N_2O to

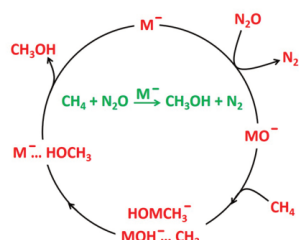


Figure 1. Studied catalytic cycle for the MTM conversion. M is the metal center catalyzing the reaction of CH_4 with N_2O . The two bottom structures are the two possible products of the $MO^- + CH_4$ reaction step.

form a metal oxide anionic unit. Subsequently, methane reacts with MO^- and forms either $HOMCH_3^-$ (2 + 2 addition) or MOH^- interacting with a methyl radical, $MOH^- \cdots CH_3$ (hydrogen abstraction). The former implies the heterolytic dissociation of the CH bond and the latter a homolytic one.⁴⁵ Finally, the CH_3 and OH moieties attach together to make methanol, and the negative charge returns to the metal center. The chemical equations for the three reaction steps are



The $[CH_3, MOH]^-$ notation in eqs 2 and 3 represents the CH_3MOH^- and $MOH^- \cdots CH_3$ structures.

The weaker charge–dipole interaction of the formed $M^- \cdots HOCH_3$ compared to that of methanol to a cationic metal center grants anionic centers the advantage of minimizing the methanol residence time at the catalytic site, thus eschewing methanol overoxidation and facilitating methanol removal. In addition, we show below that the oxidation step has small (nearly minimal) activation energy barriers for anionic centers. The electron affinities of CH_4 , N_2O , and CH_3OH are small or negative (anions are not stable), and thus the return of the electron to the metal is guaranteed in this case. For practical applications special attention must be given to avoid molecules with larger electron affinities. Alternatively, ligands which increase the electron affinity of the metal center must be employed. Our present goal is to reveal the advantages of anionic centers and study the effect of the EA of the metal center on the energetics of the catalytic cycle.

We start our discussion with Pt^- , which has the largest EA and has been used in the past to activate methane experimentally.²³ We then move in decreasing EA order going to Ni, Pd, and Fe. The located MN15 intermediate structures (IS) and transition states (TS) for the catalytic cycle of Figure 1 are depicted in Figure 2. The reactants and products of eqs 1–3 are enclosed in orange boxes. The two $[CH_3, PtOH]^-$ structures, IS_4 ($PtOH^- \cdots CH_3$) and IS_5 (CH_3PtOH^-), are enclosed in boxes with dashed lines.

The first reaction step occurs through two possible mechanisms, the single-step mechanism via TS_2 and the

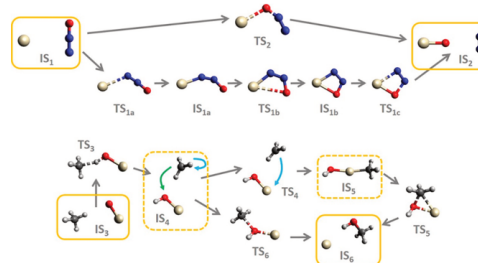


Figure 2. MN15 intermediate structures (IS) and transition states (TS) for the reactions steps 1–3 with $M = Pt$. The upper part corresponds to the two possible mechanisms for step 1 connecting IS_1 and IS_2 . The lower part relates to steps 2 and 3. Step 2 goes from IS_3 to either IS_4 or IS_5 , and step 3 completes the cycle via TS_5 and TS_6 and forms IS_6 .

multistep one via TS_{1a} , IS_{1a} , TS_{1b} , IS_{1b} , and TS_{1c} . TS_2 allows the direct transfer of the oxygen atom from N_2O to Pt^- . Along the second path, N_2O anchors first to Pt^- with its nitrogen terminus, oxygen then binds also to Pt^- making a $PtNNO$ ring, and finally N_2 is released. The ground states of both Pt^- and PtO^- (reactant and product) have been identified experimentally as doublet states (2D and $^2\Pi$)^{46,47} in agreement with our present calculations. Furthermore, our CASSCF calculations showed that the ground state spin multiplicity and single-reference character (one unpaired electron) are preserved across all of the structures of the two mechanisms. Therefore, the RCCSD(T) numerical results should be considered quite accurate.

The MN15 and RCCSD(T) energy landscape for the two mechanisms is given in Figure 3. The contribution of the ZPE

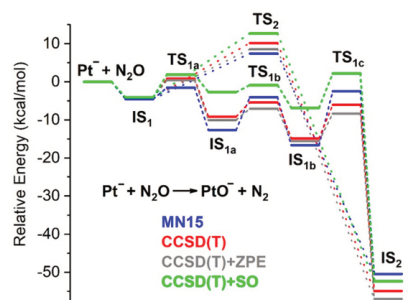


Figure 3. Energy diagram for the oxidation step of the metal center (eq 1) for different methodologies: DFT/MN15 (blue lines), RCCSD(T) (red lines), ZPE-corrected RCCSD(T) (gray lines), spin-orbit-corrected RCCSD(T) (green lines). See Figure 2 for the notation of all IS and TS structures.

(at MN15) and SO (at CASSCF) effects is also considered. All methods predict that the multistep mechanism is more favorable. According to the MN15 and RCCSD(T) energetics, the oxidation of Pt^- is highly exothermic, and the energy of the IS and TS structures for the multistep is below the energy of the reactants ($Pt^- + N_2O$). The transition state for the single-step mechanism (TS_2) lies higher in energy than the reactants

by at least 7.4 kcal/mol (MN15). The largest energy difference of 3.5 kcal/mol between MN15 and RCCSD(T) belongs to TS_{1c} . The rather small discrepancies between RCCSD(T) and MN15 validate the use of the MN15 functional. As expected the ZPE corrections lower the activation barriers by no more than 2.5 kcal/mol ($IS_{1b} \rightarrow TS_{1c}$). On the other hand, the contribution of the SO effects can be substantial and important for accurate energetics. Generally, SO effects stabilize the initial reactants over the rest of the IS and TS structures due to the large spin-orbit splitting of Pt^+ , which experimentally is 9740.9 cm^{-1} .⁴⁸ The largest discrepancy is seen for IS_{1b} (9.0 kcal/mol). However, the reaction remains highly exothermic, and the multistep mechanism is still the most favorable path with low activation energy barriers; see Figure 3.

The produced IS_2 delivers N_2 and attracts a methane molecule to form IS_3 . The oxygen terminus of the PtO^- unit abstracts a hydrogen atom from methane via TS_3 (see Figure 2). The produced $PtOH \cdots CH_3$ interacting complex (IS_4) is very unstable, and a slight rotation of the methyl radical (see the blue curved arrow at IS_4 in Figure 2) leads to the formation of the very stable $HOPtCH_3^-$ (IS_5) via TS_4 . Alternatively, IS_4 can go through TS_6 (methyl radical attacks oxygen; see the green arrow at IS_4 in Figure 2) to make the final product $Pt^+ \cdots HOCH_3$, which is also formed from IS_5 via TS_5 .

Figure 4 gives the energy diagram for the conversion of methane to methanol (reactions 2 and 3). The doublet spin

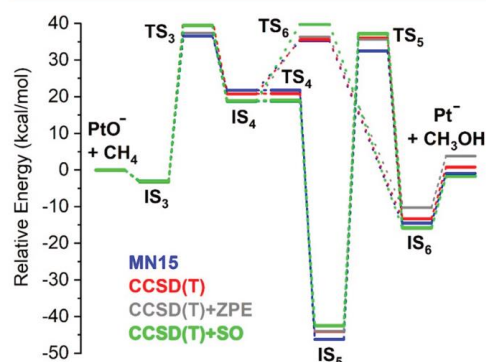


Figure 4. Energy diagram for the methane functionalization steps (eqs 2 and 3) for different methodologies: DFT/MN15 (blue lines), RCCSD(T) (red lines), ZPE-corrected RCCSD(T) (gray lines), and spin-orbit-corrected RCCSD(T) (green lines). See Figure 2 for the notation of all IS and TS structures. See Figure S2 of the Supporting Information for the same plot but shifted so that the zero of the energy corresponds to $Pt^+ + N_2O + CH_4$.

multiplicity still provides the lowest energy states for all intermediates and transition states. The hydrogen abstraction energy barrier is approximately 40 kcal/mol independently of the method employed. The conversion of the formed IS_4 to IS_5 is practically barrier-free with a minimal activation barrier of ~ 0.1 kcal/mol (TS_4). IS_5 is the global minimum of the energy landscape and needs to overcome a barrier of 80 kcal/mol in order to form the final IS_6 structure, which is 25–30 kcal/mol higher in energy. Alternatively, IS_4 can go directly to IS_6 after a small activation energy barrier of nearly 20 kcal/mol. The release of methanol from IS_6 takes about 15 kcal/mol. In this

case, the energy range due to the different methods is no more than 5.5 kcal/mol, including spin-orbit effects.

For an efficient catalytic path, the C–H activation energy barrier should decrease by about 15 kcal/mol, and the formation of IS_5 should be avoided. Both of these bottlenecks can be bypassed by adding proper ligands. The necessary space for the formation of IS_5 can be restricted by completing the first coordination sphere of the metal, as happens for positively charged fully coordinated metal-oxide complexes.⁴⁹

To get a deeper understanding of the mechanism, we focus on the underlying electronic structure variations for the intermediate structures. Figure 5 shows the involved π

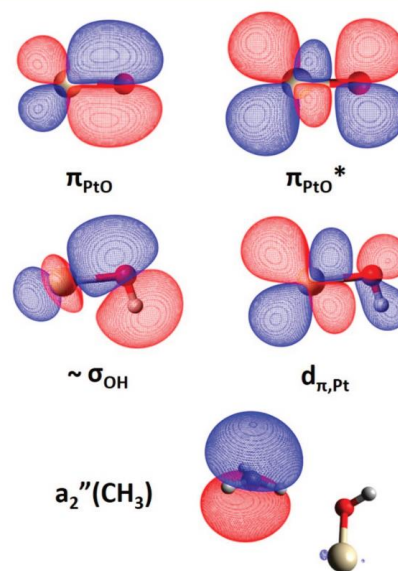


Figure 5. Molecular orbital contours of PtO^- (top), $PtOH^-$ (middle), and $CH_3 \cdots PtOH^-$ (bottom) involved in the C–H activation process.

molecular orbitals of PtO^- . The only singly occupied orbital of the system is one of the two π_{PtO^*} orbitals. The other one, along with the two π_{PtO} orbitals, is doubly occupied. The valence space of PtO^- consists further of the following doubly occupied orbitals: a σ_{PtO} bonding molecular orbital, the $\sim 2s_O$, two d_{Pt} , and one σ_{Pt} orbital, which has $4s_{Pt}$ character (see ref 50 for the similar orbitals of PdO^-). When CH_4 reacts with PtO^- , the closed-shell $PtOH^-$ is produced along with a methyl radical. The singly occupied orbital of CH_3 is shown in Figure 5 (a_2''). Based on the orbitals of $PtOH^-$ (see Figure 5), we notice that the hydrogen atom binds to PtO^- as follows: the π_{PtO} electrons “attack” H^+ (Lewis acid/base binding; see π_{PtO}/σ_{OH} orbitals of Figure 5), and the unpaired electron of H couples with the unpaired electron in the π_{PtO^*} orbital (see the $\pi_{PtO^*}/d_{\pi,Pt}$ orbitals of Figure 5), which shifts toward the platinum end. Overall, the process can be seen as a kind of proton-coupled electron transfer (PCET). To further support this observation, we plotted the RCCSD(T)/MN15 activation energy barrier against the proton affinity for the three metal oxides (NiO^- , PdO^- , PtO^-) or the acidity of the

metal hydroxides ξ at their doublet spin electronic state as $\xi = E[\text{MO}^-] + E[\text{H}^+] - E[\text{MOH}]$. Indeed, we found that a larger ξ (381.4, 386.4, 352.8 kcal/mol) corresponds to smaller activation energy barriers (30.9, 21.7, 44.3 kcal/mol), which suggests that ξ can be a good descriptor for future theoretical investigations.

Finally, we would like to emphasize the differences between metal oxide cations and anions. The $\text{MO}^+ + \text{CH}_4$ reaction in the gas phase has been studied experimentally for $M = \text{Ni}$, Pd , and Pt .⁵¹ Three different production channels were observed: $\text{M}^+ + \text{CH}_3\text{OH}$, $\text{MCH}_2^+ + \text{H}_2\text{O}$, and $\text{MOCH}_2^+ + \text{H}_2$ ($M = \text{Pd}$) or $\text{MH}_2^+ + \text{OCH}_2$ ($M = \text{Pt}$). The relative energies for the three type of products and for the three metals are listed in Table 1.

Table 1. MN15/aug-cc-pVTZ^a Relative Energies (kcal/mol) and Experimental Yields (Gas-Phase Reactions at Room Temperature) in Parentheses of Different Products of the $\text{NiO}^+/\text{PdO}^+/\text{PdO}^-/\text{PtO}^+/\text{PtO}^- + \text{CH}_4$ Reaction^b

products	M = Ni ⁺	M = Pd ⁺	M = Pd ⁻	M = Pt ⁺	M = Pt ⁻
M + CH ₃ OH	17.7 (100%)	15.1 (78%)	0.0	36.9 (0%)	0.1
MCH ₂ + H ₂ O	39.8 (0%)	22.3 (0%)	14.0	0.0 (98%)	0.0
MOCH ₂ + H ₂	0.0 (0%)	0.0 (15%)	31.5	9.3 ^d (2%)	33.8

^aThe aug-cc-pVTZ-PP basis set is used for Pt and Pd (see the Methods section). ^bExact electronic energies are given in the Supporting Information. ^c7% for Pd was unreactive collected as a $\text{PdO}^+(\text{CH}_4)$ complex. ^dPt produced $\text{PtH}_2^+ + \text{CH}_2\text{O}$.

For Ni and Pd our numerical results differ substantially (20–30 kcal/mol in some cases) from those of ref 51, but the relative energies of the different products is always consistent. No energetics for platinum are reported in ref 51. Table 1 lists also the experimental yields for all three metals. Notice that although $\text{MOCH}_2^+ + \text{H}_2$ for $M = \text{Ni}$ and Pd has the lowest energy products, the main products of the reaction are $\text{M}^+ + \text{CH}_3\text{OH}$ due to the large activation barriers for the oxidation of methanol to formaldehyde (CH_2O) on the M^+ center.⁵¹ On the other hand, PtO^+ facilitates the production of the lowest energy $\text{PtCH}_2^+ + \text{H}_2\text{O}$ products with 98% yield (see Table 1). PtO^+ turns out to be a very poor mediator for the selective oxidation of methane to methanol (0% yield; see Table 1). The methanol production channel is 36.9 kcal/mol higher than $\text{PtCH}_2^+ + \text{H}_2\text{O}$. On the other hand, using PtO^- the two channels $\text{PtCH}_2^- + \text{H}_2\text{O}$ and $\text{Pt}^- + \text{CH}_3\text{OH}$ become nearly isoenergetic (see Table 1), and the inclusion of spin–orbit effects is expected to stabilize the latter over the former channel, due to the large spin–orbit splitting for Pt^- .⁴⁸ Conclusively, it is expected that PtO^- will provide high methanol yields and that metal anions demonstrate higher selectivity to methanol production over other channels. The same is found for PdO^- , where the methanol channel is clearly more stable than the other two, as opposed to PdO^+ , where $\text{PdOCH}_2^+ + \text{H}_2$ products are the most stable ones.

Another worthwhile difference is the energy required for the release of methanol from the metal center. Our MN15 calculations predict an energy difference between $\text{Pt}^+ + \text{CH}_3\text{OH}$ and the produced $\text{Pt}^+(\text{CH}_3\text{OH})$ adduct of 60.3 kcal/mol, and it is higher than the upper limit of the range calculated theoretically (DFT/B3LYP) for the first-row transition metals (31.0–56.8 kcal/mol).⁵² The detachment

energy of methanol from Pt^- is only 13.6 kcal/mol, more than four times smaller than that from Pt^+ . On the other hand, the C–H activation energy barrier for PtO^- is relatively high (39.6 kcal/mol), and certainly higher than the 9.4–34.4 kcal/mol range (DFT/B3LYP) for first-row transition metal oxide cations.⁵² Overall, the selectivity of PtO^- is predicted to be higher than that of PtO^+ , but the activation of the C–H bond is less efficient. The wise choice of ligands is expected to reduce the activation barrier and maintain a higher selectivity for the anionic catalytic center.

We now turn our attention to the Ni and Pd metals in order to see the effect of the metal identity. The energy diagrams for the oxidation of the metal centers with N_2O are plotted in Figure 6. For comparison, we also include Pt in Figure 6. For

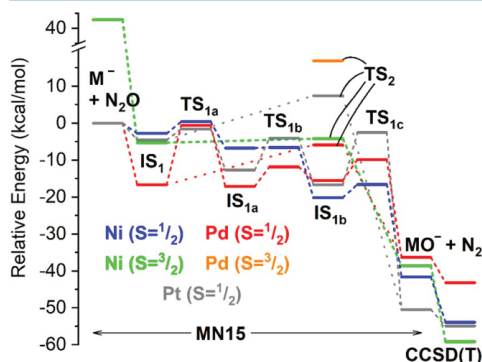


Figure 6. MN15 energy diagram for the oxidation of Ni^- , Pd^- , and Pt^- to NiO^- , PdO^- , and PtO^- by N_2O . Blue and green lines correspond to Ni with doublet and quartet spin multiplicity, respectively, red and purple to Pd with doublet and quartet spin, and gray to Pt (doublet spin). The RCCSD(T) energies of the final products $\text{MO}^- + \text{N}_2$ ($M = \text{Ni}$, Pd , Pt) are also shown at the right end of the plot.

Ni and Pd we included the path of the lowest quartet spin state as well. The ground state of all three metal oxide anions has been characterized experimentally as $^2\Pi$.⁴⁶ Our present calculations on PtO^- and our recent calculations on PdO^- confirm a doublet ground state for these systems.⁵⁰ The ground state of NiO^- is predicted as $^2\Pi$ at MN15 but as a $^4\Sigma^-$ at RCCSD(T), which guided us to consider the full quartet reaction pathway for Ni (see below).

The earlier high-level theoretical work of Sakellaris and Mavridis expressed concerns about the ground state of NiO^- seven years ago.⁵³ They found a $^4\Sigma^-$ ground state at the MRCI level but a $^2\Pi$ at RCCSD(T). The rich multireference character of $^2\Pi$ (their coefficient for the dominant configuration is only 0.44) led them to express hesitations about their RCCSD(T) results and propose a $^4\Sigma^-$ ground state. We repeated the calculations at the exact same level of theory, and we found a smaller multireference character (largest coefficient is 0.62, and the next one is -0.32). In addition, our RCCSD(T) calculations point to a $^4\Sigma^-$ ground state in harmony with the MRCI calculations of Sakellaris and Mavridis but in disagreement with their RCCSD(T) results. Our RCCSD(T)/aug-cc-pv5Z energy for the $^2\Pi$ is in absolute agreement with their energy (-1582.44192 au), but our

RCCSD(T)/aug-cc-pV5Z energy for $^4\Sigma^-$ is 10^{-2} au lower than theirs (-1582.44321 vs -1582.43324 au). A similar difference is found at the C-RCCSD(T) level (=RCCSD(T) where the $3s^23p^6$ electrons of Ni are also correlated) (-1582.92327 vs -1582.91407 au). We believe that the RCCSD(T) energies of Sakellaris and Mavridis correspond to a higher energy $^4\Sigma^-$ state and that the ground state of NiO^- is $^4\Sigma^-$, as indicated by the previous MRCI and present RCCSD(T) calculations.

In any case, we considered both spin multiplicities for the case of Ni, which revealed an additional oxidation mechanism facilitated by the excited state of Ni^- ($^4G; 4s^23d^84p^1$). This state of Ni^- lies above the ground state of Ni, but the NiON_2 complex with $S = 3/2$ is actually lower than that with $S = 1/2$ and reacts in an almost barrier-free mode to produce NiO^- ($^4\Sigma^-$), which is an excited state at MN15 but the ground state at RCCSD(T); see Figure 6. The reaction mechanism for the $S = 3/2$ pathway is a one-step mechanism running through TS_2 (see Figure 2). The Ni + N_2O reaction (following the three-step mechanism of Figure 2) bears minimal activation barriers of less than 5 kcal/mol along the $S = 1/2$ as well. The $S = 3/2$ pathway for Pd bears a large activation energy barrier, and we were not able to locate this transition state for Pt. Therefore, both Pt and Pd stay on the $S = 1/2$ potential energy hypersurface. However, Pd (as opposed to Pt) prefers the one-step mechanism for $S = 1/2$ since TS_2 has lower energy than TS_{1a} (see Figures 2 and 6). The activation energy barrier for Pd is 10.7 kcal/mol ($\text{TS}_{1c} - \text{IS}_1$ energy difference). Conclusively, the oxidation of any of the three metal anions is quite facile (independently of the mechanism) with small activation barriers and highly exothermic: Pd oxidation is less exothermic than Pt, which is less exothermic than Ni.

The energy landscape for the $\text{MO}^- + \text{CH}_4$ reaction ($M = \text{Ni}, \text{Pd}, \text{Pt}$) is shown in Figure 7. We used RCCSD(T)/MN15 energies to make sure that we describe the energy of the doublet and quartet states of NiO^- accurately. We were not able to locate the TS_4 structure connecting IS_4 and IS_5 for Ni and Pd. Based on the Pt results, we believe that IS_4 is nearly a

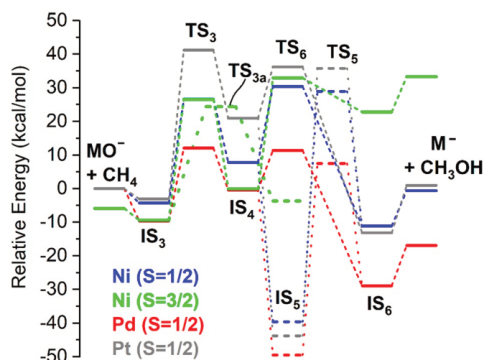


Figure 7. RCCSD(T)/MN15 energy diagram for the $\text{MO}^- + \text{CH}_4 \rightarrow \text{M}^- + \text{CH}_3\text{OH}$ reaction ($M = \text{Ni}, \text{Pd}, \text{Pt}$). Solid lines correspond to the hydrogen abstraction mechanism and dashed horizontal lines to the 2 + 2 mechanism. Blue/green colors correspond to doublet/quartet paths of Ni and red/gray to the doublet paths of Pd/Pt. See Figure S3 of the Supporting Information for the same plot but shifted so that the zero of the energy corresponds to $\text{M}^- + \text{N}_2\text{O} + \text{CH}_4$.

shoulder in the potential energy surface and that IS_4 “slides” to IS_5 with a minimal (nearly nonexistent) energy barrier. Therefore, TS_4 is not included in Figure 7. Pd and Pt paths remain always in their doublet spin state, as opposed to Ni, which starts from $\text{NiO}^- + \text{CH}_4$ ($S = 3/2$) and terminates to $\text{Ni}^- + \text{CH}_3\text{OH}$ ($S = 1/2$). Both spin multiplicities are included in Figure 7 for both mechanisms of Figure 2 (radical and 2 + 2). The zero energy for this plot is set to the energy of $\text{MO}^- + \text{CH}_4 + \text{N}_2$ for simplicity and easier comparison of the three metals, but all of the energy diagrams are well below the energy of the initial reactants $\text{M}^- + \text{CH}_4 + \text{N}_2\text{O}$ (zero of previous plots) indicating an overall highly exothermic cycle (see also Figure 8).

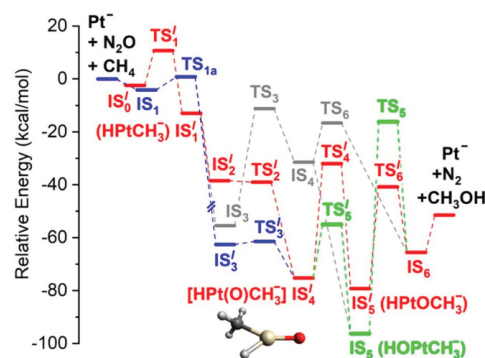


Figure 8. RCCSD(T)/MN15 energy diagrams for several pathways of the $\text{Pt}^- + \text{CH}_4 + \text{N}_2\text{O} \rightarrow \text{Pt}^- + \text{CH}_3\text{OH} + \text{N}_2$ reaction (see text).

The $\text{MO}^- + \text{CH}_4$ reaction is clearly exothermic only for Pd. The energy of the products is equal (within 1 kcal/mol) to that of the reactants for Pt and Ni. Of course, the overall $\text{N}_2\text{O} + \text{CH}_4 \rightarrow \text{N}_2 + \text{CH}_3\text{OH}$ reaction is exothermic and can drive the $\text{MO}^- + \text{CH}_4$ part. Pd offers the lowest energy activation barriers, while Pt has the largest ones. Focusing only on the radical mechanism (solid red lines in Figure 7), the activation energy barriers for Pd are 22 and 12 kcal/mol, indicating a viable route, as opposed to the twice or thrice larger barriers for Pt and Ni (see Figure 7). To provide a more quantitative argument, we employed the energetic span model^{30,31} for the 2 + 2 and radical mechanisms independently and for each metal. The turnover frequency (TOF) determining the transition state (TDTS) and intermediate (TDI) are TS_5 and IS_5 for the 2 + 2 mechanism and TS_3/IS_3 for the radical mechanism of all three metals. The apparent activation energies (TDTS – TDI energy differences) are always larger than 34 kcal/mol, except for the 21.7 kcal/mol palladium radical mechanism. The obtained TOFs are marginal for all cases except for the radical mechanism in Pd, for which $\text{TOF}(25^\circ\text{C}) = 3 \text{ h}^{-1}$; $\text{TOF}(50^\circ\text{C}) = 54 \text{ h}^{-1}$; $\text{TOF}(100^\circ\text{C}) = 5722 \text{ h}^{-1}$. The very stable CH_3MOH^- intermediate with respect to the final products (by at least 33 kcal/mol in the Pd case) of the 2 + 2 mechanism is the global minimum of the multidimension energy surface and responsible for the low TOF numbers. The addition of ligands is necessary to limit the available coordination space and eliminate the presence of CH_3MOH^- .

As shown in Figures 6 and 7, Ni has a competitive quartet spin channel, which is lower in energy at the early stages of the

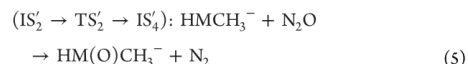
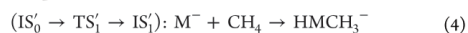
$\text{MO}^- + \text{CH}_4$ reaction, but gives its place to the doublet for both mechanisms to finally release a doublet M^- . Specifically, the switch happens between IS_4 and TS_6 for the radical mechanism and between TS_{3a} and IS_5 for the $2 + 2$ route. TS_{3a} is the transition state connecting directly $\text{MO}^- + \text{CH}_4$ and CH_3MOH^- (see the Supporting Information).

Conclusively, Pd provides the most promising energy diagram but has the smallest electron affinity. Larger electron affinity can ensure further the return of the negative charge to the metal at the end of the catalytic cycle. Therefore, the addition of ligands should target the elimination of IS_5 and the increase of the electron affinity of the catalyst. It should also be mentioned that the energy to release methanol from the metal anion is in the 10–14 kcal/mol range, nearly independent of the metal identity.

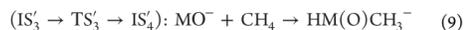
In the case of Pt, we identified additional reaction pathways.⁵⁴ So far, we considered the oxidation step happening first and followed by the C–H bond activation mediated by the terminal oxygen atom (gray energy diagram in Figure 8). Other options include the activation of the C–H bond by the metal center (and not the oxygen terminus) initially or after its oxidation. The energy plots for these paths are included in Figure 8, and the corresponding structures, energies, and frequencies are given in the Supporting Information.

Specifically, the red path pertains to the activation of the C–H bond first by Pt^- , followed by the oxidation of the metal center forming $\text{HM}(\text{O})\text{CH}_3^-$, where all three active units (H, CH_3 , O) are attached to the metal (see inset for IS'_4 of Figure 8). The recombination of these fragments to form methanol has two alternatives with either CH_3 (red path) or H (green path) migrating first to oxygen. The blue path runs through IS'_4 too, but the C–H bond splits after the oxidation of the metal center ($\text{IS}'_5 \rightarrow \text{TS}'_5$). The reaction network of Figure 8 for a metal M (here $\text{M} = \text{Pt}$) is summarized by the ensuing chemical equations (gray path corresponds to eqs 1 + 2 + 3).

Red path:



Blue path:



Green path:



The second step for the formation of IS'_4 is nearly barrier-free independently of the path followed: 4 + 5 or 8 + 9; see TS'_2 and TS'_3 . Notice that the energy of TS'_2 is lower than that of the corresponding reactants (IS'_2) at RCCSD(T)//MN15 (Figure 8), but it is higher at MN15 where the fully optimized structures are used. Another observation is that the activation of the C–H bond from the metal, reaction 4 and TS'_1 , bears an energy barrier of only 12.3 kcal/mol as opposed to 44.3 kcal/

mol when oxygen is mediated, reaction 2. The activation barrier for reaction 4 becomes 15.3 and 33.0 kcal/mol for Pd and Ni and for reaction 2 is 21.7 and 30.8 kcal/mol, respectively. These numbers suggest that Pd can activate the C–H more easily from either site (metal or oxygen).

Another point of caution is that the oxidation of the metal must precede the insertion of CH_4 to the metal center for practical applications to avoid blocking the catalytic center from the insertion of oxygen. Metal anions are advantageous because reaction 4 requires some activation energy barrier, as opposed to neutral and cationic metal centers. For example, experimental/theoretical combined studies on the reactions of Pt and Pt^+ with CH_4 showed that Pt goes to HPTCH_3 through a barrier-free path,⁵⁵ while Pt^+ bears a minimal barrier of ~ 2.5 kcal/mol.⁵⁶

After IS'_4 is formed, the reaction barriers for the OH or OCH_3 formation are 20.3 and 43.2 kcal/mol, and the final attachments of CH_3 or H to produce methanol are 80.1 and 38.5 kcal/mol (reactions 6 + 7 or 10 + 11). Both paths have overall higher activation barriers from the 1–3 gray path (44.3 and 14.8 kcal/mol). However, the rapid formation of IS'_5 and IS'_6 can poison the catalyst. This effect will be eliminated when the ligands are coordinated.

Finally, we examined the reaction pathway of Figure 1 for the most earth-abundant transition metal element, iron. Given that the lowest-EA metal among Ni, Pd, and Pt performs better and considering some connection between EA and catalytic performance, iron can be thought of as an even better candidate due to its small EA value. The calculations for iron turned out very challenging, and the use of a composite method combining MRCI and RCCSD(T) was deemed necessary (qRCCSD(T); see the Methods section). Even the accurate calculation of the EA for a single iron atom necessitates the use of large basis sets and highly correlated methods. Iron has an experimental EA of 0.151 ± 0.003 eV.⁵⁷ Our MN15/aug-cc-pVTZ value overestimates the EA significantly (0.76 eV), while RCCSD(T)/aug-cc-pVTZ predicts an unstable anion ($\text{EA} = -0.07$ eV). Increasing the basis set to aug-cc-pVSZ RCCSD(T) provides a more reasonable value of 0.05 eV, which is still one-third of the experimental value.

On the other hand, the EA of FeO can be obtained easily. The RCCSD(T)/aug-cc-pVTZ and MN15/aug-cc-pVTZ values of 1.469 and 1.467 eV are in remarkable agreement with the experimental value of 1.494 ± 0.010 eV.^{58,59} The electronic structure of FeO^- has been studied meticulously in the past.⁶⁰ There are three competing states ($6\Sigma^+$, 6Δ , and 4Δ) lying within less than 2000 cm^{-1} at MRCl, and their order is sensitive to the electron correlation treatment, subvalence electron correlation, and relativistic effects. Experimentally, the ground state has been identified as $X^4\Delta_{7/2}$. MN15 predicts a 4Δ ground state with the first sextet state ($6\Sigma^+$) being 0.15 eV higher. But RCCSD(T)/aug-cc-pVTZ predicts a completely reverse order; the ground state is a $6\Sigma^+$, and the first quartet state (4Δ) is 0.15 eV higher. This difference drops to 0.07 eV when aug-cc-pVSZ is used. The 6Δ lies in between them: 0.08 and 0.02 eV at the RCCSD(T)/aug-cc-pVTZ and RCCSD(T)/aug-cc-pVSZ levels of theory. The situation becomes even more complex considering that the interaction of FeO^- with methane brings these three states even closer. Presently, we decided to use the same approaches (MN15 and RCCSD(T)//MN15 with an augmented triple- ζ basis set) as in the Ni, Pd, and Pt species for fair comparisons. Our results do not provide accurate relative energetics between the sextet and

quartet spin pathways, which are practically degenerate in most cases.

The MN15 and RCCSD(T)//MN15 results are in good agreement for the high-spin case ($S = 5/2$) but differ considerably for the quartet spin multiplicity ($S = 3/2$). Specifically, the MN15 energy diagram for $S = 5/2$ is parallel (within ± 7 kcal/mol) to the RCCSD(T)//MN15 one but separated by about 0.7 eV, which corresponds to the difference of the quartet–sextet (${}^4F; 4s^2 3d^7 / {}^6F; 4s^2 3d^6 4p^1$) energy splitting for Fe^- between MN15 and RCCSD(T). Complete energy diagrams for all methods and both spins are provided in the Supporting Information. On the contrary, the $S = 3/2$ MN15 and RCCSD(T) energy landscapes are closer to each other, but there are structures differing by about 20 kcal/mol. One such structure is $\text{FeOH}^- \cdots \text{CH}_3$, where the $S = 3/2$ is a result of antiferromagnetic coupling between the $S = 2$ state of FeOH^- and the ${}^2A'_2$ state of CH_3 . The spin contamination is dramatic (larger than 1.0) and suggests the use of multireference approaches in this case. To combine the size-extensivity benefit of RCCSD(T) and the proper description of the quartet state at the MRCI, we used the qRCCSD(T) approach described in the Methods section. The RCCSD(T)//MN15 energies are used for the sextet path and the qRCCSD(T)//MN15 energies for the quartet path for all structures. More details, such as CI vectors and MRCI and RCCSD(T) energies, are listed in the Supporting Information file.

Figure 9 includes the reaction energetics for steps 1–3 with $M = \text{Fe}$. In this case, we were able to identify transition states

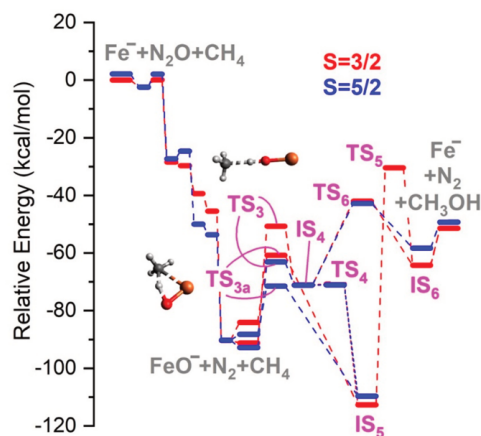


Figure 9. RCCSD(T)//MN15 ($S = 5/2$) and qRCCSD(T)//MN15 ($S = 3/2$) energy diagrams for the radical and 2 + 2 mechanisms of the $\text{Fe}^- + \text{CH}_4 + \text{N}_2\text{O} \rightarrow \text{Fe}^- + \text{CH}_3\text{OH} + \text{N}_2$ reaction.

for both the radical (hydrogen abstraction; TS_3) and 2 + 2 (proton abstraction; TS_{3a}) mechanisms for both the low- and high-spin cases. These structures for the sextet state are shown as insets in Figure 9. A first comparison with Figures 6 and 7 reveals that oxidation of the metal center remains facile and highly exothermic. Therefore, future studies can focus on the reaction of the metal oxide with methane. Another observation is that the $\text{FeO}^- + \text{CH}_4$ reaction is highly endothermic, as opposed to Ni, Pt, or Pd, which are either thermoneutral or

exothermic. This is result of the stronger FeO bond, and therefore the metal–oxygen binding energy can be used as an initial criterion for screening efficient catalysts. The metal–oxygen bond should be small enough so that the $\text{MO}^- + \text{N}_2 + \text{CH}_4$ asymptote is higher than that of $\text{M}^- + \text{N}_2 + \text{CH}_3\text{OH}$, or $D_c[\text{MO}^-] = E[\text{M}^-] + E[\text{O}] - E[\text{MO}^-] \leq E[\text{CH}_4] + E[\text{O}] - E[\text{CH}_3\text{OH}] = 95.6$ kcal/mol.

The quartet and sextet pathways are nearly parallel and cross each other at different steps (see Figure 9). The most striking difference is the initial activation of the C–H bond. The sextet spin multiplicity provides clearly lower energy barriers, especially for the 2 + 2 mechanism. Specifically, TS_{3a} is only 16.7 kcal/mol above $\text{FeO}^- + \text{CH}_4$ and leads to the global IS_5 (CH_3FeOH^-) minimum. Interestingly, the radical mechanism is more demanding and requires 29.7 kcal/mol for the activation of the C–H bond. The recombination of OH and CH_3 bears an energy barrier of 28.3 kcal/mol for the radical mechanism and is prohibitive for the 2 + 2 one (79.6 kcal/mol activation barrier). Overall, Fe^- is not a good mediator for the MTM conversion. In addition, the $\text{Fe}^- + \text{CH}_4$ reaction needs to overcome 44.4 ($S = 3/2$) and 32.0 ($S = 5/2$) kcal/mol barriers.

A final comment is that we found no specific correlation between EAs and activation barriers or other energy quantities. Among the metals studied presently, Pd $^-$ presented the lowest energy barriers, and the reaction of its oxide with methane was the only clearly exothermic one. Fe^- and Pt^- (atoms with the lowest and highest EA) were found to rest at the opposite extreme, especially Fe^- with large activation barriers and an endothermic $\text{FeO}^- + \text{CH}_4$ path. The common feature for all of the metals is that only 10–15 kcal/mol are required for the release of methanol, which is nearly independent of the metal.

CONCLUSIONS

In the present work, we presented a fundamental high-level computational investigation on the conversion of methane to methanol mediated by transition metal anions. The advantage of anionic metal centers is their weak interaction with the produced methanol, which can translate into short residence times of methanol around the catalytic center and the reduced possibility of the overoxidation of methanol. This observation is along the same lines of the idea expressed in the literature that methanol should be withdrawn fast from the catalytic center. Polar solvents can facilitate this process. Another advantage of metal anions is that their direct reaction with CH_4 bears an activation barrier, which prevents the formation of stable CH_3MH^- that can potentially poison the catalyst. Certainly, a more extended search is necessary to identify efficient practical catalysts, but this work sets the avenue for this exploration.

Specifically, the interaction energy of methanol with the negative charged metal center is small (10–15 kcal/mol) and practically independent of the metal nature. No specific correlation was identified between the EA of the metal and the energetics of the catalytic cycle, but a large EA value will ensure the return of the electron to the metal center after the end of each cycle. Our findings suggest that future work should use the metal–oxygen binding energy as an indicator (it should be smaller than ~ 100 kcal/mol) and focus on the C–H activation and CH_3 –OH recombination barriers. For practical applications, ligands that preserve the negative charge of the metal and avoid the formation of CH_3MOH^- units by promoting the radical mechanism must be located. Contrary

to the claims in the literature that the radical mechanism must be avoided for higher selectivity, in the case of anionic systems this seems to be of less importance provided that methanol is picked up and removed by the solvent quickly due to the weak metal–methanol attraction. We finally explained the radical C–H activation mechanism as a sort of PCET, and we saw that the activation barrier correlates to the proton affinity of the metal oxide.

Among the four metals employed (group 10 metals and iron), the lowest- and highest-EA metals (Fe and Pt) presented the largest activation energy barriers, and the best performance is found for Pd⁻. The calculations for Fe⁻ were proven quite demanding, and thus we devised a new approach. An electronic state with a single-reference wave function (not necessarily the ground state) is identified and is studied at a high level and a size-extensive RCCSD(T) level. This RCCSD(T) energy is set as the reference energy for the MRCI calculations used for the rest of the electronic states.

Our results are useful for future gas-phase experiments, similar to those done for cationic species. Our future work will focus on screening more metal centers and identifying proper ligands for the design of efficient and selective molecular catalysts. More rigorous kinetic models will be employed for the assessment of the catalytic efficiency.

■ ASSOCIATED CONTENT

Supporting Information

The Supporting Information is available free of charge at <https://pubs.acs.org/doi/10.1021/acs.jpca.0c10577>.

Optimal geometries (Tables S2, 12, 15), electronic energies (Tables S3–S9, S13, S16, S16a, S17, S19), and harmonic vibrational frequencies (Tables S10, S11, S14, S18) for all of the structures (minima and transition states); numerical data points for Figures 3, 4, and 6–9 (Tables S20–S25); MN15 and RCCSD(T) energy diagrams for the catalytic cycle of iron for sextet and quartet spin multiplicities (Figure S1); identical figures as Figures 4 and 7 but with shifted energy scale (Figures S2 and S3) (PDF)

■ AUTHOR INFORMATION

Corresponding Author

Evangelos Miliordos – Department of Chemistry and Biochemistry, Auburn University, Auburn, Alabama 36849, United States; orcid.org/0000-0003-3471-7133; Email: emiliord@auburn.edu

Author

Safaa Sader – Department of Chemistry and Biochemistry, Auburn University, Auburn, Alabama 36849, United States

Complete contact information is available at: <https://pubs.acs.org/doi/10.1021/acs.jpca.0c10577>

Notes

The authors declare no competing financial interest.

■ ACKNOWLEDGMENTS

The authors are indebted to Auburn University (AU) for financial support. This work was completed with resources provided by the Auburn University Hopper Cluster and Alabama Supercomputer Center.

■ REFERENCES

- (1) Kioes, S.; Liebner, W. Methane—The Promising Career of a Humble Molecule. *J. Natural Gas Chem.* **2004**, *13*, 71–78.
- (2) Chinchon, G. C.; Denny, P. J.; Jennings, J. R.; Spencer, M. S.; Waugh, K. C. Synthesis of Methanol: Part I. Catalysts and Kinetics. *Appl. Catal.* **1988**, *36*, 1–65.
- (3) Zhao, X.; Joseph, B.; Kuhn, J.; Ozcan, S. Biogas Reforming to Syngas: A Review. *iScience* **2020**, *23*, 101082.
- (4) Eller, K.; Schwarz, H. Trends Across the Periodic Table - A Screening of the Gas-Phase Chemistry of d-Block Transition-Metal Ions with Isocyanides. *Chem. Ber.* **1990**, *123*, 201–208.
- (5) Latimer, A. A.; Kakekhani, A.; Kulkarni, A. R.; Nørskov, J. K. Direct Methane to Methanol: The Selectivity-Conversion Limit and Design Strategies. *ACS Catal.* **2018**, *8*, 6894–6907.
- (6) Ravi, M.; Ranocchiar, M.; van Bokhoven, J. A. The Direct Catalytic Oxidation of Methane to Methanol—A Critical Assessment. *Angew. Chem., Int. Ed.* **2017**, *56*, 16464–16483.
- (7) Hashiguchi, B. G.; Bischof, S. M.; Konnick, M. M.; Periana, R. A. Designing Catalysts for Functionalization of Unactivated C-H Bonds Based on the CH Activation Reaction. *Acc. Chem. Res.* **2012**, *45*, 885–898.
- (8) Sunderlin, L. S.; Armentrout, P. B. Periodic Trends in Chemical Reactivity: Reactions of Sc⁺, Y⁺, La⁺, and Lu⁺ with Methane and Ethane. *J. Am. Chem. Soc.* **1989**, *111*, 3845–3855.
- (9) Schröder, D.; Schwarz, H. FeO⁺ Activates Methane. *Angew. Chem., Int. Ed. Engl.* **1990**, *29*, 1433–1434.
- (10) Schröder, D.; Schwarz, H. C-H and C-C Bond Activation by Bare Transition-Metal Oxide Cations in the Gas Phase. *Angew. Chem., Int. Ed. Engl.* **1995**, *34*, 1973–1995.
- (11) Védrine, J. C. Heterogeneous Catalysis on Metal Oxides. *Catalysts* **2017**, *7*, 341.
- (12) Schwarz, H. Chemistry with Methane: Concepts Rather than Recipes. *Angew. Chem., Int. Ed.* **2011**, *50*, 10096–10115.
- (13) Carsch, K. M.; Cundari, T. R. DFT Modeling of a Methane-to-methanol Catalytic Cycle via Group 6 Organometallics: The Role of Metal in Determining the Mode of C-H Activation. *Comput. Theor. Chem.* **2012**, *980*, 133–137.
- (14) Kirkland, J. K.; Khan, S. N.; Casale, B.; Miliordos, E.; Vogiatzis, K. D. Ligand Field Effects on the Ground and Excited States of Reactive FeO²⁺ Species. *Phys. Chem. Chem. Phys.* **2018**, *20*, 28786–28795.
- (15) Ariyaratna, I. R.; Miliordos, E. Radical Abstraction vs. Oxidative Addition Mechanisms for the Activation of the S-H, O-H, and C-H Bonds Using Early Transition Metal Oxides. *Phys. Chem. Chem. Phys.* **2021**, *23*, 1437.
- (16) Haynes, C. L.; Chen, Y.-M.; Armentrout, P. B. The Potential Energy Surface for Activation of Methane by Co⁺: An Experimental Study. *J. Phys. Chem.* **1995**, *99*, 9110–9117.
- (17) Armentrout, P. B. Activation of CH₄ by Gas-Phase Mo⁺, and the Thermochemistry of Mo-ligand Complexes. *J. Phys. Chem. A* **2006**, *110*, 8327–8338.
- (18) Chen, Y.-M.; Armentrout, P. B. Activation of Methane by Gas-Phase Rh⁺. *J. Phys. Chem.* **1995**, *99*, 10775–10779.
- (19) Lapoutre, V. J. F.; Redlich, B.; van der Meer, A. F. G.; Oomens, J.; Bakker, J. M.; Sweeney, A.; Mookherjee, A.; Armentrout, P. B. Structures of the Dehydrogenation Products of Methane Activation by 5d Transition Metal Cations. *J. Phys. Chem. A* **2013**, *117*, 4115–4126.
- (20) Wesendrup, R.; Schröder, D.; Schwarz, H. Catalytic Pt⁺-Mediated Oxidation of Methane by Molecular Oxygen in the Gas Phase. *Angew. Chem., Int. Ed. Engl.* **1994**, *33*, 1174–1176.
- (21) Msezane, A. Z.; Felli, Z.; Suggs, K.; Tesfamichael, A.; Wang, X.-Q. Gold Anion Catalysis of Methane to Methanol. *Gold Bull.* **2012**, *45*, 127–135.
- (22) Tesfamichael, A.; Suggs, K.; Felli, Z.; Msezane, A. Z. Methane Oxidation to Methanol without CO₂ Emission: Catalysis by Atomic Negative Ions. *arXiv (Physics: Chemical Physics)* **2014**, arXiv: 14030597.

- (23) Liu, G.; Zhu, Z.; Ciborowski, S. M.; Ariyaratna, I. R.; Miliordos, E.; Bowen, K. H. Selective Activation of the C-H Bond in Methane by Single Platinum Atomic Anions. *Angew. Chem., Int. Ed.* **2019**, *58*, 7773–7777.
- (24) Achatz, U.; Berg, C.; Joos, S.; Fox, B. S.; Beyer, M. K.; Niedner-Schatteburg, G.; Bondybey, V. E. Methane Activation by Platinum Cluster Ions in the Gas Phase: Effects of Cluster Charge on the Pt-4 Tetramer. *Chem. Phys. Lett.* **2000**, *320*, 53–58.
- (25) Khan, S. N.; Miliordos, E. Methane to Methanol Conversion Facilitated by Transition-Metal Methyl and Methoxy Units: The Cases of FeCH_3^+ and FeOCH_3^+ . *J. Phys. Chem. A* **2019**, *123*, 5590–5599.
- (26) Almeida, N. M. S.; Ariyaratna, I. R.; Miliordos, E. O-H and C-H Bond Activations of Water and Methane by RuO^{2+} and $(\text{NH}_3)\text{RuO}^{2+}$: Ground and Excited States. *J. Phys. Chem. A* **2019**, *123*, 9336–9344.
- (27) Claveau, E. E.; Miliordos, E. Quantum Chemical Calculations on NbO and Its Reaction with Methane: Ground and Excited Electronic States. *Phys. Chem. Chem. Phys.* **2019**, *21*, 26324–26332.
- (28) Jackson, B. A.; Miliordos, E. Weak-field Ligands Enable Inert Early Transition Metal Oxides to Convert Methane to Methanol: The Case of ZrO. *Phys. Chem. Chem. Phys.* **2020**, *22*, 6606–6618.
- (29) Haynes, W. M. *CRC Handbook of Chemistry and Physics*, 93rd ed.; CRC Press: Boca Raton, FL, 2012.
- (30) Kozuch, S. A Refinement of Everyday Thinking: The Energetic Span Model for Kinetic Assessment of Catalytic Cycles. *WIREs Comput. Mol. Sci.* **2012**, *2*, 795–815.
- (31) Kozuch, S.; Shaik, S. How to Conceptualize Catalytic Cycles? The Energetic Span Model. *Acc. Chem. Res.* **2011**, *44*, 101–110.
- (32) Yu, H. S.; He, X.; Li, S. L.; Truhlar, D. G. MN15: A Kohn-Sham Global-hybrid Exchange-correlation Density Functional with Broad Accuracy for Multi-reference and Single-reference Systems and Noncovalent Interactions. *Chem. Sci.* **2016**, *7*, 5032–5051.
- (33) Balabanov, N. B.; Peterson, K. A. Systematically Convergent Basis Sets for Transition Metals. I. All-electron Correlation Consistent Basis Sets for the 3d Elements Sc-Zn. *J. Chem. Phys.* **2005**, *123*, 064107.
- (34) Dunning, T. H. Gaussian Basis Sets for Use in Correlated Molecular Calculations. I. The Atoms Boron Through Neon and Hydrogen. *J. Chem. Phys.* **1989**, *90*, 1007–1023.
- (35) Kendall, R. A.; Dunning, T. H.; Harrison, R. J. Electron Affinities of the First-row Atoms Revisited. Systematic Basis Sets and Wave Functions. *J. Chem. Phys.* **1992**, *96*, 6796–6806.
- (36) Figgen, D.; Peterson, K. A.; Dolg, M.; Stoll, H. Energy-consistent Pseudopotentials and Correlation Consistent Basis Sets for the 5d Elements Hf-Pt. *J. Chem. Phys.* **2009**, *130*, 164108.
- (37) Peterson, K. A.; Figgen, D.; Dolg, M.; Stoll, H. Energy-consistent Relativistic Pseudopotentials and Correlation Consistent Basis Sets for the 4d Elements Y-Pd. *J. Chem. Phys.* **2007**, *126*, 124101.
- (38) Raghavachari, K.; Trucks, G. W.; Pople, J. A.; Head-Gordon, M. A Fifth-order Perturbation Comparison of Electron Correlation Theories. *Chem. Phys. Lett.* **1989**, *157*, 479–483.
- (39) Bartlett, R. J.; Watts, J. D.; Kucharski, S. A.; Noga, J. Non-iterative Fifth-Order Triple and Quadruple Excitation Energy Corrections in Correlated Methods. *Chem. Phys. Lett.* **1990**, *165*, 513–522.
- (40) Shamasundar, K. R.; Knizia, G.; Werner, H.-J. A New Internally Contracted Multi-reference Configuration Interaction Method. *J. Chem. Phys.* **2011**, *135*, 054101.
- (41) Berning, A.; Schweizer, M.; Werner, H.-J.; Knowles, P. J.; Palmieri, P. Spin-orbit Matrix Elements for Internally Contracted Multireference Configuration Interaction Wavefunctions. *Mol. Phys.* **2000**, *98*, 1823–1833.
- (42) Frisch, M. J.; Trucks, G. W.; Schlegel, H. B.; Scuseria, G. E.; Robb, M. A.; Cheeseman, J. R.; Scalmani, G.; Barone, V.; Petersson, G. A.; Nakatsuji, H.; et al. *Gaussian 16*, rev. B.01; Gaussian, Inc.: Wallingford, CT, 2016.
- (43) Werner, H.-J.; Knowles, P. J.; Knizia, G.; Manby, F. R.; Schütz, M.; Celani, P.; GYÖRFFY, W.; Kats, D.; Korona, T.; Lindh, R.; et al. *MOLPRO*, version 2015.1, a package of ab initio programs, 2015.
- (44) Werner, H.-J.; Knowles, P. J.; Manby, F. R.; Black, J. A.; Doll, K.; Heßelmann, A.; Kats, D.; Köhn, A.; Korona, T.; Kreplin, D. A.; et al. The Molpro Quantum Chemistry Package. *J. Chem. Phys.* **2020**, *152*, 144107.
- (45) Xu, X.; Faglioni, F.; Goddard, W. A. Methane Activation by Transition-Metal Oxides, MO_x ($M = \text{Cr, Mo, W}$; $x = 1, 2, 3$). *J. Phys. Chem. A* **2002**, *106*, 7171–7176.
- (46) Ramond, T. M.; Davico, G. E.; Hellberg, F.; Svedberg, F.; Salén, P.; Söderqvist, P.; Lineberger, W. C. Photoelectron Spectroscopy of Nickel, Palladium, and Platinum Oxide Anions. *J. Mol. Spectrosc.* **2002**, *216*, 1–14.
- (47) Peppernick, S. J.; Gunaratne, K. D. D.; Castleman, A. W. Superatom Spectroscopy and the Electronic State Correlation Between Elements and Isoelectronic Molecular Counterparts. *Proc. Natl. Acad. Sci. U. S. A.* **2010**, *107*, 975.
- (48) Bilodeau, R. C.; Scheer, M.; Haugen, H. K.; Brooks, R. L. Near-threshold Laser Spectroscopy of Iridium and Platinum Negative Ions: Electron Affinities and the Threshold Law. *Phys. Rev. A: At, Mol., Opt. Phys.* **1999**, *61*, 012505.
- (49) Rasheed, W.; Draksharapu, A.; Banerjee, S.; Young, V. G., Jr.; Fan, R.; Guo, Y.; Ozerov, M.; Nehr Korn, J.; Krzystek, J.; Telsler, J.; et al. Crystallographic Evidence for a Sterically Induced Ferryl Tilt in a Non-Heme Oxoiron(IV) Complex that Makes it a Better Oxidant. *Angew. Chem., Int. Ed.* **2018**, *57*, 9387–9391.
- (50) Almeida, N. M. S.; Ariyaratna, I. R.; Miliordos, E. Ab Initio Calculations on the Ground and Excited Electronic States of Neutral and Charged Palladium Monoxide, $\text{PdO}^{0/+}$. *Phys. Chem. Chem. Phys.* **2018**, *20*, 14578–14586.
- (51) Božović, A.; Feil, S.; Koyanagi, G. K.; Viggiano, A. A.; Zhang, X.; Schlangen, M.; Schwarz, H.; Bohme, D. K. Conversion of Methane to Methanol: Nickel, Palladium, and Platinum (d9) Cations as Catalysts for the Oxidation of Methane by Ozone at Room Temperature. *Chem. - Eur. J.* **2010**, *16*, 11605–11610.
- (52) Shiota, Y.; Yoshizawa, K. Methane-to-Methanol Conversion by First-Row Transition-Metal Oxide Ions: ScO^+ , TiO^+ , VO^+ , CrO^+ , MnO^+ , FeO^+ , CoO^+ , NiO^+ , and CuO^+ . *J. Am. Chem. Soc.* **2000**, *122*, 12317–12326.
- (53) Sakellaris, C. N.; Mavridis, A. First Principles Exploration of NiO and Its Ions NiO^+ and NiO^- . *J. Chem. Phys.* **2013**, *138*, 054308.
- (54) Yoshizawa, K.; Shiota, Y.; Yamabe, T. Methane-Methanol Conversion by MnO^+ , FeO^+ , and CoO^+ : A Theoretical Study of Catalytic Selectivity. *J. Am. Chem. Soc.* **1998**, *120*, 564–572.
- (55) Perera, M.; Metz, R. B.; Kostko, O.; Ahmed, M. Vacuum Ultraviolet Photoionization Studies of PtCH_2 and H-Pt-CH_3 : A Potential Energy Surface for the Pt+CH_4 Reaction. *Angew. Chem., Int. Ed.* **2013**, *52*, 888–891.
- (56) Zhang, X.-G.; Liyanage, R.; Armentrout, P. B. Potential Energy Surface for Activation of Methane by Pt^+ : A Combined Guided Ion Beam and DFT Study. *J. Am. Chem. Soc.* **2001**, *123*, 5563–5575.
- (57) Leopold, D. G.; Lineberger, W. C. A Study of the Low-lying Electronic States of Fe_2 and Co_2 by Negative Ion Photoelectron Spectroscopy. *J. Chem. Phys.* **1986**, *85*, 51–55.
- (58) Andersen, T.; Lykke, K. R.; Neumark, D. M.; Lineberger, W. C. Autodetachment Study of the Electronic Spectroscopy of FeO^- . *J. Chem. Phys.* **1987**, *86*, 1858–1867.
- (59) Drechsler, G.; Boesl, U.; Bässmann, C.; Schlag, E. W. Mass Selected Anion-zero Kinetic Energy Photoelectron Spectroscopy (Anion-ZEKE): Ground and Low Excited States of FeO . *J. Chem. Phys.* **1997**, *107*, 2284–2291.
- (60) Sakellaris, C. N.; Miliordos, E.; Mavridis, A. First Principles Study of the Ground and Excited States of FeO , FeO^+ , and FeO^- . *J. Chem. Phys.* **2011**, *134*, 234308.



Cite this: *Phys. Chem. Chem. Phys.*,
2022, 24, 21583

Received 18th June 2022,
Accepted 6th September 2022

DOI: 10.1039/d2cp02771b

rsc.li/pccp

Being negative can be positive: metal oxide anions promise more selective methane to methanol conversion†

Safaa Sader and Evangelos Miliordos *

Computational studies are performed to show that metal oxide anionic complexes promote the $\text{CH}_4 + \text{N}_2\text{O} \rightarrow \text{CH}_3\text{OH} + \text{N}_2$ reaction with low activation barriers for the C–H activation and the formation of the $\text{CH}_3\text{–OH}$ bond. The energy for the release of the produced methanol is minimal, reducing the residence time of methanol around the catalytic center and preventing its overoxidation.

Methane to methanol conversion is a topic of high interest and intense research. The ample methane underground reserves and the new extraction methods (fracking) render methane a valuable carbon source.¹ Its direct conversion to liquid methanol under mild conditions at the location of extraction can facilitate the transportation to industrial plants for further processing. Methanol can serve both as fuel and a platform chemical.² The concept of methanol economy had been introduced two decades ago.³ Several laboratory techniques have been probed including (but not limited to) zeolites, metal-organic frameworks, enzymes, frustrated Lewis pairs, and molecular catalysts,^{4–10} all with partial success. The fact that the C–H bond of the produced methanol is weaker than that in methane renders methanol predisposed to overoxidation to formaldehyde and other methanol derivatives.¹¹ As a result, higher conversion rates are achieved at the expense of selectivity.^{11,12} One of the proposed solutions in the literature is to expedite the diffusion of methanol from the catalytic center to the solvent.¹¹ The weaker interaction of methanol with anionic (electron-rich) metal centers compared to the commonly used positively charged metal centers can perfectly serve this role.

The currently proposed catalysts are molecular metal oxide anions, the catalytic cycle for which is shown in Fig. 1. The [M] notation represents the ligated metal center and [O] represents

the oxidant, which is N_2O in this study since it has been shown to oxidize promptly anionic metal centers.¹³ $[\text{M}]\text{O}^-$ activates methane in two ways, either *via* a [2+2] insertion, producing the $\text{HO}[\text{M}]\text{CH}_3^-$ adduct, or a radical mechanism, making $[\text{M}]\text{OH}^-$ and releasing a CH_3 radical. The latter mechanism happens as proton-coupled electron transfer (PCET) and is facilitated by the radical nature of the catalyst ($S = 1/2$).¹³ Then the two units OH and CH_3 combine to give methanol, $[\text{M}]^- \cdots \text{HOCH}_3$, which is promptly released (see below). The electron affinity of the metal center should be large enough to secure the abidance of the electron to the metal, and the interaction energy of $[\text{M}]^-$ with CH_3OH should be small. Finally $[\text{M}]^-$ is oxidized to $[\text{M}]\text{O}^-$ closing the catalytic cycle.

Small metal oxide cluster anions have been studied for the activation of CH_4 in the past (gas-phase experiments),^{14–20} but to our knowledge, no molecular complexes have been probed so far. Synthetic routes for molecular systems like the ones proposed presently (nickel, palladium, platinum anionic complexes with methyl or aryl ligands) have been reported in the literature.^{21–36}

In our previous study, we located the intermediates/transition states and constructed the energy landscape for the Group

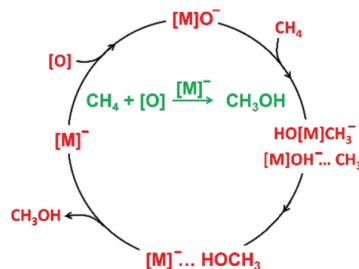


Fig. 1 Proposed catalytic cycle for the methane to methanol transformation facilitated by the metal oxide anion $[\text{M}]\text{O}^-$. [M] indicates ligated metal and [O] indicates an oxidant.

Department of Chemistry and Biochemistry, Auburn University, Auburn, AL, 36849, USA. E-mail: emiliord@auburn.edu

† Electronic supplementary information (ESI) available: Additional electronic and free energy diagrams, numerical data for all energy diagrams, geometries and frequencies for all intermediate and transition state structures are listed in the Fig. S1–S11 and Tables S1–S7 of ESI. See DOI: <https://doi.org/10.1039/d2cp02771b>

10 metals (Ni, Pd, Pt); no ligands were considered in that study.¹³ For all three metals, a PCET mechanism is energetically favored for the activation of the H-CH₃ bond and the oxidation step is practically barrier-free.¹³

The best performance was observed for Pd provided it runs through the [M]OH⁻·CH₃ intermediate, and not HOPdCH₃⁻, which is a very stable intermediate, and must be avoided to prevent poisoning of the catalyst. In addition, the electron affinity of Pd is the smallest among the three metals, which may raise a question about the viability of a quasi-Pd⁻ center. The solution proposed in our earlier work was the inclusion of ligands that (1) destabilize the [2+2] adduct (HOPdCH₃⁻) due to steric repulsions and (2) increase the electron affinity of the metal center. In this work we show that using CH₃ as ligands satisfies both requirements. Initially, we use the model system M(CH₃)₄⁻, where M = Ni, Pd, Pt, to construct the energy landscape at high levels of theory and benchmark the used density functional, which is used for the study of larger systems (see below).

All structures were optimized with Density Functional Theory (DFT) with the MN15 functional.³⁷ The aug-cc-pVTZ basis set (TZ) is used for H, C, N, O, Ni, and aug-cc-pVTZ-PP for Pd, Pt.^{38–45} All intermediate structures are minima in their potential energy surface (real frequencies) and all transition states have one imaginary frequency. Single point energy calculations are performed at the Coupled Cluster Singles Doubles and perturbative Triples, CCSD(T),^{46,47} with the aug-cc-pVDZ (DZ) basis sets. The unrestricted version for both DFT and CCSD(T) calculations is employed as implemented in Gaussian 16.⁴⁸ Finally, CCSD(T)/TZ energies are estimated as $E[\text{CCSD(T)}/\text{TZ}] = E[\text{CCSD(T)}/\text{DZ}] + E[\text{MN15}/\text{TZ}] - E[\text{MN15}/\text{DZ}]$.

The MN15/TZ structures are shown in Fig. 2. R is the interaction complex between methane and metal oxide. TS1R, I1, and TS1P correspond to the PCET mechanism. One proton is transferred from CH₄ to oxygen and an electron migrates

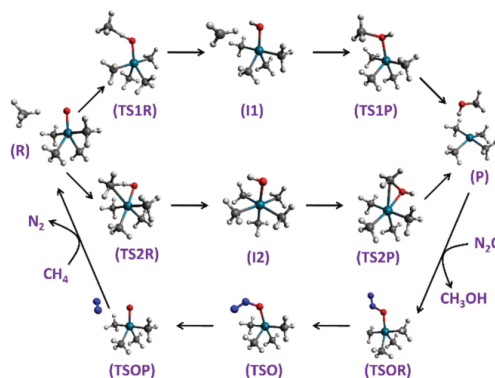


Fig. 2 Structures of all intermediates and transition states for the CH₄ + N₂O → CH₃OH + N₂ reaction facilitated by (CH₃)₄PdO⁻. The PCET/[2+2] mechanisms are shown in the top/middle lines, while the bottom line corresponds to the oxidation step.

Table 1 Activation energy barriers (kcal mol⁻¹) for the Ni, Pd, and Pt species with methyl or biphenyl (Bp) ligands

Method	$E_a(1R)^a$	$E_a(1P)^b$	$E_a(2R)^c$	$E_a(2P)^d$	E_{ts}^e	E_{ox}^f
			[M] = Pd(CH ₃) ₄			
MN15/DZ	17.4	16.4	23.5	22.9	13.3	2.3
MN15/TZ	18.2	17.0	26.3	23.3	12.3	4.0
CCSD(T)/DZ	16.7	18.1	25.4	24.3	12.0	2.0
CCSD(T)/TZ	17.5	18.7	28.1	24.7	11.0	0.2
			[M] = Ni(CH ₃) ₄			
MN15/TZ	21.4	17.6	30.7	16.7	13.6	10.7
			[M] = Pt(CH ₃) ₄			
MN15/TZ	21.9	20.7	28.4	36.8	12.3	0.4
			[M] = Pd(Bp) ₂			
MN15/TZ	19.3	16.9	28.5	20.3	12.0	7.6

^a Calculated as the energy difference between TS1R and R (see Fig. 2).

^b Calculated as the energy difference between TS1P and I1. ^c Calculated as the energy difference between TS2R and R. ^d Calculated as the energy difference between TS2P and I2. ^e Calculated as the energy difference between P and [M] + CH₃OH. ^f Calculated as the energy difference between TSOR and TSO.

from CH₄ to the metal center.¹³ The TS2R/I2/TS2P path composes the [2+2] avenue. Methanol is released from the produced (CH₃)₄Pd⁻·HOCH₃ species and oxygen is loaded on the metal *via* the TSOR/TSO/TSOP route to close the catalytic cycle. The values for the activation barriers of the PCET and [2+2] mechanisms are listed in Table 1 and the overall energy diagram is demonstrated in Fig. 3. To make Fig. 3 we added the energy of N₂ for the R → P part and the energy of CH₄ for the oxidation step. The activation barriers fluctuate within 2.5 kcal mol⁻¹ for the different computational levels, except for $E_a(2R)$, which changes by 5 kcal mol⁻¹ from MN15/DZ to CCSD(T)/TZ and corresponds to the first step of the [2+2] path (R → TS2R). This barrier is the highest one and the system is not expected to access it. The larger basis sets and the inclusion of electron correlation *via* CCSD(T) increase the barriers, but don't seem to affect the energy needed to release methanol from the catalytic

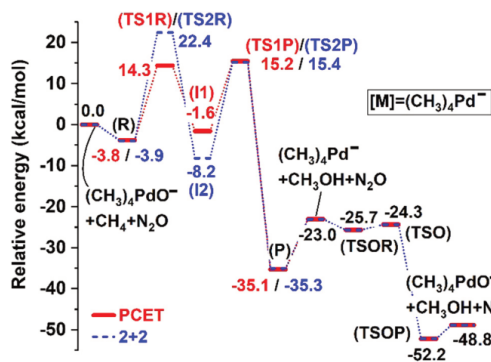


Fig. 3 MN15/TZ potential energy diagram for the CH₄ + N₂O → CH₃OH + N₂ reaction facilitated by (CH₃)₄PdO⁻. The structures for both PCET and [2+2] mechanisms are depicted in Fig. 2.

center. Our best results, CCSD(T)/TZ, differ from MN15/TZ by less than 2.0 kcal mol⁻¹ and thus MN15/TZ is considered quite accurate with reduced computational cost and is used for the rest of the catalytic systems.

The MN15/TZ results for the other two metals and another ligand [Pd with biphenyl (Bp) ligands; see Fig. S10, ESI† for structures] are also listed in Table 1 and energy diagrams are given in the ESI† (Fig. S1–S5). Biphenyl is selected as a more practical ligand commonly used (pure or its derivatives) in organic/organometallic synthesis as fairly non-reactive ligand.⁴⁹ The trends are the same for all four systems: The lowest barriers are observed for the PCET mechanism, $E_a(1R)/E_a(1P)$, and are of the 20 kcal mol⁻¹ order (16.9–21.9 kcal mol⁻¹). The [2+2] mechanism requires a large CH activation barrier, $E_a(2R)$, ranging from 28.1 to 30.7 kcal mol⁻¹, while the second (CH₃–OH recombination) step demonstrates a wide range of values (16.7–36.8 kcal mol⁻¹). The interaction energy between [M]⁻ and CH₃OH is rather independent of the metal center or ligands (12.0–13.6 kcal mol⁻¹). Finally looking at the energy diagrams (Fig. 3 and Fig. S1–S5, ESI†), it is obvious that the CH₃[M]OH⁻ intermediate is no longer the very stable intermediate observed in the base of bare metals¹³ (except for [M] = (CH₃)₄Pt). In addition, the oxidation step is nearly barrier-free (activation energies smaller than 11 kcal mol⁻¹) closing readily the catalytic cycle (see Fig. 1 and 3), but this should be considered an upper limit since there is an alternative mechanism found earlier with even smaller barriers.¹³

The second bottleneck encountered for bare metal oxide anions was the low electron affinity (EA) of the best-performing metal (Pd). The vertical EA values (energy difference between anionic and neutral species at the geometry of the anion) of (CH₃)₄Ni, (CH₃)₄Pd, and (CH₃)₄Pt, are 2.65 (2.96), 2.28 (2.56), and 2.35 (2.56) eV at CCSD(T)/DZ (MN15/TZ). The MN15/DZ value for (CH₃)₄Pd is 2.58 eV attributing the difference between MN15/TZ and CCSD(T)/DZ to the method and not the basis set. The vertical EA value for (Bp)₂Pd is 3.33 eV at MN15/DZ, which should be overestimated by ~0.3 eV and is even larger than (CH₃)₄Pd. All these values are larger than the EA of Pt, which has one of the largest EAs among all metals

(experimentally 2.128 eV).⁵⁰ In addition, EAs are practically independent of the metal as opposed to bare metals (1.156/1.04 eV for Ni, 0.562/0.39 eV for Pd, and 2.128/2.02 eV for Pt experimentally/CCSD(T)/DZ). The anionic systems always have doublet spin multiplicity with one unpaired electron on the metal and the neutral systems are always closed-shell singlets (see Table S1 of ESI†). The unpaired electron occupies the orbital of Fig. S8 of ESI† and indicates that the additional electron is shared mainly among the Pd atom and two methyl groups in agreement with the Natural Population Analysis.^{51,52} These two methyl units are initially positively charged (+0.16) and receive 0.36 e⁻, while the metal has initially a +0.41 charge and receives 0.15 e⁻. The other two methyl groups possess already a -0.37 charge e⁻ and they receive only 0.06 e⁻. In summary, the charges in (Me)₄Pd⁻ are +0.26 for Pd, and -0.19/-0.43 for the two different methyl groups. When oxygen binds to Pd, the metallic charge remains practically the same (+0.27) and 0.14 electrons of each methyl group migrate to the oxygen center, which has a -0.55 charge. This is indicative of metal–ligand cooperativity where the ligands play a role of electron bank during the reaction.

Next, we considered the free energy diagrams at a temperature of 298.15 K and a pressure of 1.0 atm. Free energies are obtained with the harmonic approximation implemented in Gaussian.⁴⁸ These are shown in Fig. S7 (ESI†) and the energy values are listed in Table S2 of the ESI†. The entropic factor minimizes the energy needed for the release of methanol to less than 2.0 kcal mol⁻¹ allowing for the fast removal of methanol from the catalytic center preventing its overoxidation.

To quantify the performance of the selected catalysts, identify the dominant reaction path, and locate the rate-determining step, we performed a kinetic analysis. We approximated the forward and reverse rate constants k for all five reaction steps as^{53–55}

$$k = \frac{RT}{h} \left(\frac{RT}{p} \right)^n e^{-\frac{\Delta G^\ddagger}{RT}},$$

where k_B , T , p , h , ΔG^\ddagger , and R are the Boltzmann's constant, temperature, pressure, Planck's constant, free energy activation

Table 2 Rate constants k for the reaction steps of Fig. 2, and $t_{1/2}$, TOF, δE for the overall catalytic cycle employing [M]O⁻ as catalysts

Reaction step	[M]			
	(CH ₃) ₄ Ni	(CH ₃) ₄ Pd	(CH ₃) ₄ Pt	(Bp) ₂ Pd
[M]O ⁻ + CH ₄ → I1	3.16 × 10 ¹	2.68 × 10 ²	2.26 × 10 ⁻¹	2.81 × 10 ²
I1 → [M]O ⁻ + CH ₄	4.15 × 10 ¹	1.51 × 10 ¹	9.22 × 10 ¹	5.49
I1 → [M] ⁻ + CH ₃ OH	4.78 × 10 ⁻³	1.28 × 10 ⁻²	2.27 × 10 ⁻⁵	1.39 × 10 ⁻¹
[M] ⁻ + CH ₃ OH → I1	5.41 × 10 ⁻²⁸	4.07 × 10 ⁻²⁴	9.92 × 10 ⁻²²	5.40 × 10 ⁻²⁰
[M]O ⁻ + CH ₄ → I2	3.66 × 10 ⁻⁹	8.05 × 10 ⁻⁵	2.89 × 10 ⁻⁷	2.40 × 10 ⁻⁶
I2 → [M]O ⁻ + CH ₄	1.04 × 10 ⁻⁶	1.75 × 10 ⁻⁸	7.25 × 10 ⁻¹¹	2.11 × 10 ⁻¹⁰
I2 → [M] ⁻ + CH ₃ OH	2.15 × 10 ¹	4.62 × 10 ⁻⁵	4.49 × 10 ⁻¹³	1.44 × 10 ⁻²
[M] ⁻ + CH ₃ OH → I2	4.70 × 10 ⁻²⁶	4.43 × 10 ⁻²⁴	3.04 × 10 ⁻²³	6.22 × 10 ⁻²⁰
[M] ⁻ + N ₂ O → [M]O ⁻ + N ₂	9.79 × 10 ¹	1.08 × 10 ⁶	5.56 × 10 ⁹	2.44 × 10 ⁶
[M]O ⁻ + N ₂ → [M] ⁻ + N ₂ O	6.57 × 10 ⁻¹³	6.44 × 10 ⁻¹¹	5.12 × 10 ⁻¹⁶	3.02 × 10 ⁻¹³
$t_{1/2}/s$	3077	419	∞ ^a	37.5
TOF/s	1.40 × 10 ⁻⁴	5.4 × 10 ⁻³	2.3 × 10 ⁻⁹	9.3 × 10 ⁻²
$\delta E/kcal mol^{-1}$	22.7	20.2	29.2	18.6

^a The reaction does not proceed beyond the first step (CH activation).

barrier, and the universal gas constant, respectively ($n = 0/1$ for first/second order reaction steps). Table 2 tabulates the k values used for the kinetics studies. For these studies, we considered a 10% catalyst and launched the COPASI software for the solution of the differential equations.⁵⁶ As a measurement of the catalytic efficiency, we use the half-life time needed ($t_{1/2}$) for the production of 50% of CH_3OH . We also employed the energetic span model to estimate the turn-over-frequency (TOF) and energetic span (δE) of the cycle.^{53,54} In the COPASI work, we found that clearly only the PCET mechanism dominates (see Fig S9 of ESI†), and thus we use the PCET energy landscape for the energetic span model.

The main conclusions of our analysis are that the PCET mechanism (*via* I1) is faster and is the main path to the products, the rate determining step (lowest rate constant) is always the CH activation step, $[\text{M}]^{\text{O}^-} + \text{CH}_4 \rightarrow \text{I1}$, while the oxygen reload of the metal plays a minor role to the overall rate. The energetic span model predicts that the TOF-determining intermediate (TDI) is the initial reactants, $[\text{M}]^{\text{O}^-} + \text{CH}_4$, and the TOF-determining transition state (TDTS) is TS1P (see Fig. S11, ESI†). This means that both steps ($\text{R} \rightarrow \text{I1} \rightarrow \text{P}$) are to be considered in future studies.

Comparing the different systems, we see that the lowest $t_{1/2}$, lowest δE , and higher TOF belong to $[\text{M}] = (\text{Bp})_2\text{Pd}$. $[\text{M}] = (\text{CH}_3)_4\text{Ni}$ and $(\text{CH}_3)_4\text{Pd}$ perform very well too, as opposed to $[\text{M}] = (\text{CH}_3)_4\text{Pt}$, the large barriers of which prevent the completion of the reaction. Our predicted $\delta E = 18.6 \text{ kcal mol}^{-1}$ for $[\text{M}] = (\text{Bp})_2\text{Pd}$ and given the accuracy of our electronic structure methods ($\pm 2 \text{ kcal mol}^{-1}$), the $(\text{Bp})_2\text{PdO}^-$ appears to be a promising catalyst. In addition, the ligands seem to offer some flexibility given the variation in δE going from four methyl ligands to two Bp ligands (18.6 to $22.7 \text{ kcal mol}^{-1}$). Pd seems to be the best option, but the performance of Ni (as opposed to Pt) can be further optimized by proper ligands and lead to an inexpensive family of catalysts. In this direction, we also performed calculations for $[\text{M}] = (\text{CH}_3)_4\text{Fe}$. Our MN15/TZ results given in the ESI† (Fig. S6 and Table S3) demonstrate a rather poor performance for Fe, which presents large activation barriers. The same trends were found for “naked” FeO^- .¹³ These trends support the strategy of focusing first on bare oxides and then adding methyl-type ligands for practical applications.

The authors are indebted to Auburn University (AU) for financial support and Prof. David Stanbury (AU) for the insightful discussions. E. M. is especially grateful to the donors of the James E. Land endowment. This work was completed with resources provided by the Auburn University Hopper and Easley Clusters.

Conclusions

We show that metal oxide anionic units combined with proper ligands can provide low activation barriers for the conversion of methane to methanol. The advantage over the commonly used cationic species is the facile release of the produced methanol

reducing the residence time around the catalytic center and avoiding overoxidation of methanol. The use of methyl-type ligands increases the electron affinity of the metal center securing the negative charge on the metal. Our kinetic analysis shows that $(\text{Bp})_2\text{PdO}^-$ is a promising catalyst. Finally, we noticed large dependence of the performance on both the metal and ligand, which offers large chemical space for future explorations.

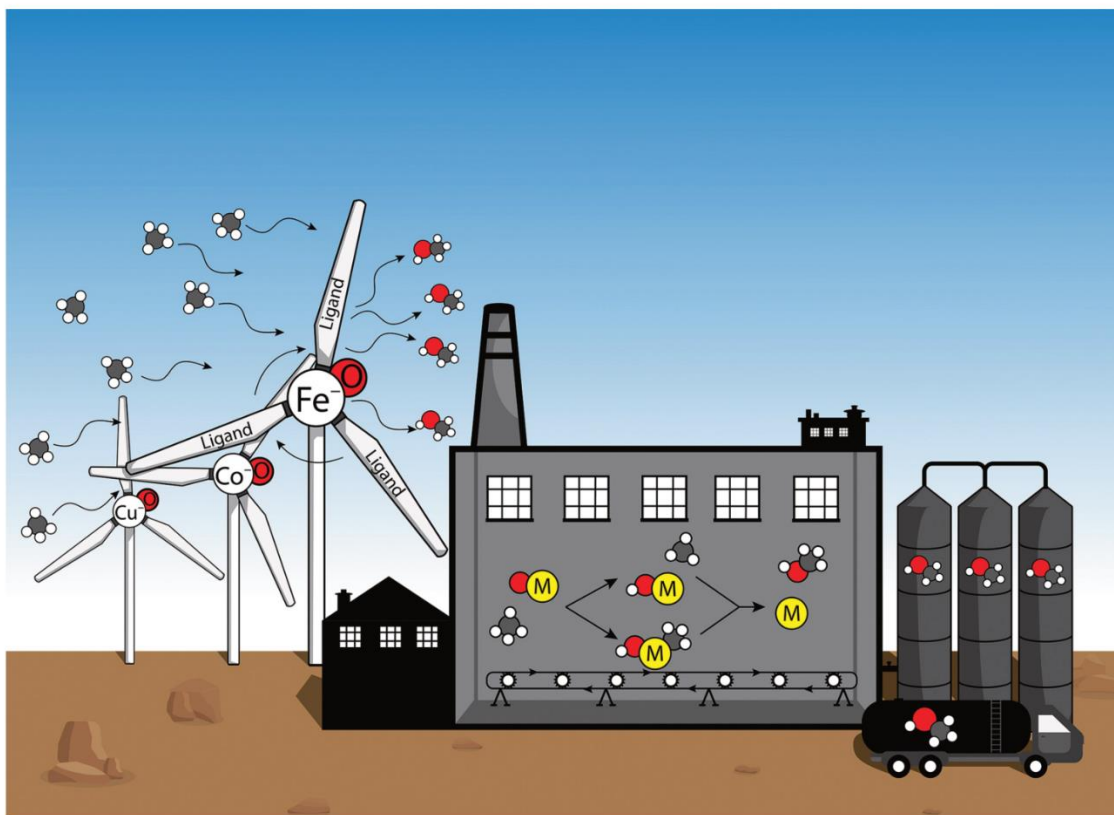
Conflicts of interest

There are no conflicts to declare.

Notes and references

- R. W. Howarth, A. Ingrassia and T. Engelder, *Nature*, 2011, **477**, 271–275.
- G. A. Olah, *Angew. Chem., Int. Ed.*, 2005, **44**, 2636–2639.
- G. A. Olah, *Chem. Eng. News Arch.*, 2003, **81**, 5.
- J. Baek, B. Rungtaweeworanit, X. Pei, M. Park, S. C. Fakra, Y.-S. Liu, R. Matheu, S. A. Alshimri, S. Alshehri and C. A. Trickett, *et al.*, *J. Am. Chem. Soc.*, 2018, **140**, 18208–18216.
- W.-G. Cui, G.-Y. Zhang, T.-L. Hu and X.-H. Bu, *Coord. Chem. Rev.*, 2019, **387**, 79–120.
- B. G. Hashiguchi, S. M. Bischof, M. M. Konnick and R. A. Periana, *Acc. Chem. Res.*, 2012, **45**, 885–898.
- A. R. Kulkarni, Z.-J. Zhao, S. Siahrostami, J. K. Nørskov and F. Studt, *Catal. Sci. Technol.*, 2018, **8**, 114–123.
- T. J. Lawton and A. C. Rosenzweig, *J. Am. Chem. Soc.*, 2016, **138**, 9327–9340.
- M. B. Park, E. D. Park and W.-S. Ahn, *Front. Chem.*, 2019, **7**, 514, DOI: [10.3389/fchem.2019.00514](https://doi.org/10.3389/fchem.2019.00514).
- X. Zhang, Z. Huang, M. Ferrandon, D. Yang, L. Robison, P. Li, T. C. Wang, M. Delferro and O. K. Farha, *Nat. Catal.*, 2018, **1**, 356–362.
- A. A. Latimer, A. Kakekhani, A. R. Kulkarni and J. K. Nørskov, *ACS Catal.*, 2018, **8**, 6894–6907.
- M. Ravi, M. Ranocchiari and J. A. van Bokhoven, *Angew. Chem., Int. Ed.*, 2017, **56**, 16464–16483.
- S. Sader and E. Miliordos, *J. Phys. Chem. A*, 2021, **125**, 2364–2373.
- V. Canale, A. Zavras, G. N. Khairallah, N. d'Alessandro and R. A. J. O'Hair, *Eur. J. Mass Spectrom.*, 2015, **21**, 557–567.
- Y.-K. Li, Y.-X. Zhao and S.-G. He, *J. Phys. Chem. A*, 2018, **122**, 3950–3955.
- M. C. Oliveira, J. Marçalo, M. C. Vieira and M. A. A. Ferreira, *Int. J. Mass Spectrom.*, 1999, **185–187**, 825–835.
- R. B. Wyrwas, B. L. Yoder, J. T. Maze and C. C. Jarrold, *J. Phys. Chem. A*, 2006, **110**, 2157–2164.
- Y. Yang, Y.-K. Li, Y.-X. Zhao, G.-P. Wei, Y. Ren, K. R. Asmis and S.-G. He, *Angew. Chem., Int. Ed.*, 2021, **60**, 13788–13792.
- Y.-X. Zhao, X.-N. Li, Z. Yuan, Q.-Y. Liu, Q. Shi and S.-G. He, *Chem. Sci.*, 2016, **7**, 4730–4735.

- 20 Y.-X. Zhao, Q.-Y. Liu, M.-Q. Zhang and S.-G. He, *Dalton Trans.*, 2016, **45**, 11471–11495.
- 21 K. Angermund, M. Bühl, E. Dinjus, U. Endruschat, F. Gassner, H.-G. Haubold, J. Hormes, G. Köhl, F. T. Mauschick and H. Modrow, *et al.*, *Angew. Chem., Int. Ed.*, 2002, **41**, 4041–4044.
- 22 O. Bartlewicz, M. Jankowska-Wajda and H. Maciejewski, *RSC Adv.*, 2019, **9**, 711–720.
- 23 M. A. Bernd, E. B. Bauer, J. Oberkofler, A. Bauer, R. M. Reich and F. E. Kühn, *Dalton Trans.*, 2020, **49**, 14106–14114.
- 24 A. M. Borys and E. Hevia, *Angew. Chem., Int. Ed.*, 2021, **60**, 24659–24667.
- 25 J. A. Brozik, B. L. Scott and B. I. Swanson, *Inorg. Chim. Acta*, 1999, **294**, 275–280.
- 26 Á. Díez, J. Fernández, E. Lalinde, M. T. Moreno and S. Sánchez, *Dalton Trans.*, 2008, 4926–4936, DOI: [10.1039/B806572A](https://doi.org/10.1039/B806572A).
- 27 G. C. Fortman, N. M. Scott, A. Linden, E. D. Stevens, R. Dorta and S. P. Nolan, *Chem. Commun.*, 2010, **46**, 1050–1052.
- 28 A. Huffer, B. Jeffery, B. J. Waller and A. A. Danopoulos, *C. R. Chim.*, 2013, **16**, 557–565.
- 29 M. Kolter, K. Böck, K. Karaghiosoff and K. Koszinowski, *Angew. Chem., Int. Ed.*, 2017, **56**, 13244–13248.
- 30 S. Martínez-Salvador, B. Menjón, J. Forniés, A. Martín and I. Usón, *Angew. Chem., Int. Ed.*, 2010, **49**, 4286–4289.
- 31 T. Ogawa, M. Yoshida, H. Ohara, A. Kobayashi and M. Kato, *Chem. Commun.*, 2015, **51**, 13377–13380.
- 32 F. Schroeter and T. Strassner, *Inorg. Chem.*, 2018, **57**, 5159–5173.
- 33 S.-y Takizawa, R. Kano, N. Ikuta and S. Murata, *Dalton Trans.*, 2018, **47**, 11041–11046.
- 34 D. T. Weiss, P. J. Altmann, S. Haslinger, C. Jandl, A. Pöthig, M. Cokoja and F. E. Kühn, *Dalton Trans.*, 2015, **44**, 18329–18339.
- 35 S. Ye, W. Kaim, M. Albrecht, F. Lissner and T. Schleid, *Inorg. Chim. Acta*, 2004, **357**, 3325–3330.
- 36 M. Yoshida and M. Kato, *Coord. Chem. Rev.*, 2020, **408**, 213194.
- 37 H. S. Yu, X. He, S. L. Li and D. G. Truhlar, *Chem. Sci.*, 2016, **7**, 5032–5051.
- 38 T. H. Dunning, *J. Chem. Phys.*, 1989, **90**, 1007–1023.
- 39 R. A. Kendall, T. H. Dunning and R. J. Harrison, *J. Chem. Phys.*, 1992, **96**, 6796–6806.
- 40 N. B. Balabanov and K. A. Peterson, *J. Chem. Phys.*, 2005, **123**, 064107.
- 41 D. Figgen, K. A. Peterson, M. Dolg and H. Stoll, *J. Chem. Phys.*, 2009, **130**, 164108.
- 42 K. A. Peterson, D. Figgen, M. Dolg and H. Stoll, *J. Chem. Phys.*, 2007, **126**, 124101.
- 43 H.-J. Werner, P. J. Knowles, F. R. Manby, J. A. Black, K. Doll, A. Heßelmann, D. Kats, A. Köhn, T. Korona and D. A. Kreplin, *et al.*, *J. Chem. Phys.*, 2020, **152**, 144107.
- 44 D. Figgen, K. A. Peterson, M. Dolg and H. Stoll, *J. Chem. Phys.*, 2009, **130**, 164108.
- 45 K. A. Peterson, D. Figgen, M. Dolg and H. Stoll, *J. Chem. Phys.*, 2007, **126**, 124101.
- 46 K. Raghavachari, G. W. Trucks, J. A. Pople and M. Head-Gordon, *Chem. Phys. Lett.*, 1989, **157**, 479–483.
- 47 R. J. Bartlett, J. D. Watts, S. A. Kucharski and J. Noga, *Chem. Phys. Lett.*, 1990, **165**, 513–522.
- 48 M. J. Frisch, G. W. Trucks, H. B. Schlegel, G. E. Scuseria, M. A. Robb, J. R. Cheeseman, G. Scalmani, V. Barone, G. A. Petersson and H. Nakatsuji, *et al.*, *Gaussian 16 Rev. B.01*, Wallingford, CT, 2016.
- 49 Z. J. Jain, P. S. Gide and R. S. Kankate, *Arabian J. Chem.*, 2017, **10**, S2051–S2066.
- 50 W. M. Haynes, *CRC Handbook of Chemistry and Physics*, Taylor & Francis, 93rd edn, 2012.
- 51 E. D. Glendening, J. K. Badenhoop, A. E. Reed, J. E. Carpenter, J. A. Bohmann, C. M. Morales, P. Karafiloglou, C. R. Landis and F. Weinhold, *NBO 7.0*. Theoretical Chemistry Institute: University of Wisconsin, Madison, 2018, <https://nbo6.chem.wisc.edu/>, accessed May 13, 2022.
- 52 E. D. Glendening, C. R. Landis and F. Weinhold, *J. Comput. Chem.*, 2019, **40**, 2234–2241.
- 53 S. Kozuch, *Wiley Interdiscip. Rev.: Comput. Mol. Sci.*, 2012, **2**, 795–815.
- 54 S. Kozuch and S. Shaik, *Acc. Chem. Res.*, 2011, **44**, 101–110.
- 55 J. A. Varela, S. A. Vázquez and E. Martínez-Núñez, *Chem. Sci.*, 2017, **8**, 3843–3851.
- 56 S. Hoops, S. Sahle, R. Gauges, C. Lee, J. Pahle, N. Simus, M. Singhal, L. Xu, P. Mendes and U. Kummer, *Bioinformatics*, 2006, **22**, 3067–3074.

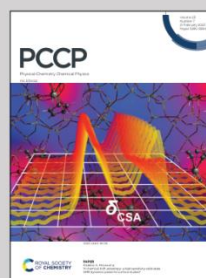


**Showcasing research from the Group of
Prof. Evangelos Miliordos at Auburn University, USA**

Transition metal oxide complexes as molecular catalysts for selective methane to methanol transformation: any prospects or time to retire?

This article discusses strategies for selective partial oxidation of methane to methanol. The proposed ideas are based on recent literature findings and our ongoing computational work on molecular catalysis. The use of metal oxide anionic complexes offers small metal-methanol binding energies giving the opportunity for the solvent to remove methanol fast from the catalyst. Another direction is using metal oxide dications with ligands that form hydrogen bonds with methanol, which increases the activation barrier of methanol oxidation.

As featured in:



See Evangelos Miliordos *et al.*,
Phys. Chem. Chem. Phys.,
2023, **25**, 5313.



Cite this: *Phys. Chem. Chem. Phys.*,
2023, 25, 5313

Transition metal oxide complexes as molecular catalysts for selective methane to methanol transformation: any prospects or time to retire?

Emily E. Claveau,¹ Safaa Sader, Benjamin A. Jackson,² Shahriar N. Khan and Evangelos Miliordos^{1*}

Transition metal oxides have been extensively used in the literature for the conversion of methane to methanol. Despite the progress made over the past decades, no method with satisfactory performance or economic viability has been detected. The main bottleneck is that the produced methanol oxidizes further due to its weaker C–H bond than that of methane. Every improvement in the efficiency of a catalyst to activate methane leads to reduction of the selectivity towards methanol. Is it therefore prudent to keep studying (both theoretically and experimentally) metal oxides as catalysts for the quantitative conversion of methane to methanol? This perspective focuses on molecular metal oxide complexes and suggests strategies to bypass the current bottlenecks with higher weight on the computational chemistry side. We first discuss the electronic structure of metal oxides, followed by assessing the role of the ligands in the reactivity of the catalysts. For better selectivity, we propose that metal oxide anionic complexes should be explored further, while hydrophylic cavities in the vicinity of the metal oxide can perturb the transition-state structure for methanol increasing appreciably the activation barrier for methanol. We also emphasize that computational studies should target the activation reaction of methanol (and not only methane), the study of complete catalytic cycles (including the recombination and oxidation steps), and the use of molecular oxygen as an oxidant. The titled chemical conversion is an excellent challenge for theory and we believe that computational studies should lead the field in the future. It is finally shown that bottom-up approaches offer a systematic way for exploration of the chemical space and should still be applied in parallel with the recently popular machine learning techniques. To answer the question of the title, we believe that metal oxides should still be considered provided that we change our focus and perform more systematic investigations on the activation of methanol.

Received 23rd November 2022,
Accepted 10th January 2023

DOI: 10.1039/d2cp05480a

rsc.li/pccp

1. Introduction

Natural gas has become a major hydrocarbon source in recent years. It is extracted in large quantities from petroleum wells (is burned and released into the atmosphere)^{1,2} or from fracking.³ The utilization of natural gas is a topic of intense research because it can be used as a fuel or a building block for the synthesis of larger organic molecules, while its main component (methane) is a very potent greenhouse gas (25 times more potent than carbon dioxide) and its release or combustion harms the Earth's atmosphere. Functionalization of methane is an important initial step for its utilization. A direct process under mild conditions will enable a commercially viable and eco-friendly path for the exploitation of this abundant carbon

feedstock. The importance of methane utilization and the historical background of the early and more recent attempts to activate methane are given in more detail in ref. 4 and 5. The insertion of an oxygen atom between one of the C–H bonds, *i.e.* conversion of methane to methanol, seems to be the most promising option. Methanol economy is a term coined twenty years ago with the hope of soon finding an efficient way to produce large quantities of methanol, not only from methane but also from other carbon sources such as CO₂.^{6–8}

Methanol is a key molecule for multiple reasons.⁹ It is liquid under ambient conditions and can be transported in conventional tanker vehicles, whereas energy intensive liquefaction techniques are necessary for the transportation of methane as LNG (liquefied natural gas). The boiling point of methanol is 64.7 °C in contrast to methane at –161.6 °C.¹⁰ In addition, methanol has a competitive thermal content and is a greener fuel compared to gasoline.¹¹ Finally, methanol has a variety of

Department of Chemistry and Biochemistry, Auburn University, Auburn, AL 36849-5312, USA. E-mail: emiliord@auburn.edu

industrial applications, for example its use as a solvent or as a raw material in the production of formaldehyde, acetic acid, ethers, alkenes, and amino acids.^{5,12,13}

Therefore, the ideal solution would be a direct (one-step) conversion of methane to methanol under mild conditions that can be applied at the location of the natural gas extraction. Industrially, this conversion occurs under harsh conditions involving the intermediate production of syngas (a mixture of carbon monoxide and molecular hydrogen) followed by the Fischer–Tropsch process.¹⁴ This is economically feasible only at large scale and in specialized facilities. Several laboratory techniques (homogeneous catalysis, heterogeneous catalysis and biological systems) have been proposed or developed for this goal. Metal-oxide surfaces,^{15–17} metal exchanged zeolites,^{18–21} metal organic frameworks (MOF),^{22–24} metal-doped graphene sheets,²⁵ photocatalysts,^{26,27} enzymes/biocatalysts,²⁸ enzyme embedded materials,²⁹ electrochemical devices,² and other less conventional methods, such as plasma technologies, membrane reactors, solar reactors, and supercritical fluids, are reported in the literature.^{30,31}

Despite the extensive efforts, an efficient partial oxidation of methane to methanol in high yields has not reached commercialization yet. The major bottleneck is not converting methane to methanol but doing so in a selective manner. The C–H bonds of methanol are weaker than methane and can be further oxidized leading to side products. Both experimental data and theoretical calculations indicate that no matter which catalyst (molecular or heterogeneous) is used, the activation barrier for methanol is always lower than methane and that improvement in conversion rates occurs at the expense of selectivity.^{5,32} Regarding metal-exchanged zeolites, additional complications include diffusion limitations in confined chemical environments and the identification of the catalytically active form (metal-oxo terminal or bridged structures). Higher methanol yields are given by metal exchanged zeolites with small pores,¹⁹ with Fe and Cu exchanged zeolites being the better performing systems.²⁰ MOFs have higher metal loading and were recently used for CH activation,^{22–24} but they also have diffusion limitations.²⁴ Photocatalysts are used to functionalize strong C–H bonds of specific carbon atoms,²⁶ including methane,²⁷ but little effort has been made in the selective production of methanol. The most successful strategy achieving high selectivity and high yield is protecting OH of methanol as OSO₃H and deprotecting the OH group as needed. This multi-step process facilitated by a platinum molecular complex was developed by Periana and co-workers more than ten years ago,³³ but has found no industrial applications because of the difficult catalyst recovery and high cost.

Theory has also played a significant role in our understanding focusing primarily on the methane activation process (selectivity studies are sparse).³⁴ The appropriate type of calculations and their difficulties for these systems are reviewed in the literature.^{35,36} Many studies focus on the reactivity of iron–oxo species inspired by the structure of methane monooxygenases.^{37,38} The haem–iron complex in these enzymes adopt the highly

reactive quintet oxyl state of the iron–oxo unit, unlike the laboratory synthesized mimic complexes (see ref. 39 and 40, and references therein). The latter generally prefer the less reactive triplet state (but see ref. 41) and the activation of methane happens *via* the intervention of the quintet state in the transition state region (two-state reactivity).^{39,40,42} In terms of electronic structure, the mechanism becomes more complex if we consider the σ and π reaction paths.^{39,40,43} Machine learning techniques have recently been exploited in an attempt to provide correlations between the different factors,⁴⁴ with a recent study questioning the accepted principle that high spin iron–oxo units offer the best performance.⁴⁵ Finally, a new mechanism (involving metal methoxy groups) was identified recently in iron MOF species offering an alternative path for protection of the produced methanol.⁴⁶

In almost all the catalytic systems used so far some metal–oxygen unit (even as a transient intermediate) is the common chemically active component. The issue of non-selective oxidation has shifted efforts towards the search for a catalyst which will quickly release methanol from the catalytic site.³² To this direction, there are two novel ideas in the literature for both homogeneous and heterogeneous catalysts. Molecular catalysts are designed to create a non-friendly environment for methanol by creating hydrophobic cavities around the catalytic (vanadyl, VO²⁺) center.⁴⁷ Heterogeneous electrocatalytic techniques aim to change the electrochemical potential accordingly during the reaction.² None of these solutions had the desired performance. In response, the use of molecular metal oxide anionic species has been proposed based on quantum mechanical calculations.^{48,49} In this case, methanol interacts with a negatively charged metal center with which it binds only weakly. More details for this “molecular electrocatalysis” process are presented later. In addition, the replacement of the hydrophobic with hydrophilic cavities is suggested presently.

In the text below, we start by providing a critical overview of the electronic structure of transition metal monoxides with various charges (oxidation states of the metal), and the effect of the ligands in adjusting their electronic structure. The C–H bond activation mechanisms employed by metal oxides and aspects on their efficiency and selectivity are then discussed. Finally, we summarize our thoughts and suggestions for future avenues. We post that it is still too early to retire metal oxides as methane-to-methanol catalysts as several strategies remain and have been proposed to overcome the present shortcomings. We also show that a systematic theoretical bottom-up approach, where bare metal oxides are studied first and then ligands are added in a step-wise manner, is viable and provides a road map for development and invaluable insights towards the discovery of a practical catalytic system. In the remaining text, the [M] and [O] notation is used to represent ligated metal complexes and molecular oxidants, respectively. Some calculations performed presently were done at the DFT/MN15 and CASSCF levels of theory using Gaussian16 and MOLPRO2015,^{50–52} respectively, using correlation consistent basis sets.^{53–57} The exact details are mentioned in every case.

2. Electronic structure of bare metal monoxides

The metal oxide complexes are used for a plethora of reactions and are often present in enzymatic systems usually as MO^{2+} . An initial interesting question is why has nature selected these species? What is special about doubly charged metal oxides? Previous high level quantum chemical work^{58–71} on the electronic structure of MO^- , MO^0 , MO^+ , and MO^{2+} revealed that MO^{2+} species are the only ones bearing ground or low energy states with a radical character on the oxygen terminus in energetic proximity to states with a closed-shell oxygen center. The co-existence of the two forms gives flexibility and one or the other form can be stabilized with appropriate ligands and wise choice of metal.

Specifically, a neutral or charged metal oxide, MO^{n+} , adopts two electronic structure representations depending on the presence or absence of an unpaired electron on the oxygen terminus. The $\text{M}^{(n+2)+}\text{O}^{2-}$ oxo form indicates an electron rich closed-shell oxygen center, whereas in the $\text{M}^{(n+1)+}\text{O}^{\bullet-}$ oxyl form oxygen is missing an electron and bears a radical character. At this point, it should be stressed that the commonly used $\text{M}=\text{O}$ picture is often misleading (see also below). To investigate the relative stability of these two forms, we start from the parent fragments $\text{M}^{(n+2)+} + \text{O}^{2-}$ and $\text{M}^{(n+1)+} + \text{O}^-$. The latter is always lower in energy and their separation is determined by the ionization energy (IE) of the metal ($\text{M}^{(n+1)+}$ to $\text{M}^{(n+2)+}$). The O^{2-} ion is unstable with respect to O^- (negative electron affinity, EA).¹⁰ The energy required to go from the oxyl to the oxo fragments, IE-EA ($\text{EA} < 0$), is proportional to the square of the metallic charge, as can be observed by the experimental values¹⁰ and inferred by the hydrogenic model.

Fig. 1(a) depicts graphically the formation of the two equilibrium $\text{M}^{(n+2)+}\text{O}^{2-}$ and $\text{M}^{(n+1)+}\text{O}^{\bullet-}$ structures from the corresponding fragments. Both are stabilized with respect to the fragments by both electrostatic (ΔE_{elc}) and covalent chemical bonding (ΔE_{covb}) factors. An indication of the stronger binding in oxo systems is their shorter bond lengths. Assuming no charge transfer during the bond formation, the electrostatic

terms are given by $E_{\text{elc}}(\text{oxo}) = (n+2) \times (-2)/r_{\text{MO}}$ and $E_{\text{elc}}(\text{oxyl}) = (n+1) \times (-1)/r_{\text{MO}}$, and thus $\Delta E_{\text{elc}} = E_{\text{elc}}(\text{oxo}) - E_{\text{elc}}(\text{oxyl}) = -(n+3)/r_{\text{MO}}$ is a linear function of total charge n . Overall, the energy required for the formation of oxo fragments increases faster ($\sim n^2$) than the energy gained during the formation of the equilibrium structure ($\sim n^1$). For the sake of simplicity, we neglect the ΔE_{covb} and EA terms, which cancel each other (at least partially). The plot of Fig. 1(b) shows the energy required (IE) and gained (ΔE_{elc} , $r_{\text{MO}} = 1.6 \text{ \AA}$) going from $\text{Fe}^{(n+1)+}\text{O}^{\bullet-}$ to $\text{Fe}^{(n+2)+}\text{O}^{2-}$. The left region in light blue is oxo dominated ($\Delta E_{\text{elc}} > \text{IE}$), whereas the right region in light orange is oxyl-dominated ($\Delta E_{\text{elc}} < \text{IE}$). The $n = 2$ appears to be the onset for ground state oxyl species.

Despite the approximations taken, this model reveals that there is some overall charge n of MO^{n+} , where the relative magnitudes of the necessary energy for the $\text{M}^{(n+1)+} \rightarrow \text{O}^{\bullet-}$ electron transfer and the energy gained by the subsequent formation of $\text{M}^{(n+2)+}\text{O}^{2-}$ switch. This gives flexibility for the MO^{n+} species to adjust their electronic structure (and hence their reactivity) *via* an appropriate combination of ligand molecules and metal identity. The turning point appears to be generally $n = 2$, but can be $n = 0$ or 1 for the late transition metals due to their larger ionization energies. Experimentally, this turning point for iron has been observed *via* the reactivity enhancement going from FeO^+ to FeO^{2+} .⁷² Finally, higher positive charges ($n \geq 3$) definitely favor the oxyl form.

Below we examine in more detail the electronic structure of metal oxides starting from neutral followed by cationic, dicationic, and anionic species. Typical molecular orbitals of bare first-row transition metal monoxides are shown in Fig. 2. The left/right columns correspond to VO/NiO as representatives of early/late transition metals. This valence space can be divided in non-bonding, bonding, and anti-bonding orbitals. The bonding ones include the σ_{MO} orbital, which is created by the constructive superposition of the $2p_z$ of oxygen and $3d_z^2$ of the metal, and two π_{MO} resulting from the constructive superposition of the $2p_{x,y}$ of oxygen and $3d_{xz,yz}$ of the metal. These orbitals are clearly polarized towards oxygen for the early transition metals. The anti-bonding orbitals (π_{MO}^* and σ_{MO}^*)

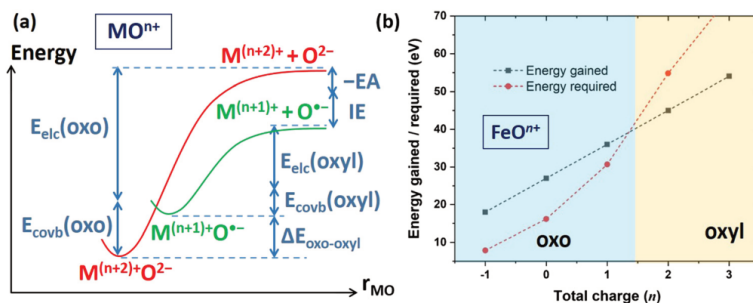


Fig. 1 (a) Representative potential energy curves and energy decomposition for the formation of the oxo [$\text{M}^{(n+2)+}\text{O}^{2-}$] and oxyl [$\text{M}^{(n+1)+}\text{O}^{\bullet-}$] forms of MO^{n+} . (b) Energy gained (ΔE_{elc}) and required (IE) for the transformation of the oxyl form to oxo in FeO^{n+} ; see the text. The light blue/orange regions correspond to oxo/oxyl-dominated species.

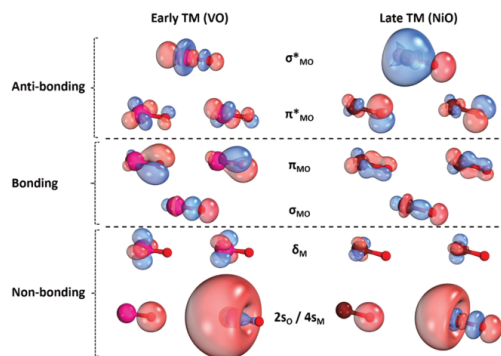


Fig. 2 Typical molecular orbitals for early (here VO) and late (here NiO) transition metal oxides.

are the result of the destructive combinations of the same atomic orbitals. Polarization in the opposite direction is observed for anti-bonding orbitals: the π_{MO}^* are now polarized towards the metal/oxygen for early/late transition metals. The non-bonding ones include the 2s of oxygen ($2s_{\text{O}}$), the 4s of the metal ($4s_{\text{M}}$) polarized away from oxygen as result of its orthogonality with the bonding σ_{MO} orbital. Identical polarization has been observed for metal ammonia complexes, where the lone pair of ammonia pushes away $4s_{\text{M}}$.⁷³ The last two orbitals are pure metallic (δ_{M}) as they have zero overlap with the valence orbitals of oxygen.

The three bonding orbitals are all doubly occupied in the ground state electronic configuration of all neutral species ($\sigma_{\text{MO}}^2\pi_{\text{MO}}^4$) indicating three covalent metal–oxygen bonds. However, the strong polarization of these orbitals for the early transition metals suggests rather an ionic $\text{M}^{2+}\text{O}^{2-}$ picture. For the first three metals, the remaining valence electrons populate the non-bonding orbitals ($4s_{\text{M}}^1, 4s_{\text{M}}^1\delta_{\text{M}}^1, 4s_{\text{M}}^1\delta_{\text{M}}^2$ for ScO, TiO, and VO).^{58,59} These electrons screen only minimally the metallic charge experienced by the $\sigma_{\text{MO}}^2\pi_{\text{MO}}^4$ electrons. Ideally, going from Sc to Ti and V the effective charge is 3+, 4+, and 5+ leading to a contraction of the bond length from 1.668 Å (ScO; $\text{X}^2\Sigma^+$), to 1.623 Å (TiO; $\text{X}^3\Delta$) and 1.592 Å (VO; $\text{X}^4\Sigma^-$).⁷⁴ Conclusively, the $\text{M}^{2+}\text{O}^{2-}$ description is fair for MO^0 (M = Sc, Ti, V), and the commonly used $\text{M}=\text{O}$ picture (implying a double metal–oxygen bond) is generally inaccurate ($\text{M}\equiv\text{O}$ would be more appropriate). Moving to CrO and MnO, the additional electrons go to π_{MO}^* causing elongation of the bonds to 1.613 (CrO; $\text{X}^5\Pi$) and 1.648 Å (MnO; $\text{X}^6\Sigma^+$). If we consider that $\pi_{\text{MO}}^* \sim \pi 3d_{xz}$, we can still suggest a $\text{Cr}^{2+}\text{O}^{2-}/\text{Mn}^{2+}\text{O}^{2-}$ picture. The additional electrons for the next metals populate sequentially the δ_{M} (FeO; $\text{X}^5\Delta$), the $4s_{\text{M}}$ (CoO; $\text{X}^4\Delta$) and δ_{M} (NiO; $\text{X}^3\Sigma^-$)^{60–62} non-bonding orbitals leaving the bond lengths practically unaffected 1.619, 1.631, and 1.631 Å.⁷⁴ Given that the last two metal oxides have a $(4s_{\text{M}}\delta_{\text{M}})^{5,6}\sigma_{\text{MO}}^2\pi_{\text{MO}}^4\pi_{\text{MO}}^{+2}$ configuration with $\pi_{\text{MO}}^* \sim 2p_{xy}$, the terminal oxygen has a strong radical nature (oxyl character). FeO is somewhere in the middle making iron–oxygen a versatile

bond balancing between oxo and oxyl. The cationic metal monoxides follow similar trends: ScO^+ has a $\sigma_{\text{MO}}^2\pi_{\text{MO}}^4$ configuration, and the additional electrons populate δ_{M} (TiO^+), δ_{M} (VO^+), $4s_{\text{M}}$ (CrO^+), π_{MO}^* (MnO^+ combined with a concomitant $\pi_{\text{MO}} \rightarrow \pi_{\text{MO}}^*$ electron promotion), π_{MO}^* (FeO^+), δ_{M} (CoO^+), and δ_{M} (NiO^+).^{58–62} Overall, both neutral and cationic first-row transition metal monoxides show a strong oxo character for early metals which gradually converts to oxyl for the late metals.

Despite the importance of the dicationic species, only recently a systematic high-level study appeared in the literature providing potential energy curves, wavefunction information, and spectroscopic constants for several electronic states.⁷⁰ These systems can be clearly categorized into three groups, the early transition metals (Ti, V, Cr) with well separated oxo ground states, the middle transition metals (Mn, Fe) with oxyl ground states but low-lying oxo excited states, and the late transition metals (Co, Ni, Cu) with clear oxyl ground and excited states. The dominant configuration of the ground state of TiO^{2+} is $\sigma_{\text{MO}}^2\pi_{\text{MO}}^4$ resembling ScO^+ . ScO^{2+} is necessarily oxyl species owing to that scandium has only three valence electrons [$\text{ScO}^{2+} = \text{ScO}^+(\text{X}^1\Sigma^+) - 1e^- = \text{Sc}^{3+}\text{O}^{2-} - 1e^- = \text{Sc}^{3+}\text{O}^{\bullet-}$], while going to VO^{2+} and CrO^{2+} the additional electrons populate the δ_{M} orbitals. The oxo states of MnO^{2+} and FeO^{2+} bear one and two π^* electrons, respectively, but they are higher in energy than the oxyl states. This stabilization of the oxyl states going from VO^{2+} to FeO^{2+} explains the different reactivity of the two species as confirmed recently with machine learning studies.⁷⁵ The oxyl states of MnO^{2+} , FeO^{2+} , and the remaining metal oxides are of strong multi-reference character. A similar systematic analysis for second row metals has not appeared in the literature, but sporadic studies indicate that they favor low-spin states with a dominant oxo character. For example, MoO^{2+} is identical to CrO^{2+} ($\sigma_{\text{MO}}^2\pi_{\text{MO}}^4\delta_{\text{M}}^2$),⁶⁴ whereas RuO^{2+} prefers $\sigma_{\text{MO}}^2\pi_{\text{MO}}^4\delta_{\text{M}}^4(1\Sigma^+)^{65}$ instead of $\sigma_{\text{MO}}^2\pi_{\text{MO}}^4\delta_{\text{M}}^2\pi_{\text{MO}}^2(\text{FeO}^{2+}; ^3\Delta)$, and RhO^{2+} prefers $\sigma_{\text{MO}}^2\pi_{\text{MO}}^4\delta_{\text{M}}^4\pi_{\text{MO}}^2(2\Pi)^{71}$ over $\sigma_{\text{MO}}^2\pi_{\text{MO}}^4\delta_{\text{M}}^2\pi_{\text{MO}}^2\sigma_{\text{MO}}^1(\text{CoO}^{2+}; ^6\Sigma^+)$.

A final comment pertains to the $4s_{\text{M}}$ electrons. The low-lying electronic states of transition metal atoms have either a doubly or singly occupied $4s_{\text{M}}$ orbital. The lowest energy $4s_{\text{M}}^0$ states are considerably higher in energy ranging between 1.71 eV for Ni and 6.41 eV for Mn (M_J -averaged values).⁷⁶ On the other hand, the low-lying electronic states of transition metal cations prefer $4s_{\text{M}}^0$ and $4s_{\text{M}}^1$ states, with the lowest energy $4s_{\text{M}}^2$ states being in the 1.44 (Sc)–6.86 (Mn) eV range (M_J -averaged values).⁷⁶ The exact same trends are observed for metal oxides. The neutral species prefer generally the order $4s_{\text{M}}^1 < 4s_{\text{M}}^2 < 4s_{\text{M}}^0$, and the cationic species $4s_{\text{M}}^0 \sim 4s_{\text{M}}^1 \ll 4s_{\text{M}}^2$.^{58–62} All of the low-lying states of dicationic metal oxide species have $4s_{\text{M}}^0$ configurations, while those of the metal oxide anionic species are of $4s_{\text{M}}^2$ nature. When making MO^- species from MO^0 the additional electron is practically always placed into the $4s_{\text{M}}$ orbital and not on the more electronegative oxygen terminal. The electron affinity (EA) values for the first-row transition metal monoxides range experimentally between 1.22 (CrO) and 1.54 (CoO) eV,^{77–84} which is fortuitously close to the 1.46 eV⁸⁵ EA of the oxygen atom.

Finally, we refer to the destiny of the $4s_M$ electrons upon ligation, which is not discussed in the chemistry textbooks. Ligands, such as water or ammonia, can displace the $4s_M$ electrons from the metal to the periphery of the complex or possibly to the solution,^{67,73} whereas ligands, such as a halide or a second oxygen atom, can elicit these electrons oxidizing the metal–oxygen unit.⁶⁹ The only case that a $4s_M$ electron can survive is in an unsaturated complex of ammonia-like ligands.⁶⁷

3. Ligand effects on the electronic structure

The naturally emerging question is: how do ligands shift the oxo/oxyl balance and hence the reactivity of metal oxygen complexes? The diversity in the electronic structure of the metal–oxygen bond and the variety of metal–ligand interaction types (σ/π -donors/acceptors) make the deduction of general rules an extremely difficult task. This Gordian knot has been the main focus of the recent machine-learning-based studies in order to identify the key geometric and electronic parameters that determine the reactivity of these species.⁴⁴

In a bottom-up approach, the deconvolution of the important factors can be achieved *via* the step-wise strategy of first exploring the electronic structure of metal–oxygen units and then adding one ligand molecule at a time. This perspective has been recently explored for some representative systems. It was shown that ammonia and water ligands stabilize the oxo form of FeO^{2+} over the oxyl form.³⁹ The addition of solely one ammonia or water ligand indicated that ammonia stabilizes the oxo form more than water, which was confirmed for mixed (water/ammonia) penta- and hexa-coordinated species, suggesting that strong ligand fields favor oxo over oxyl. Experimentally, this conclusion was confirmed by coordinating penta-dentate ligands around the FeO^{2+} unit. The ligands are anchored with σ -donating nitrogen atoms and the ligand field was modulated by increasing the volume of side-units of the ligands.⁸⁶ The bulkier ligands elongated the Fe–N bonds weakening the ligand field, increasing the radical character of the iron–oxygen unit, and thus enhancing the C–H activation rates.

On the other hand, the stabilization of oxyl states can be managed by adding hydrogen atoms, halides or other electron engaging (or withdrawing) ligands, such as a second oxygen atom. The potential energy curves of three hydrogen atoms approaching ZrO revealed that they can stabilize the higher energy $\text{Zr}^3(5s_{Zr}^1\delta^2)\text{O}^{\bullet-}$ ($^3\Pi$) electronic states more than the ground $\text{X}^3\Delta\text{Zr}^{2+}(5s_{Zr}^1\delta^1)\text{O}^{2-}$ state.⁶⁹ The oxo/oxyl energy gap for ZrO ($^3\Delta/{}^3\Pi$) is $78.5\text{ kcal mol}^{-1}$ at the MN15/aug-cc-pVDZ(O,H)/aug-cc-pVDZ-PP(Zr) level of theory (present calculations). The addition of the first and second hydrogen atoms decrease this gap only slightly to 76.1 and $67.4\text{ kcal mol}^{-1}$, respectively. However, the addition of the third hydrogen makes the difference by eliminating the oxo form. H_2ZrO is a closed-shell oxo species with no unpaired electron on the Zr site to accommodate a third Zr–H bond in contrast with the open shell H_2ZrO triplet oxyl state (one electron is on Zr and one on

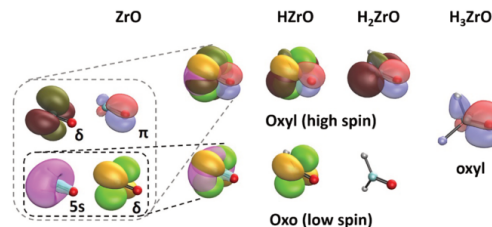


Fig. 3 Singly occupied orbitals for the low spin oxo and high spin oxyl states of H_nZrO , $n = 0-3$. The addition of each hydrogen atom leads to deletion of one unpaired electron. The $5s^1$ electron vanishes first. The three unpaired electrons of ZrO/oxyl localized on the metal ($5s^1, \delta^2$) transform gradually to the three Zr–H bonding orbitals, while the π electron remains intact until the formation of H_3ZrO . ZrO/oxo has only two metallic electrons ($5s^1, \delta^1$) and can only form H_2ZrO .

O). The H_3ZrO ground state has a clear $\text{O}(2p^1)$ configuration disclosing its ZrO ($^5\Pi/\text{oxyl}$) ancestry.⁶⁹ Fig. 3 provides a pictorial view of the $\text{ZrO} \rightarrow \text{H}_3\text{ZrO}$ transformation. The exact same effect was found for F_3ZrO and is anticipated to occur for all halides, oxygen, or other electron withdrawing systems. Each halide can engage one metallic electron,⁶⁹ and oxygen is expected to engage two electrons. In transition metal dioxides, although the two oxygen atoms are generally equivalent, one oxygen atom can be seen as the electron engaging ligand and the other one as the active unit, resulting in a higher oxyl radical character⁸⁷ (compare also the reactivity of the ground and first excited state of TaO_2^+),⁸⁸ and weaker metal–oxygen bonds compared to monoxides.⁸⁹ This picture is in agreement with the abundance of radical oxygen centers in metal polyoxides.⁹⁰⁻⁹³

Overall, the stepwise bottom-up approach provides useful insights for future catalyst design studies. So far, a couple of basic principles are that σ -donors stabilize the oxo configuration, while an appropriate number of σ -electron-engaging ligands favor the oxyl configuration. Future studies should explore the effect of π -donors/acceptors and combinations of all types in a pair-wise manner, before moving to higher coordination numbers and practical molecular catalysts.

4. Efficiency in activating methane

Metal oxides have been observed to react with methane *via* two avenues, the so-called 2+2 addition and the radical mechanism. The electronic structure transformations and typical transition state geometric structures for the two paths are illustrated in Fig. 4. Geometrically, the two transition states differ mainly in the $[\text{M}]-\text{O}-\text{CH}_4$ angle. This angle is obtuse for the radical mechanism and is acute for the 2+2 addition. The 2+2 pathway necessitates that the transition metal oxide complex is not saturated by ligands, while the radical one occurs either as hydrogen atom transfer (HAT) or proton-coupled electron transfer (PCET). For reasons of completeness, it should be mentioned that bridged metal–oxygen bonds (M–O–M) have been shown to be less active.⁹⁴

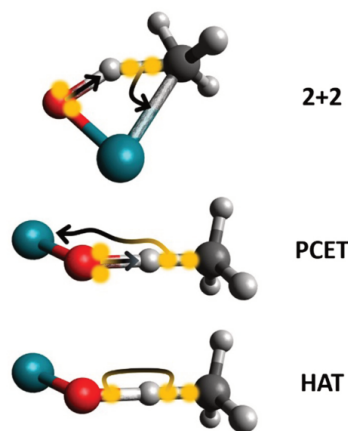


Fig. 4 Typical structures of the transition state for the activation of the H₃C–H bond facilitated by metal oxides via the 2+2, PCET, and HAT mechanisms. Oxygen, carbon, hydrogen, and metal atoms are depicted as red, gray, white, and cyan spheres. The participating electrons and the undergoing electron transfers/spin couplings are shown with yellow spheres and black arrows.

A simplified picture for the 2+2 mechanism involves the “attack” of an electron pair localized on oxygen to hydrogen (see Fig. 4) and the concomitant formation of the M–C bond with the electrons of the cleaved C–H bond. As a result, the hydrogen atom departs from methane as a proton and the methyl group binds to the metal as CH₃[−]. In the PCET mechanism the same proton transfer is accompanied by a transfer of one C–H electron to the metal center. The net outcome is the production of a methyl radical and the reduction of the metal center. On the other hand, the HAT mechanism requires an unpaired electron on the oxygen terminus, which abstracts hydrogen as an atom (and not a proton) releasing a methyl radical. The 2+2 path adopts a heterolytic-type cleavage of the C–H bond, while radical mechanisms (PCET and HAT) proceed with a homolytic-type dissociation.

There are numerous (theoretical and experimental) studies on the reaction of bare neutral and singly positively charged first-row transition metal oxides with methane in the literature.^{95–103} Because of their high oxo character (see above) these systems (neutral and cationic) follow a 2+2 mechanism with C–H activation barriers ranging from 9 (high-spin MnO⁺) to 40 kcal mol^{−1} (with respect to the encounter complex of the reactants) depending on the metal and spin state.^{95–103} The second CH₃–OH fission step (CH₃MOH → M + CH₃OH) has always larger activation barriers than the C–H activation step, but the transition state energy is often lower than the reactants energy enabling the formation of methanol.

At this point, we should make the distinction between gas phase and solution phase reactions. In the latter case the energy of the molecular system can dissipate to solvent molecules trapping the system to the stable CH₃MOH intermediate

and leading to interruption of the catalytic cycle. In a different direction, the inclusion of ligands can destabilize this intermediate.

Reactions of bare metal oxide dications with methane are not found in the literature and have the intrinsic issue that the MO⁺ + CH₄⁺ fragments are lower in energy than MO²⁺ + CH₄, and thus MO²⁺ can ionize methane. The inclusion of a few ligand molecules stabilizes the latter fragments. FeO²⁺ has the lion's share among the reaction studies with methane.^{39,43} Both 2+2 and radical pathways are observed for ligated metal oxide dications.³⁹ It is widely accepted in the literature that the activation energy barriers are considerably smaller for the radical pathways. Counter-examples have been reported recently, where (NH₃)₄RhO²⁺ activates CH₄ via 2+2 with only a 13.6 kcal mol^{−1} barrier.⁷¹ As explained below, this is attributed to the electronic structure transformation of the oxide during the coordination of CH₄.

The RhO²⁺ unit within the (NH₃)₄RhO²⁺ complex retains the electronic structure (2s²σ_{RhO}²π_{RhO}⁴δ_{RhO}⁴π_{RhO}¹) configuration of diatomic RhO²⁺ (see Fig. 2 and 5 for orbital notations and contours). When the four ammonia ligands coordinate, the occupied δ₊ and π_{RhO}^{*} orbitals have minimal amplitude along the Rh–N bonds (see Fig. 5), but the doubly occupied δ_− orbital has a clear anti-bonding σ_{RhN}^{*} character (see Fig. 5).

The incoming CH₄ molecule captures the sixth open coordination site forming the pseudo-octahedral (NH₃)₄(CH₄)RhO²⁺ complex. CH₄ coordinates similarly to ammonia making a dative (coordinative) bond with the electron pair of one H₃C–H bond (see σ_{Rh–CH} ± σ_{Rh–N} orbitals of Fig. 5 and ref. 71). The coordination of CH₄ induces a dramatic electronic structure shift at the metal center. The δ_− orbital is replaced by the second π_{RhO}^{*} orbital and the new configuration (resembling a t_{2g}⁵ configuration under the near-O_h symmetry of the formed complex; see Fig. 5) has no antibonding character along the metal–ligand bonds. Therefore, the five valence electrons of Rh⁴⁺ minimally screen the metal center's charge, exposing the ligands, including CH₄, to a large attractive central positive charge (nucleophilic attack; see Fig. 1 of ref. 33), which “pre-activates” the H₃C–H bond of methane and leads to the unexpectedly small energy barrier. The bond of the coordinated H₃C–H bond is elongated by 0.04 Å compared to isolated CH₄ (1.136 vs. 1.098 Å). In the future, a more efficient “pre-activation” process is expected in systems which can donate electrons from a t_{2g}-like orbital to the antibonding CH orbital (reverse nucleophilic or electrophilic attack; see Fig. 1 of ref. 33).

Overall, CH₄ causes re-organization of the metallic electrons, which in turn induces its efficient activation. To our knowledge, this is the first reported example of metal–substrate cooperativity. Ammonia ligands are often used to keep the computational cost manageable, but for practical applications they are generally replaced by poly-dentate ligands, for example see ref. 86.

Metal mono-oxides with unpaired electrons (non-zero spin density) on oxygen can readily activate methane via HAT forming a metal-hydroxide and releasing a methyl radical (CH₃[•]). As

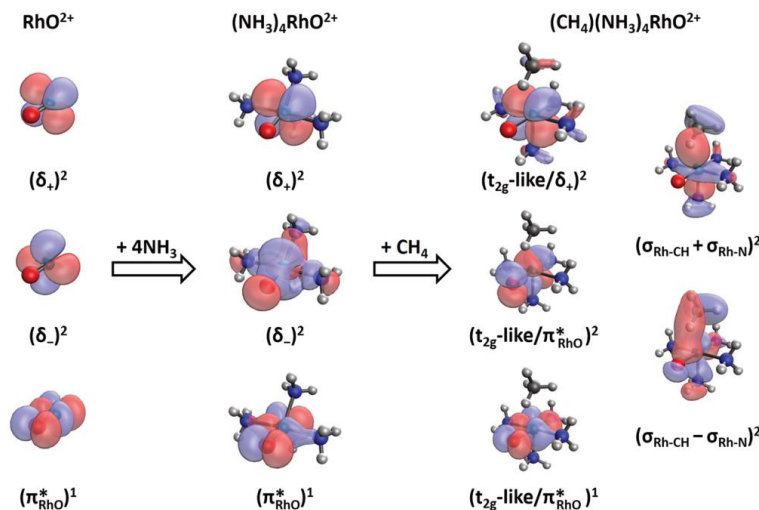


Fig. 5 Contours of select orbitals for RhO^{2+} , $(\text{NH}_3)_4\text{RhO}^{2+}$, and $(\text{CH}_4)(\text{NH}_3)_4\text{RhO}^{2+}$ for their ground states ($S = \frac{1}{2}$) calculated presently at the MN15 level of theory with the cc-pVDZ-PP (for Rh) cc-pVDZ (for N, C, H) aug-cc-pVDZ (for O) basis sets/pseudopotentials. Structures were taken from ref. 71.

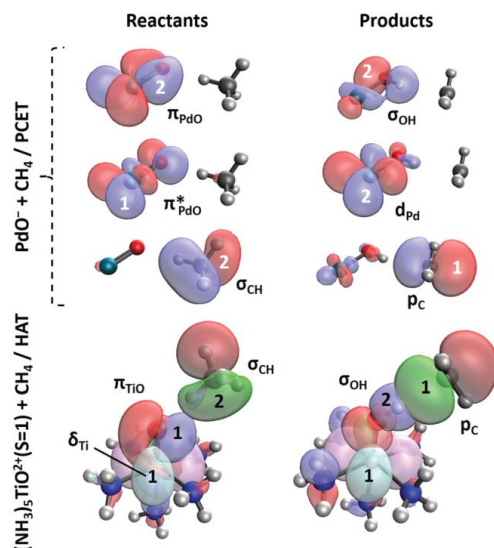


Fig. 6 Select orbitals for the $(\text{NH}_3)_5\text{TiO}^{2+}(\text{triplet}) + \text{CH}_4$ and $\text{PdO}^- + \text{CH}_4$ reactions. The numbers placed on each orbital correspond to their occupancy number. In the case of PdO^- the doubly occupied π_{PdO} orbital takes a proton from CH_4 (σ_{CH}) and becomes σ_{OH} . The π_{PdO} orbital takes an electron from σ_{CH} . The former orbital polarizes towards Pd (d_{Pd}) and the latter becomes a 2p-orbital of carbon (p_{C}). The whole process signifies a PCET mechanism. On the other hand, in the triplet state of $(\text{NH}_3)_5\text{TiO}^{2+}$ the π_{TiO} orbital receives a proton and an electron from σ_{CH} (both depicted as red/blue contours) at the same time signifying a HAT process. The δ_{Ti} electron (cyan/purple contours) remains intact and σ_{CH} turns to p_{C} (both depicted as green/brown contours).

an example, we refer to the first excited state of TiO^{2+} of triplet spin multiplicity for reasons that will become clear later. This state has two unpaired electrons, one in a pure metallic orbital (δ_{Ti}) and one in the π_{TiO} orbital polarized towards oxygen (see Fig. 6) and has been characterized as a $\text{Ti}^{3+}\text{O}^{\bullet-}$ state.⁷⁰ The reaction of this species with CH_4 is spontaneous, *i.e.* no energy barrier is observed (see Fig. 7). The π_{TiO} orbital converts to the σ_{OH} one, and Ti remains in its Ti^{3+} oxidation state.

An example of the PCET mechanism is the reaction of PdO^- with CH_4 . The electronic structure of this oxide has been studied in detail recently,⁶³ and the important feature is that in addition to the σ_{PdO} , π_{PdO} , and Pd-localized orbitals, there is an unpaired electron in a π_{PdO}^* orbital with no clear polarization (see Fig. 2 of ref. 63 and Fig. 6). The π_{PdO}^* orbital is a combination of $4d_{xz}(\text{Pd})$ and $2p_x(\text{O})$. Although this unpaired electron could abstract the H atom from methane, the observed mechanism agrees better with PCET. The π_{PdO} $\sim 2p_x(\text{O}) + 4d_{xz}(\text{Pd})$ orbital is actually grabs H^+ and polarizes towards H^+ , while $\pi_{\text{PdO}}^* \sim 2p_x(\text{O}) - 4d_{xz}(\text{Pd})$ receives an electron from CH_4 and polarizes towards the metal (see Fig. 5 of ref. 104 and Fig. 6). This re-organization of the molecular orbitals clearly showcases a proton transfer to oxygen and an electron transfer to the metal facilitated *via* the π_{PdO}^* orbital. The non-zero spin density (π_{PdO}^*) on oxygen is used not for abstracting the proton but for receiving the electron.

Based on the previous two examples, it is suggested that HAT is promoted by singly occupied π_{MO} orbitals (the possibility of singly occupied σ_{MO} orbital is not excluded; see ref. 39, 40 and references therein), while a $(\pi_{\text{MO}})^2(\pi_{\text{MO}}^*)^1$ configuration initiates PCET.

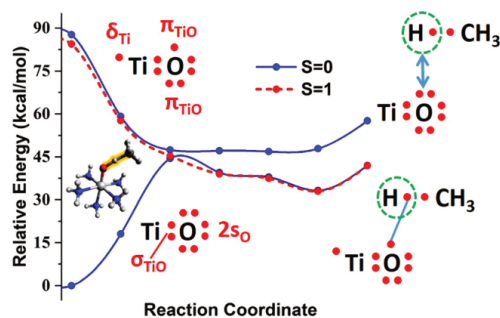


Fig. 7 CASSCF potential energy profiles of the reaction $(\text{NH}_3)_5\text{TiO}^{2+} + \text{CH}_4 \rightarrow (\text{NH}_3)_5\text{TiOH}^{2+} + \text{CH}_3$ for the ground and excited electronic states. Solid blue lines correspond to singlet states and the dashed red line to triplet states. The energy of the reactants corresponds to the left side and that of the products to the right side (see Fig. 6 for their structures). The transition state (shown as inset) is obtained at MN15. The used basis sets are cc-pVDZ (for Ti, C, N, H) aug-cc-pVDZ (for O). The Lewis structures demonstrate the electronic structure of the TiO unit before and after the reaction (ligands are omitted for clarity).

The radical (HAT or PCET) mechanism is also observed for metal oxides with a profound oxo character (no or minimal spin density on oxygen). Especially fully coordinated metal oxides with no physical space for a 2+2 mechanism react *via* HAT/PCET transition states ($[\text{M}]\text{O}-\text{H}-\text{CH}_3$ angle of 180° ; see Fig. 4). From the purely fundamental electronic structure standpoint, the approach of an electronically saturated (closed-shell) oxygen terminus (oxo) with a closed-shell molecule, such as CH_4 , should lead to a repulsive interaction. What is the reason for the observed reactivity? What factors enable oxo species to follow a radical mechanism?

To provide an explanation, the ground singlet-spin state $[(\sigma_{\text{MO}})^2(\pi_{\text{MO}})^4]$ configuration of $(\text{NH}_3)_5\text{TiO}^{2+}$ is employed as a prototype oxo state; denoted as $[\text{Ti}]\text{O}^{2+}$ for simplicity in the rest of the paragraph. Using density functional theory (unrestricted DFT) and specifically the MN15 functional combined with the cc-pVTZ basis set for Ti, N, H, and C, and the aug-cc-pVTZ basis set for O, we located a HAT/PCET-type transition state (see Fig. 7) for the $[\text{Ti}]\text{O}^{2+} + \text{CH}_4$ reaction. Following the normal mode of the imaginary frequency we sampled geometries connecting reactants, $[\text{Ti}]\text{O}^{2+}(\text{CH}_4)$ interaction complex, and products, $[\text{Ti}]\text{OH}^{2+}(\text{CH}_3)$. We then performed CASSCF calculations (with cc-pVDZ basis sets for Ti, N, and H, and aug-cc-pVDZ for C and O) along this reaction coordinate for the two lowest energy singlet states and the first triplet state. The active space chosen consists of 12 orbitals, the $\sigma_{\text{M-O}}$, two $\pi_{\text{M-O}}$, δ_{M} , two $\pi_{\text{M-O}}^*$, $\sigma_{\text{M-O}}^*$, δ_{M}^* , the σ and σ^* of the activated CH bond, and two additional orbitals to allow for appropriate convergence (usually outer p orbitals). The computed potential energy profiles are plotted in Fig. 7. As expected, the potential energy curve pertaining to the ground state of $[\text{Ti}]\text{O}^{2+} + \text{CH}_4$ is purely repulsive and leads to products only after an avoided crossing with the excited singlet state right exactly at the transition state

region. It is also notable that the activation barrier for this reaction is as high as 45 kcal mol^{-1} . Although it is expected to drop when dynamic correlation is included, the value will certainly be higher than the typical barriers of radical mechanisms.

The underlying mechanism in terms of electronic structure is also illustrated in Fig. 7. The excited singlet (open-shell) and triplet states are of identical nature ($\text{Ti}^{3+}\text{O}^{\bullet-}$) with a $(\sigma_{\text{MO}})^2(\pi_{\text{MO}})^3(t_{2g} \sim \delta_{\text{Ti}})^1$ electronic configuration and they react with CH_4 *via* the HAT pathway described earlier: The unpaired π_{MO} electron carries off a hydrogen atom from methane (see the bottom right inset of Fig. 7). On the other hand, the closed-shell ground state fails to make any products (see the top right inset of Fig. 7). The triplet state leads to a triplet $[\text{Ti}]\text{OH}^{2+}(\text{CH}_3)$ product smoothly, while its sibling singlet state undergoes an avoided crossing, conveying its character to the ground singlet state.

Based on the previous analysis, the reaction of $(\text{NH}_3)_5\text{TiO}^{2+}$ with CH_4 to $(\text{NH}_3)_5\text{TiOH}^{2+} + \text{CH}_3^{\bullet}$ can be seen with two ways: (1) starting from the ground state $(\text{NH}_3)_5\text{Ti}^{4+}\text{O}^{2-}$ and going to $(\text{NH}_3)_5\text{Ti}^{3+}\text{OH}^-$ *via* PCET, or (2) starting from the excited state $(\text{NH}_3)_5\text{Ti}^{3+}\text{O}^{\bullet-}$ and going to $(\text{NH}_3)_5\text{Ti}^{3+}\text{OH}^-$ *via* HAT. The second picture is more intuitive and implies that the $\text{H}_3\text{C}-\text{H}$ activation barrier will be lowered if the excited state of the metal oxide is lower. Therefore it provides more information and can explain why some oxides are more efficient than others. This example emphasizes the importance of excited states in “ground-state” chemistry. Transient oxygen radicals are indicative of a two-state reactivity scheme as observed for triplet/quintet states in iron-oxo systems.⁴⁰

The above analysis refers to rather clear-cut cases with clear oxo or oxyl character. In the case of the intermediate/multi-configurational character, all three mechanisms can potentially contribute to the methane activation reaction increasing the complexity of the analysis. In the future, tools that can distinguish the contribution of each pathway will be useful in predicting reactivity and catalytic efficiencies.

5. Selectivity in selective methanol production

The previous discussion focuses on the electronic structure of metal oxide catalysts and the consequences to the activation of a C-H bond of methane. As mentioned in the introduction, the main bottleneck for the selective conversion of methane to methanol is the over-oxidation of the produced methanol. Therefore, computational studies should include energy landscapes for the reaction of the metal oxide catalyst with methanol and not only methane. Nørskov and co-workers did so for numerous metal oxide surfaces and found out that the activation barrier for methanol is consistently lower than that of methane independently of the metal identity.³² The fundamental reasoning provided by the authors is that the C-H bond of methanol is weaker, suggesting that metal oxides are rather inappropriate catalysts and other families must be sought.

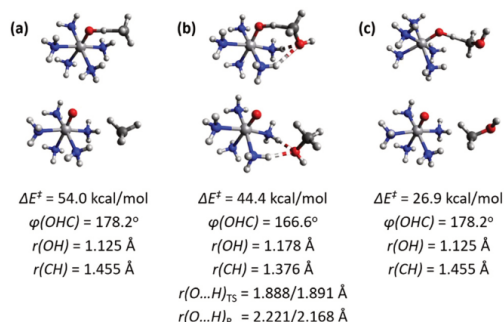


Fig. 8 Structures for the transition states and reacting species for the reaction of $(\text{NH}_3)_5\text{VO}^{2+}$ with methane (a) and methanol (b and c). The structures (c) are not fully optimized, but they are obtained from structures (a) and replacing the most remote H atom of methane with OH. ΔE^\ddagger is the activation energy, $\varphi(\text{OHC})$, $r(\text{OH})$, and $r(\text{CH})$ refer to the angles and distances pertaining to the OCH atoms involved in the methane activation, and $r(\text{O}\cdots\text{H})_{\text{TS/R}}$ corresponds to the O–H distance of the hydrogen bonds at the transition state/reacting species.

The main message of this perspective is to suggest two different approaches to improve the efficiency of metal oxides before their definitive retirement. The first proposal is to design a catalytic system which forces methanol into an orientation unfavorable for CH activation. Presently, a simplistic example refers to the formation of hydrogen bonds but can be generalized for other constrained environments.

The example below refers to the saturated vanadyl ammonia complex $(\text{NH}_3)_5\text{VO}^{2+}$ reacting with CH_4 and CH_3OH . Fig. 8 shows the relative structures for the transition states and corresponding reacting species (encounter complex). The structures of schemes (a) and (b) pertain to fully optimized structures for CH_4 and CH_3OH , respectively. Notice that methanol forms hydrogen bonds with the coordinated ammonia ligands. Scheme (c) corresponds to the reaction with methanol in the absence of hydrogen bonds. These are not fully optimized structures. They are made starting from the structures of CH_4 and replacing the most remote H of CH_4 with OH. Only the positions of the introduced O and H atoms are optimized. The intrinsic activation barriers are 54.0 kcal mol $^{-1}$ for CH_4 and $44.0/26.9$ kcal mol $^{-1}$ for CH_3OH when the hydrogen bonds are present/absent. It turns out that the formation of hydrogen bonds increases the barrier by 17 kcal mol $^{-1}$. During the formation of the transition state both the hydrogen bonds and the proton transfer are disturbed. The $(\text{N})\text{H}\cdots\text{O}(\text{H})$ distances elongate on average by 0.3 Å, while the C–H distance and OHC angle of the transition state decrease by 0.08 Å (1.46 vs. 1.38 Å) and 11° (178° vs. 167°) compared to methane (scheme a) or artificial methanol structures (scheme c).

Although the activation barrier remains lower than that of methane, this example demonstrates that such constrained environments of a rather hydrophilic environment (and not hydrophobic as suggested in the literature for a vanadyl catalyst⁴⁷) can potentially be tuned to disturb the system

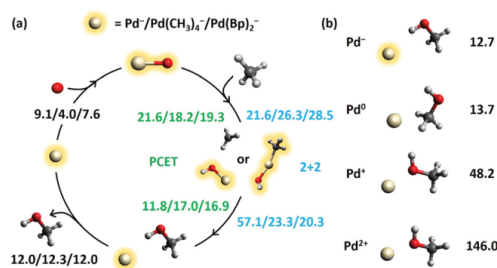


Fig. 9 (a) Catalytic cycle for the reaction $[\text{M}]\text{O}^- + \text{CH}_4 + [\text{O}] \rightarrow [\text{M}]\text{O}^- + \text{CH}_3\text{OH}$. Here $[\text{O}]$ is N_2O , which releases N_2 , and $[\text{M}] = \text{Pd}^-/\text{Pd}(\text{CH}_3)_4^-/\text{Pd}(\text{Bp})_2^-$. Only the structures for $[\text{M}] = \text{Pd}^-$ are shown,¹⁰⁴ but the activation barriers for all three species are listed (blue/green values correspond to 2+2/PCET mechanisms).^{49,104} The bottom left values correspond to the energy required for the release of methanol. (b) Structures and interaction energies for the $\text{Pd}(\text{CH}_3\text{OH})^{2+,+,0,-}$ species calculated presently at the MN15 level of theory (see text). All values are in kcal mol $^{-1}$.

enough so that the activation energy for methanol is at least competitive to that of methane.

A better way to go around the easier activation of methanol is to avoid it. Recently, metal oxide anions have been shown to provide a reasonable bypass. The catalytic cycle is shown in Fig. 9(a) and is the typical cycle reported for metal oxide cations. The main difference making metal oxide anions advantageous is that the negative charge on the metal does not anchor the methanol. Instead, the weak interaction between the metal anion and methanol promotes the diffusion of methanol to the solvent. The same approach has been employed in the literature tuning the electrochemical potential of a metal oxide surface.² The benefit of the molecular anionic metal oxides is that the oxidation state of the metal changes naturally/automatically to the desired state in every step performing “molecular electrocatalysis”. An example demonstrating the range of the interaction energies for different charges is that of Pd^{2+} , Pd^+ , Pd^0 , and Pd^- interactions with methanol, which are 146.0 , 48.2 , 13.7 , and 12.7 kcal mol $^{-1}$ [present calculations at MN15/aug-cc-pVTZ(C,H,O)/aug-cc-pVTZ-PP (Pd)], and only in the anionic and neutral systems the oxygen atom of methanol does not coordinate to the metal, but instead methanol is located further with the OH group pointing to the metal (see Fig. 9(b)).

An immediately obvious challenge for practical applications is how to stabilize an anionic metal center. The electron affinities of the transition metal atoms (taken from ref. 10; see also ref. 105 for computed values) are collected in the periodic table of Fig. 10. The largest electron affinity values correspond to metals of low abundance (Ir, Pt, Au) with probably the best option being nickel, which has an intermediate electron affinity value and high natural abundance. In any case, the identification of ligands that can stabilize the negative charge on the metal is important. Recent calculations found that ligands coordinating with a metal–carbon bond, such as methyl¹⁰⁶ or biphenyl, increase the electron capacity of the

Sc	Ti	V	Cr	Mn	Fe	Co	Ni	Cu	Zn
0.19	0.08	0.53	0.67	N/A	0.15	0.66	1.16	1.24	N/A
Y	Zr	Nb	Mo	Tc	Ru	Rh	Pd	Ag	Cd
0.31	0.43	0.92	0.75	0.55	1.05	1.14	0.56	1.30	N/A
La	Hf	Ta	W	Re	Os	Ir	Pt	Au	Hg
0.47	0.01	0.32	0.82	0.15	1.1	1.56	2.13	2.31	N/A

Fig. 10 Experimental electron affinities for the first, second, and third row transition metals.¹⁰ Mn⁻, Zn⁻, Cd⁻, and Hg⁻ anions are not stable and the electron affinity is not available (N/A). Values in red are below 1.0 eV, values in blue are between 1.0 eV and 1.46 eV (electron affinity of O), and values in green are higher than 1.46 eV.

metal center.⁴⁹ Specifically, the electron affinity of the M(CH₃)₄ species, M = Ni, Pd, Pt, soars to 2.3–2.7 eV and is nearly insensitive to the metal identity (the range for the atoms is 0.6–2.1 eV; see Fig. 10), which makes Ni an excellent candidate for practical applications as the more naturally abundant metal. A different idea is the provision of electrons to the metal in an in-situ and on-demand basis. An example is the weakly bound metal-(π -ring) complexes of Agapie and co-workers.¹⁰⁷

The activation barriers for single and ligated Pd⁻ catalysts for the individual reactions steps are given in Fig. 9(a) as taken from ref. 49 and 104. The values are nearly independent of the catalyst. The CH₃-OH recombination step of the 2+2 path is the only outlier. The 2+2 intermediate is extremely stable and poisons the cycle for bare Pd⁻. Similar observations have been reported for other oxides.^{66,69,87,95,96} However, the addition of methyl or biphenyl ligands ameliorates this issue by destabilizing this intermediate and reducing the activation barriers for the recombination step. This observation highlights the importance of calculating complete cycles and not only the H₃C-H activation step.

Overall, the lessons learned from cationic metal oxides apply for anionic systems too. For example, the two types of mechanisms (PCET, 2+2) are found for anions too. Another interesting observation is that the last oxygen reload step has a near-zero activation barrier for an anion,^{49,104} when using N₂O, generally smaller (certainly not bigger) than neutral and cationic metal oxide units.^{18,34,108–111} For practical applications, it has to be seen if this holds true for O₂. In addition, given the enhanced electron affinities of ligated metal oxide anions, more detailed studies on the electronic structure of the ground and more excited states are necessary for both ligated and diatomic metal oxides. For reasons of completeness, it is mentioned that metal oxide anions have been shown to be superior for other reactions as well, such as water activation reactions.^{64,112}

6. Current challenges and outlook

Tackling the challenge of selectively converting methane to methanol has been a persistent riddle for chemists over the past decades. The inherently weaker C-H bond of methanol prevents catalysts from being selective. Metal oxides or generally metal-oxygen bonds used as facilitators also suffer from this issue. The goal of this perspective is to emphasize that

metal oxides (molecular species) can still be a useful gadget in the chemists toolkit and suggest strategies to circumvent the selectivity traits.

A major shift on the focus of the theoretical studies is the study of methanol activation, and not only methane. A first plan of action is based on perturbing the structure of the methanol transition state. This can be achieved by limiting its mobility and making hydrogen bonds between OH of methanol and constrained environment (such as zeolites or MOFs) or the recently reported molecular cavities around a vanadyl (VO²⁺) unit.⁴⁷ The latter should be modified to include OH or NH dangling units similar to the ones reported for MnO, FeO, CuO, and RuO units.^{113–117}

Along the same lines, another approach would be the design of low coordination complexes which promote a low barrier 2+2 mechanism. These systems would require a closer proximity of methanol and metal center, and this could be avoided by hydrogen bonding or steric effects. The 2+2 mechanism will also prevent the formation of free radicals and the formation of additional byproducts. A strategy for designing low barrier 2+2 mechanisms was proposed recently⁷¹ and involves a “pre-activation” of the C-H bond by exposing the CH bond to large metallic charges. This can be enabled by coupling the metal d-electrons into orbitals that bear small electronic density along the metal-substrate axis. The latter can happen in an “*in situ*” mode during the approach of the substrate to the metal center. Such low-spin complexes are preferably made with second-row transition metals, but future studies should focus on using the more abundant first-row transition metals combined with ligands that impose low spin multiplicity.

A second strategy is the use of metal oxide anions instead of the traditionally used cationic or neutral species. This molecular electrocatalysis process has the advantage that the produced methanol tends to depart from the catalytic center assisting its removal by appropriate solvent molecules. The challenges of stabilizing a negative charge on the metal and enabling a low barrier 2+2 path seem to be addressable *via* the wise selection of ligands. Metal carbon bonds appear to increase the electron affinity of the metal center to values comparable to bare Pt, but there is plenty of unexplored chemical space for further improvement. For industrial applications, promising complexes can be tethered to (chemically inactive) metal surfaces or silica,¹¹⁸ as happens in other areas of chemistry,^{119–123} such as light harvesting, electrocatalysis, or DNA studies, combining the advantages of homogeneous and heterogeneous modes. Probably long distances between each unit will be necessary to avoid oxidation of the ligands from neighboring units.

For the above explorations, theoretical studies should consider complete catalytic cycles besides the activation of the C-H bond of methane. For example, the second step (CH₃-OH rebound step) and the oxidation of the metal is important too. Although N₂O and O₃ are very practical for computational works and laboratory experiments, the target oxidant should be O₂ for an industrially and economically viable process.^{18,124} It should be mentioned that H₂O and H₂O₂ have also been probed as oxidants.^{125,126} In addition, the reaction of both methane

and methanol with the catalysts should be examined to address the selectivity challenge.

The above suggestions can be supported by our better knowledge of the electronic structure of transition metal oxides. The relative stability of the oxo and oxyl forms is the key parameter and traces back to fundamental quantum mechanical principles. Specifically, the parabolic (quantum prediction) and not linear (classical prediction) dependence of the ionization energy of atoms on their charge determines the oxo/oxyl composition. We believe that quantifying and controlling the oxo/oxyl ratio of the wavefunction is an important factor for moving forward, keeping in mind the significant contribution of the excited states of the catalyst to the “ground-state” chemical reactions. For example, the PCET mechanism can be seen as the HAT mechanism enabled by excited oxyl states. Orbital analysis for the different mechanisms (2+2/PCET/HAT) indicated that the π_{MO} orbitals enable proton (H^+) transfers and that π_{MO}^* eases electron (e^-) transfers. Therefore, a more detailed investigation of the electronic structure is necessary, especially for the metal oxide anionic complexes, which are largely unexplored. Photoelectron spectroscopy studies for metal monoxide anions reacting with methane and methanol, similar to those done for single metal anions¹²⁷ and polymetal-polyoxide particles,¹²⁸ will be certainly helpful. Regarding anionic species, the enhanced ionization energies urge for studies of several excited electronic states bound with respect to the neutral counterparts. Finally, the role of all types of ligands (σ/π -donors/acceptors) should be explored further.

The lessons we have learned in terms of electronic structure must be used in future theoretical and experimental explorations. Theory provides a perfect means for faster disclosure of appropriate candidate catalysts and should lead the field.¹²⁹ The “cooperation” of density functional theory and wavefunction (especially multi-reference) calculations should be promoted. For example, small molecular systems can be used for benchmarking functionals that can be used for larger species. Another important effect, which should be considered in the future, is the role of crossings between states of different spins (spin-orbit coupling), which can reveal new reaction pathways or change the reaction rates considerably.^{130,131} Machine learning methods can be helpful if the correct descriptors and methods are employed,¹³² and we believe that excited states (maybe in terms of excitation energies and not just HOMO/LUMO energies)¹³³ must be included in the models. At the same time, the bottom-up approach starting from bare oxides and gradually adding ligands of different types should not be abandoned and should proceed hand in hand with experimental observations.¹³⁴ This path offers a more chemically intuitive path and will identify the eigenvectors of the catalytic efficiency “operator” in the multi-dimensional chemical space. The coupling elements can then be considered to explore the off-diagonal regions and discover the most efficient catalysts.

Conflicts of interest

The authors declare no competing financial interests.

Acknowledgements

The authors are indebted to Auburn University for financial support and especially the James E. Land endowment. This work was completed with resources provided by the Auburn University Easley Cluster. EM wants to thank Christoforos G. Kokotos (National and Kapodistrian University of Athens, Greece) and Christian R. Goldsmith (Auburn University, USA) for the discussions.

References

- 1 The World Bank, Global Gas Flaring Reduction Partnership (GGFR), 2019, <https://www.worldbank.org/en/programs/gasflaringreduction>, (accessed 10/27/2022).
- 2 J. Jang, K. Shen and C. G. Morales-Guio, *Joule*, 2019, **3**, 2589–2593.
- 3 R. W. Howarth, *Biogeosciences*, 2019, **16**, 3033–3046.
- 4 H. D. Gesser, N. R. Hunter and C. B. Prakash, *Chem. Rev.*, 1985, **85**, 235–244.
- 5 M. Ravi, M. Ranocchiari and J. A. van Bokhoven, *Angew. Chem., Int. Ed.*, 2017, **56**, 16464–16483.
- 6 G. A. Olah, *Chem. Eng. News Archive*, 2003, **81**, 5.
- 7 G. A. Olah, *Angew. Chem., Int. Ed.*, 2005, **44**, 2636–2639.
- 8 G. A. Olah, A. Goepfert and G. K. S. Prakash, *J. Org. Chem.*, 2009, **74**, 487–498.
- 9 K. R auchle, L. Plass, H.-J. Wernicke and M. Bertau, *Energy Technol.*, 2016, **4**, 193–200.
- 10 W. M. Haynes, *CRC Handbook of Chemistry and Physics*, Taylor & Francis, 93rd edn, 2012.
- 11 S. Verhelst, J. W. G. Turner, L. Sileghem and J. Vancoillie, *Prog. Energy Combust. Sci.*, 2019, **70**, 43–88.
- 12 S. Sarp, S. Gonzalez Hernandez, C. Chen and S. W. Sheehan, *Joule*, 2021, **5**, 59–76.
- 13 W. Zhang, M. Song, Q. Yang, Z. Dai, S. Zhang, F. Xin, W. Dong, J. Ma and M. Jiang, *Biotechnol. Biofuels*, 2018, **11**, 260.
- 14 M. C. Alvarez-Galvan, N. Mota, M. Ojeda, S. Rojas, R. M. Navarro and J. L. G. Fierro, *Catal. Today*, 2011, **171**, 15–23.
- 15 J. A. Rodriguez, F. Zhang, Z. Liu and S. D. Senanayake, *Catalysis*, The Royal Society of Chemistry, 2019, vol. 31, pp. 198–215.
- 16 R. Sharma, H. Poelman, G. B. Marin and V. V. Galvita, *Catalysts*, 2020, **10**, 194.
- 17 Y. Lyu, J. N. Jocz, R. Xu, O. C. Williams and C. Sievers, *ChemCatChem*, 2021, **13**, 2832–2842.
- 18 M. H. Mahyuddin, Y. Shiota and K. Yoshizawa, *Catal. Sci. Technol.*, 2019, **9**, 1744–1768.
- 19 M. B. Park, E. D. Park and W.-S. Ahn, *Front. Chem.*, 2019, **7**, 514.
- 20 B. E. R. Snyder, M. L. Bols, R. A. Schoonheydt, B. F. Sels and E. I. Solomon, *Chem. Rev.*, 2018, **118**, 2718–2768.
- 21 P. Tomkins, M. Ranocchiari and J. A. van Bokhoven, *Acc. Chem. Res.*, 2017, **50**, 418–425.

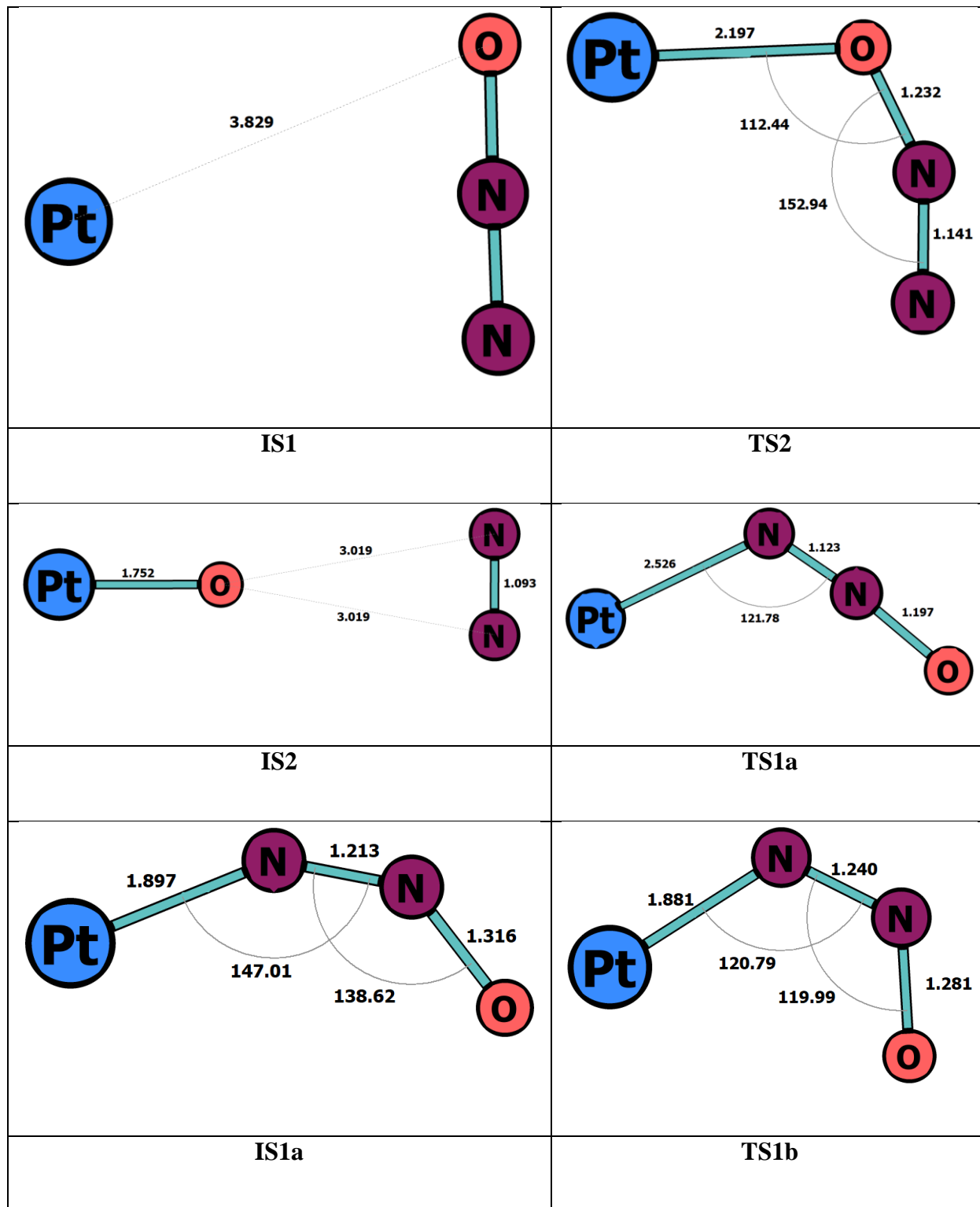
- 22 T. Ikuno, J. Zheng, A. Vjunov, M. Sanchez-Sanchez, M. A. Ortuño, D. R. Pahls, J. L. Fulton, D. M. Camaioni, Z. Li and D. Ray, *et al.*, *J. Am. Chem. Soc.*, 2017, **139**, 10294–10301.
- 23 J. Baek, B. Rungtaweeworanit, X. Pei, M. Park, S. C. Fakra, Y.-S. Liu, R. Matheu, S. A. Alshimiri, S. Alshehri and C. A. Trickett, *et al.*, *J. Am. Chem. Soc.*, 2018, **140**, 18208–18216.
- 24 D. Y. Osadchii, A. I. Olivos-Suarez, Á. Szécsényi, G. Li, M. A. Nasalevich, I. A. Dugulan, P. S. Crespo, E. J. M. Hensen, S. L. Veber and M. V. Fedin, *et al.*, *ACS Catal.*, 2018, **8**, 5542–5548.
- 25 X. Cui, H. Li, Y. Wang, Y. Hu, L. Hua, H. Li, X. Han, Q. Liu, F. Yang and L. He, *et al.*, *Chem*, 2018, **4**, 1902–1910.
- 26 G. Laudadio, Y. Deng, K. van der Wal, D. Ravelli, M. Nuño, M. Fagnoni, D. Guthrie, Y. Sun and T. Noël, *Science*, 2020, **369**, 92–96.
- 27 A. Hu, J.-J. Guo, H. Pan and Z. Zuo, *Science*, 2018, **361**, 668–672.
- 28 L. Soussan, N. Pen, M.-P. Belleville, J. S. Marcano and D. Paolucci-Jeanjean, *J. Biotechnol.*, 2016, **222**, 117–142.
- 29 C. D. Blanchette, J. M. Knipe, J. K. Stolaroff, J. R. DeOtte, J. S. Oakdale, A. Maiti, J. M. Lenhardt, S. Sirajuddin, A. C. Rosenzweig and S. E. Baker, *Nat. Commun.*, 2016, **7**, 11900.
- 30 P. V. L. Reddy, K.-H. Kim and H. Song, *Renewable Sustainable Energy Rev.*, 2013, **24**, 578–585.
- 31 Z. Zakaria and S. K. Kamarudin, *Renewable Sustainable Energy Rev.*, 2016, **65**, 250–261.
- 32 A. A. Latimer, A. Kakekhani, A. R. Kulkarni and J. K. Nørskov, *ACS Catal.*, 2018, **8**, 6894–6907.
- 33 B. G. Hashiguchi, S. M. Bischof, M. M. Konnick and R. A. Periana, *Acc. Chem. Res.*, 2012, **45**, 885–898.
- 34 P. Liao, R. B. Getman and R. Q. Snurr, *ACS Appl. Mater. Interfaces*, 2017, **9**, 33484–33492.
- 35 K. D. Vogiatzis, M. V. Polynski, J. K. Kirkland, J. Townsend, A. Hashemi, C. Liu and E. A. Pidko, *Chem. Rev.*, 2019, **119**, 2453–2523.
- 36 N. Nakatani and M. Hada, *J. Comput. Chem.*, 2019, **40**, 414–420.
- 37 A. B. Jacobs, R. Banerjee, D. E. Dewese, A. Braun, J. T. Babicz, Jr., L. B. Gee, K. D. Sutherlin, L. H. Böttger, Y. Yoda and M. Saito, *et al.*, *J. Am. Chem. Soc.*, 2021, **143**, 16007–16029.
- 38 G. M. Jones, B. A. Smith, J. K. Kirkland and K. Vogiatzis, *Inorg. Chem. Front.*, 2023, DOI: [10.1039/D2QI01961B](https://doi.org/10.1039/D2QI01961B).
- 39 J. K. Kirkland, S. N. Khan, B. Casale, E. Miliordos and K. D. Vogiatzis, *Phys. Chem. Chem. Phys.*, 2018, **20**, 28786–28795.
- 40 C. Kupper, B. Mondal, J. Serrano-Plana, I. Klawitter, F. Neese, M. Costas, S. Ye and F. Meyer, *J. Am. Chem. Soc.*, 2017, **139**, 8939–8949.
- 41 D. J. Xiao, E. D. Bloch, J. A. Mason, W. L. Queen, M. R. Hudson, N. Planas, J. Borycz, A. L. Dzubak, P. Verma and K. Lee, *et al.*, *Nat. Chem.*, 2014, **6**, 590–595.
- 42 S. Shaik, M. Filatov, D. Schröder and H. Schwarz, *Chem. – Eur. J.*, 1998, **4**, 193–199.
- 43 P. C. Andrikopoulos, C. Michel, S. Chouzier and P. Sautet, *ACS Catal.*, 2015, **5**, 2490–2499.
- 44 T. Z. H. Gani and H. J. Kulik, *ACS Catal.*, 2018, **8**, 975–986.
- 45 A. Nandy, C. Duan, C. Goffinet and H. J. Kulik, *JACS Au*, 2022, **2**, 1200–1213.
- 46 M. C. Simons, S. D. Prinslow, M. Babucci, A. S. Hoffman, J. Hong, J. G. Vitillo, S. R. Bare, B. C. Gates, C. C. Lu and L. Gagliardi, *et al.*, *J. Am. Chem. Soc.*, 2021, **143**, 12165–12174.
- 47 S. A. Ikbal, C. Colombari, D. Zhang, M. Delecluse, T. Brotin, V. Dufaud, J.-P. Dutasta, A. B. Sorokin and A. Martinez, *Inorg. Chem.*, 2019, **58**, 7220–7228.
- 48 A. Z. Msezane, Z. Felfli, K. Suggs, A. Tesfamichael and X.-Q. Wang, *Gold Bull.*, 2012, **45**, 127–135.
- 49 S. Sader and E. Miliordos, *Phys. Chem. Chem. Phys.*, 2022, **24**, 21583–21587.
- 50 H. S. Yu, X. He, S. L. Li and D. G. Truhlar, *Chem. Sci.*, 2016, **7**, 5032–5051.
- 51 M. J. Frisch, G. W. Trucks, H. B. Schlegel, G. E. Scuseria, M. A. Robb, J. R. Cheeseman, G. Scalmani, V. Barone, G. A. Petersson, H. Nakatsuji, *et al.*, *Gaussian 16 Rev. B.01*, Wallingford, CT, 2016.
- 52 H.-J. Werner, P. J. Knowles, F. R. Manby, J. A. Black, K. Doll, A. Hefselmann, D. Kats, A. Köhn, T. Korona and D. A. Kreplin, *et al.*, *J. Chem. Phys.*, 2020, **152**, 144107.
- 53 T. H. Dunning, *J. Chem. Phys.*, 1989, **90**, 1007–1023.
- 54 R. A. Kendall, T. H. Dunning and R. J. Harrison, *J. Chem. Phys.*, 1992, **96**, 6796–6806.
- 55 N. B. Balabanov and K. A. Peterson, *J. Chem. Phys.*, 2005, **123**, 064107.
- 56 K. A. Peterson, D. Figgen, M. Dolg and H. Stoll, *J. Chem. Phys.*, 2007, **126**, 124101.
- 57 D. Figgen, K. A. Peterson, M. Dolg and H. Stoll, *J. Chem. Phys.*, 2009, **130**, 164108.
- 58 E. Miliordos and A. Mavridis, *J. Phys. Chem. A*, 2007, **111**, 1953–1965.
- 59 E. Miliordos and A. Mavridis, *J. Phys. Chem. A*, 2010, **114**, 8536–8572.
- 60 C. N. Sakellaris, E. Miliordos and A. Mavridis, *J. Chem. Phys.*, 2011, **134**, 234308.
- 61 C. N. Sakellaris and A. Mavridis, *J. Phys. Chem. A*, 2012, **116**, 6935–6949.
- 62 C. N. Sakellaris and A. Mavridis, *J. Chem. Phys.*, 2013, **138**, 054308.
- 63 N. M. S. Almeida, I. R. Ariyaratna and E. Miliordos, *Phys. Chem. Chem. Phys.*, 2018, **20**, 14578–14586.
- 64 I. R. Ariyaratna and E. Miliordos, *Phys. Chem. Chem. Phys.*, 2018, **20**, 12278–12287.
- 65 N. M. S. Almeida, I. R. Ariyaratna and E. Miliordos, *J. Phys. Chem. A*, 2019, **123**, 9336–9344.
- 66 E. E. Claveau and E. Miliordos, *Phys. Chem. Chem. Phys.*, 2019, **21**, 26324–26332.
- 67 I. R. Ariyaratna and E. Miliordos, *Phys. Chem. Chem. Phys.*, 2019, **21**, 15861–15870.
- 68 I. R. Ariyaratna and E. Miliordos, *J. Quant. Spectrosc. Radiat. Transfer*, 2020, **255**, 107265.

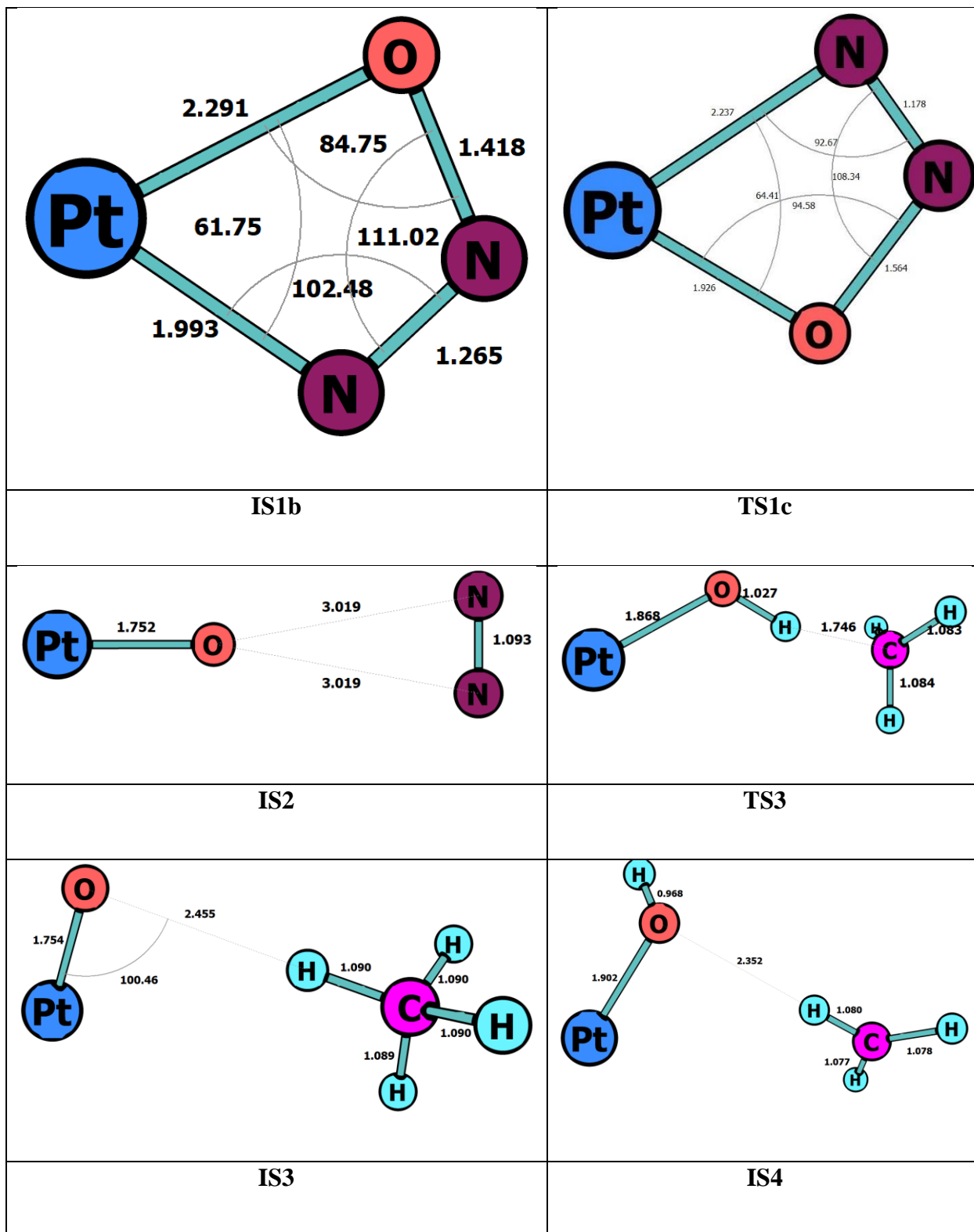
- 69 B. A. Jackson and E. Miliordos, *Phys. Chem. Chem. Phys.*, 2020, **22**, 6606–6618.
- 70 E. E. Claveau and E. Miliordos, *Phys. Chem. Chem. Phys.*, 2021, **23**, 21172–21182.
- 71 S. N. Khan and E. Miliordos, *Inorg. Chem.*, 2021, **60**, 16111–16119.
- 72 W. A. Donald, C. J. McKenzie and R. A. J. O'Hair, *Angew. Chem., Int. Ed.*, 2011, **50**, 8379–8383.
- 73 N. M. S. Almeida, F. Pawłowski, J. V. Ortiz and E. Miliordos, *Phys. Chem. Chem. Phys.*, 2019, **21**, 7090–7097.
- 74 A. J. Merer, *Annu. Rev. Phys. Chem.*, 1989, **40**, 407–438.
- 75 V. Vennelakanti, R. Mehmood and H. J. Kulik, *ACS Catal.*, 2022, **12**, 5489–5501.
- 76 A. Kramida, Y. Ralchenko, J. Reader and NIST ASD Team (2022), NIST Atomic Spectra Database (version 5.10), [Online], Available: <https://physics.nist.gov/asd> [Thu Oct 27 2022], National Institute of Standards and Technology, Gaithersburg, MD, DOI: [10.18434/T4W30F](https://doi.org/10.18434/T4W30F).
- 77 P. C. Engelking and W. C. Lineberger, *J. Chem. Phys.*, 1977, **66**, 5054–5058.
- 78 P. G. Wenthold, R. F. Gunion and W. C. Lineberger, *Chem. Phys. Lett.*, 1996, **258**, 101–106.
- 79 H. Wu and L. S. Wang, *J. Chem. Phys.*, 1997, **107**, 8221–8228.
- 80 H. Wu and L.-S. Wang, *J. Phys. Chem. A*, 1998, **102**, 9129–9135.
- 81 H. Wu and L.-S. Wang, *J. Chem. Phys.*, 1998, **108**, 5310–5318.
- 82 G. L. Gutsev, B. K. Rao, P. Jena, X. Li and L.-S. Wang, *J. Chem. Phys.*, 2000, **113**, 1473–1483.
- 83 T. M. Ramond, G. E. Davico, F. Hellberg, F. Svedberg, P. Salén, P. Söderqvist and W. C. Lineberger, *J. Mol. Spectrosc.*, 2002, **216**, 1–14.
- 84 R.-Z. Li, J. Liang, X.-L. Xu, H.-G. Xu and W.-J. Zheng, *Chem. Phys. Lett.*, 2013, **575**, 12–17.
- 85 M. K. Kristiansson, K. Chartkunchand, G. Eklund, O. M. Hole, E. K. Anderson, N. de Ruette, M. Kamińska, N. Punnakayathil, J. E. Navarro-Navarrete and S. Sigurdsson, *et al.*, *Nat. Commun.*, 2022, **13**, 5906.
- 86 W. Rasheed, A. Draksharapu, S. Banerjee, V. G. Young Jr, R. Fan, Y. Guo, M. Ozerov, J. Nehr Korn, J. Krzystek and J. Telsler, *et al.*, *Angew. Chem., Int. Ed.*, 2018, **57**, 9387–9391.
- 87 S. Hong and G. Mpourmpakis, *Catal. Sci. Technol.*, 2021, **11**, 6390–6400.
- 88 S. Zhou, J. Li, M. Schlangen and H. Schwarz, *Chem. – Eur. J.*, 2016, **22**, 7225–7228.
- 89 J. N. Harvey, M. Diefenbach, D. Schröder and H. Schwarz, *Int. J. Mass Spectrom.*, 1999, **182–183**, 85–97.
- 90 X.-L. Ding, X.-N. Wu, Y.-X. Zhao and S.-G. He, *Acc. Chem. Res.*, 2012, **45**, 382–390.
- 91 Z. Yuan, Y.-X. Zhao, X.-N. Li and S.-G. He, *Int. J. Mass Spectrom.*, 2013, **354–355**, 105–112.
- 92 Y.-X. Zhao, Q.-Y. Liu, M.-Q. Zhang and S.-G. He, *Dalton Trans.*, 2016, **45**, 11471–11495.
- 93 Z.-C. Wang, T. Weiske, R. Kretschmer, M. Schlangen, M. Kaupp and H. Schwarz, *J. Am. Chem. Soc.*, 2011, **133**, 16930–16937.
- 94 G. Fu, X. Xu, X. Lu and H. Wan, *J. Am. Chem. Soc.*, 2005, **127**, 3989–3996.
- 95 A. Božović, S. Feil, G. K. Koyanagi, A. A. Viggiano, X. Zhang, M. Schlangen, H. Schwarz and D. K. Bohme, *Chem. – Eur. J.*, 2010, **16**, 11605–11610.
- 96 K. Yoshizawa, Y. Shiota and T. Yamabe, *J. Am. Chem. Soc.*, 1998, **120**, 564–572.
- 97 R. B. Metz, in *Research Advances in Physical Chemistry*, ed. R. M. Mohan, Global, Trivandrum, India, 2001, vol. 2, pp. 35–43.
- 98 G. Altinay, M. Citir and R. B. Metz, *J. Phys. Chem. A*, 2010, **114**, 5104–5112.
- 99 G. Altinay, A. Kocak, J. Silva Daluz and R. B. Metz, *J. Chem. Phys.*, 2011, **135**, 084311.
- 100 K. Yoshizawa, Y. Shiota and T. Yamabe, *Organometallics*, 1998, **17**, 2825–2831.
- 101 K. Yoshizawa, Y. Shiota and T. Yamabe, *J. Chem. Phys.*, 1999, **111**, 538–545.
- 102 M. Zhou, *Int. Rev. Phys. Chem.*, 2008, **27**, 1–25.
- 103 G. Wang, Y. Gong, M. Chen and M. Zhou, *J. Am. Chem. Soc.*, 2006, **128**, 5974–5980.
- 104 S. Sader and E. Miliordos, *J. Phys. Chem. A*, 2021, **125**, 2364–2373.
- 105 N. B. Balabanov and K. A. Peterson, *J. Chem. Phys.*, 2006, **125**, 074110.
- 106 J. Campos, J. López-Serrano, R. Peloso and E. Carmona, *Chem. – Eur. J.*, 2016, **22**, 6432–6457.
- 107 J. T. Henthorn, S. Lin and T. Agapie, *J. Am. Chem. Soc.*, 2015, **137**, 1458–1464.
- 108 A. Delabie, C. Vincier, M. Flock and K. Pierloot, *J. Phys. Chem. A*, 2001, **105**, 5479–5485.
- 109 W. B. Tolman, *Angew. Chem., Int. Ed.*, 2010, **49**, 1018–1024.
- 110 M. H. Mahyuddin, Y. Shiota, A. Staykov and K. Yoshizawa, *Inorg. Chem.*, 2017, **56**, 10370–10380.
- 111 B. C. Sweeny, B. A. Long, A. A. Viggiano, S. G. Ard and N. S. Shuman, *J. Phys. Chem. A*, 2022, **126**, 859–869.
- 112 I. R. Ariyaratna, N. M. S. Almeida and E. Miliordos, *Phys. Chem. Chem. Phys.*, 2020, **22**, 16072–16079.
- 113 S. Das, C. D. Incarvito, R. H. Crabtree and G. W. Brudvig, *Science*, 2006, **312**, 1941–1943.
- 114 S. A. Cook and A. S. Borovik, *Acc. Chem. Res.*, 2015, **48**, 2407–2414.
- 115 G. Olivo, G. Farinelli, A. Barbieri, O. Lanzalunga, S. Di Stefano and M. Costas, *Angew. Chem., Int. Ed.*, 2017, **56**, 16347–16351.
- 116 K. Rajabimoghadam, Y. Darwish, U. Bashir, D. Pitman, S. Eichelberger, M. A. Siegler, M. Swart and I. Garcia-Bosch, *J. Am. Chem. Soc.*, 2018, **140**, 16625–16634.
- 117 J. R. Frost, S. M. Huber, S. Breitenlechner, C. Bannwarth and T. Bach, *Angew. Chem., Int. Ed.*, 2015, **54**, 691–695.
- 118 S. Zhao, L. Ma, Y. Xi, H. Shang and X. Lin, *RSC Adv.*, 2021, **11**, 11295–11303.
- 119 P. Braunstein, H.-P. Kormann, W. Meyer-Zaika, R. Pugin and G. Schmid, *Chem. – Eur. J.*, 2000, **6**, 4637–4646.
- 120 B. Fabre, *Chem. Rev.*, 2016, **116**, 4808–4849.

- 121 L. Gao, S.-X. Du and H.-J. Gao, *Int. J. Mol. Sci.*, 2010, **11**, 656–671.
- 122 L. A. Hunt, R. R. Rodrigues, K. Foell, D. Nugegoda, H. Cheema, N. I. Hammer and J. H. Delcamp, *J. Phys. Chem. C*, 2021, **125**, 25410–25421.
- 123 E. Pyrak, A. Jaworska and A. Kudelski, *Molecules*, 2019, **24**, 3921.
- 124 C. Hammond, S. Conrad and I. Hermans, *ChemSusChem*, 2012, **5**, 1668–1686.
- 125 V. L. Sushkevich, D. Palagin, M. Ranocchiari and J. A. van Bokhoven, *Science*, 2017, **356**, 523–527.
- 126 Á. Szécsényi, G. Li, J. Gascon and E. A. Pidko, *ACS Catal.*, 2018, **8**, 7961–7972.
- 127 G. Liu, Z. Zhu, S. M. Ciborowski, I. R. Ariyaratna, E. Miliordos and K. H. Bowen, *Angew. Chem., Int. Ed.*, 2019, **58**, 7773–7777.
- 128 R. B. Wyrwas, B. L. Yoder, J. T. Maze and C. C. Jarrold, *J. Phys. Chem. A*, 2006, **110**, 2157–2164.
- 129 S. Ahn, M. Hong, M. Sundararajan, D. H. Ess and M.-H. Baik, *Chem. Rev.*, 2019, **119**, 6509–6560.
- 130 E. R. Heller and J. O. Richardson, *J. Am. Chem. Soc.*, 2021, **143**, 20952–20961.
- 131 A. O. Lykhin, D. S. Kaliakin, G. E. dePolo, A. A. Kuzubov and S. A. Varganov, *Int. J. Quantum Chem.*, 2016, **116**, 750–761.
- 132 A. Nandy, H. Adamji, D. W. Kastner, V. Vennelakanti, A. Nazemi, M. Liu and H. J. Kulik, *ACS Catal.*, 2022, **12**, 9281–9306.
- 133 D. J. Durand and N. Fey, *Chem. Rev.*, 2019, **119**, 6561–6594.
- 134 R. Hoffmann, presented in part at the 12th triennial congress of the World association of theoretical and computational chemists, Vancouver Convention Center, Vancouver, BC, Canada, July 8, 2022, 2022.

APPENDIX 2

Supporting Material for Chapter 3





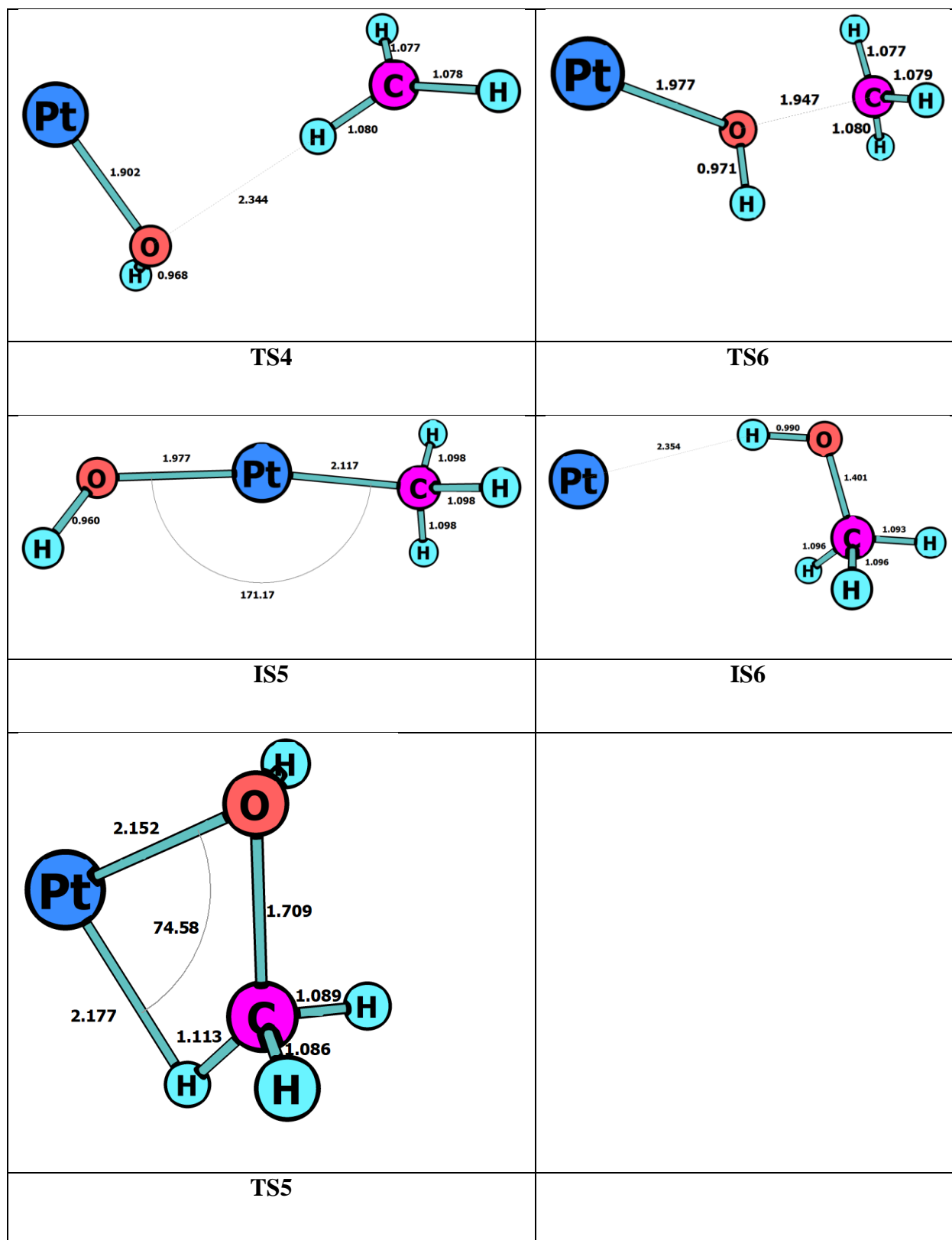


Figure S1. Optimized geometries of intermediates and transition states in $\text{Pt}^- + \text{N}_2\text{O} + \text{CH}_4$ reaction calculated at MN15/stable=opt/MN15/aug-cc-pVTZ level of theory. Bond lengths and angles are in angstroms and degrees, respectively.